Technische Universität München
TUM School of Natural Sciences

Erbium dopants in nanophotonic silicon waveguides and cavities

Andreas Maximilian Gritsch

Vollständiger Abdruck der von der TUM School of Natural Sciences der Technischen Universität München zur Erlangung eines

Doktors der Naturwissenschaften (Dr. rer. nat.)

genehmigten Dissertation.

Vorsitz: Prof. Dr. Michael Knap

Prüfer der Dissertation:

1. Prof. Dr. Andreas Reiserer
2. Prof. Dr. Rudolf Gross

Die Dissertation wurde am 17.01.2024 bei der Technischen Universität München eingereicht und durch die TUM School of Natural Sciences am 29.02.2024 angenommen.

MAX PLANCK INSTITUTE
OF QUANTUM OPTICS

Erbium dopants in nanophotonic silicon waveguides and cavities

Andreas Gritsch

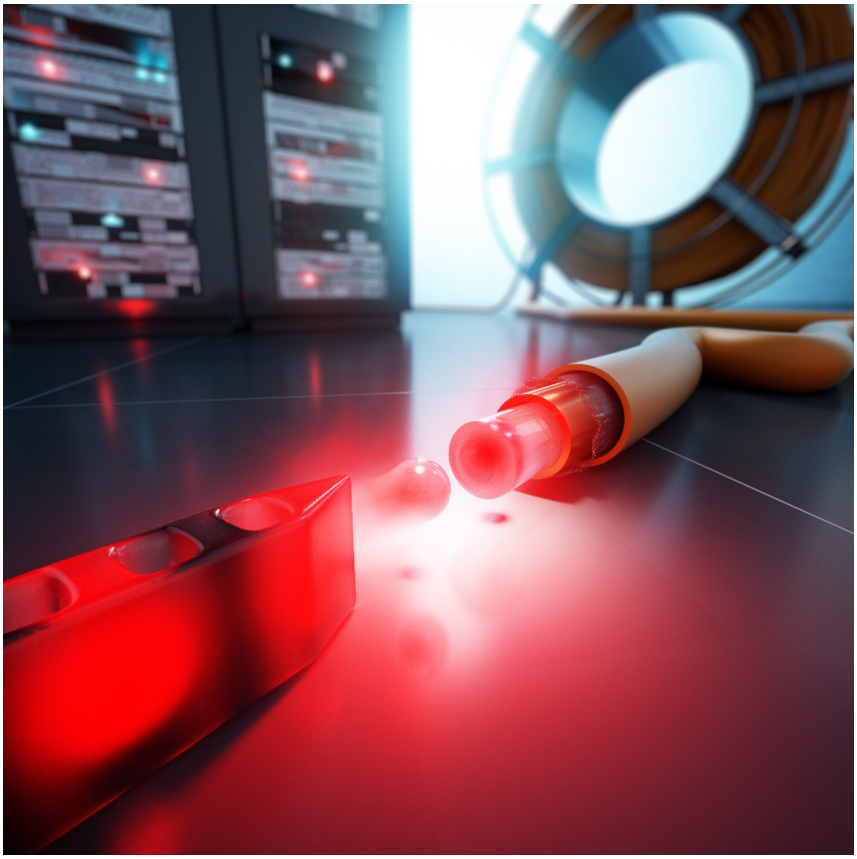

Dissertation

Max-Planck-Institute of Quantum Optics and
TUM School of Natural Sciences, Technical University of Munich

Cover: Artist's view of a future single-photon source based on a single erbium dopant embedded in a silicon photonic crystal resonator. ©Christoph Hohmann, MCQST.

Acknowledgments

First of all, I would like to express my deepest appreciation to Andreas Reiserer. Your passion for science, your deep understanding of physics, the countless discussions, and the ambition and effort you put into your work and this project in particular have always been motivating and inspiring. Beyond the scientific parts, I would like to thank you for the excellent and trusting communication and for the freedoms I have enjoyed during the past years.

For the work on nanophotonic waveguides, I teamed up with Lorenz Weiss. Thank you for the excellent collaboration and the work you put into this project including countless sample exchanges on both weekdays and weekends. Thank you also for taking care of all the bureaucracy such that I could focus only on the cleanroom and the lab work. This project was later joined by Stephan Rinner, in particular for the measurements on the AMF samples. Thank you for your effort, the excellent collaboration and for succeeding Lorenz as the chief of sample exchanges.

Furthermore, I am very grateful to Alexander Ulanowski. Your insight into singles in resonators, your programming skills, and your motivation and dedication including many long night shifts have been an integral part leading to the success of the silicon cavity project. Thank you for your outstanding effort and collaboration.

Johannes Früh, I am still feeling sorry for leaving our office. Nevertheless, I would like to thank you for the excellent collaboration on the coherence times of single emitters and for always providing helping hands, in the lab, in the clean room, and in the electronics workshop. And also for bringing the best cake I ever had at MPQ.

Moreover, special thanks to Jakob Pforr, who started as a master student on the silicon cavity towards the end of this project and almost immediately took over my entire clean room work, and now joined the group as a PhD student. Thank you specifically for fabricating the latest generation of samples.

During the last year, I shared the office with Kilian Sandholzer. I would like to thank you for the long and detailed discussions about different fields of physics and the critical questions about my work which regularly resulted in new ideas.

In general, I am grateful to every former and current member of the quantum networks group, for the outstanding collaboration in the lab and the cleanroom, the passionate scientific discussions during lunch breaks, coffee breaks, and in between, and the overall positive and friendly atmosphere. I wish everyone the best for their current and future projects.

Specifically, I want to mention Benjamin Merkel, Pablo Cova Fariña, Tangui Aladjidi, Zarije Ademi, Florian Burger, Jonas Schmitt, Fabian Salamon, Kilian Sandholzer, Nilesh Goel, Adrian Holzäpfel, Mayssane Selmani, and Daniele Lopriore.

Futhermore, I would like to thank the technicians and the entire administration at

MPQ for their efficient support. Moreover, I want to thank the ZNN, the WSI, and the WMI for providing us access to their clean room facilities. Without the latter, this project would not have been feasible.

I am indebted to my family and friends for their love and support. Especially, I would like to thank my parents for their everlasting support before and during my PhD. Furthermore, I would also like to thank my brother Matthias for his understanding when this PhD project again interfered in an unfortunate way with the opening hours of the grocery stores in Bavaria and for his help with the 3D visualization figure of our sample.

Finally, I would like to thank Andreas Reiserer, Alexander Ulanowski, Kilian Sandholzer, Adrian Holzäpfel, Stephan Rinner, Jakob Pforr, and my mother for the careful proof-reading of this thesis or at least parts of it.

Abstract

In this thesis, erbium dopants in nanophotonic silicon structures are investigated as practical building blocks for quantum network nodes. Resonant spectroscopy in nanophotonic waveguides demonstrates that erbium dopants are reproducibly integrated in silicon at a small number of previously unknown, well-defined lattice sites. Two of these novel sites stand out for their favorable properties for quantum technologies with optical transitions at 1537.76 nm and 1536.06 nm. They further exhibit narrow inhomogeneous broadenings $< 0.5\,\mathrm{GHz}$, short radiative lifetimes $< 200\,\mu\mathrm{s}$, and narrow homogeneous linewidths $< 0.01\,\mathrm{MHz}$ implying promising optical coherence properties. The latter are preserved up to temperatures of 8 K due to the large crystal field splittings $> 1.7\,\mathrm{THz}$. Furthermore, these two sites are also observed in low-loss waveguides fabricated as part of a commercial multi-project wafer run. This demonstrates the compatibility of erbium dopants in silicon with industrial nanofabrication processes for mass production.

To enhance the optical coupling to individual dopants, one-dimensional photonic crystal cavities are designed and fabricated. These devices achieve a Q-factor of $\approx 1 \times 10^5$ and a mode volume of $< 1\,(\lambda/n)^3$. In these resonators, a small number of single erbium dopants are spectrally resolved and individually addressed. Single dopants show spectral diffusion linewidths of $< 15\,\mathrm{MHz}$, Purcell enhancements of up to 177, and their emitted photons exhibit high single-photon purity $g^{(2)}(0) < 0.02$. Furthermore, optical Rabi oscillations are observed, and photon echo measurements show an optical coherence time of $T_2 = 1.31(5)\,\mu\mathrm{s}$. By applying a magnetic field, the electronic spin states of a single dopant are resolved and optically polarized. This forms an optically addressable spin qubit. The eigenstates states of this qubit are detected with a fidelity of 87.2(5) %. This result represents the first demonstration of an optical single-shot readout of a single spin qubit in silicon. In addition, the spin states can be coherently driven by directly applying microwave pulses, and spin echo sequences show a spin coherence time of $t_2 = 48(2)\,\mu\mathrm{s}$.

The results presented in this work establish erbium dopants in silicon as a promising candidate for chip-based and scalable quantum network nodes.

Publications

- S. Rinner*, F. Burger*, A. Gritsch*, J. Schmitt, and A. Reiserer. 2023. "Erbium Emitters in Commercially Fabricated Nanophotonic Silicon Waveguides." Nanophotonics 12, 3455–3462 (2023). https://doi.org/10.1515/nanoph-2023-0287.
- A. Gritsch, A. Ulanowski, and A. Reiserer. 2023. "Purcell Enhancement of Single-Photon Emitters in Silicon." Optica 10 (6): 783–89. https://doi.org/10.1364/OPTICA.486167.
- A. Gritsch*, L. Weiss*, J. Früh, S. Rinner, and A. Reiserer. 2022. "Narrow Optical Transitions in Erbium-Implanted Silicon Waveguides." Physical Review X 12 (4): 041009. https://doi.org/10.1103/PhysRevX.12.041009.
- L. Weiss*, A. Gritsch*, B. Merkel, and A. Reiserer. 2021. "Erbium Dopants in Nanophotonic Silicon Waveguides." Optica 8 (1): 40–41. https://doi.org/10.1364/OPTICA.413330.

Contents

1. Erbium dopants in silicon: A scalable material platform for quantum networks

The 2022 Nobel Prize in Physics was awarded for the entanglement of photons, the violation of Bell's inequality, and for experiments that pioneered the field of quantum information science. With their work, the laureates, Aspect, Clauser, and Zeilinger, have not only tested fundamental predictions of quantum science but they also brought its technological applications closer (Nobel Prize Outreach AB 2022). The enormous interest in these technologies stems from the predicted superiority of the quantum systems over their classical counterparts in certain applications. So far, such quantum advantages have been envisioned in four main areas (Acín et al. 2018; Reiserer 2022). These areas are quantum computation (Preskill 2018), quantum simulation (Bloch, Dalibard, and Nascimbène 2012; Georgescu, Ashhab, and Nori 2014; Daley et al. 2022), quantum sensing (Degen, Reinhard, and Cappellaro 2017), and quantum communication (Wehner, Elkouss, and Hanson 2018; Gisin and Thew 2007; Lu et al. 2022).

The fundamental building blocks of these technologies, i.e., the elementary carriers of quantum information, are called quantum bits, or qubits for short. Ideally, these qubits are quantum systems whose states can be initialized, coherently controlled, and read out with high fidelity, but which are otherwise completely isolated from their environment. This is difficult to implement experimentally. As a result, breakthroughs in quantum technologies are often associated with novel qubit encodings. For example, the key to the award-winning experiments of the three Nobel laureates was the encoding of qubits in the states of optical photons (Nobel Prize Outreach AB 2022).

To date, the ability to address and manipulate individual qubits has also been achieved on several other experimental platforms, such as ions (**bruzewiczTrappedionQuantumComputing2019** or neutral atoms trapped in vacuum, superconducting circuits, and many different solid-state systems (de Leon et al. 2021; Becher et al. 2023). All of these qubit realizations have individual strengths and challenges, and first indications of a quantum advantage for special types of problems have been demonstrated with today's experimental hardware (Arute et al. 2019; Zhong et al. 2020; Wu et al. 2021). Nevertheless, the challenge of building quantum hardware that allows the realization of large-scale and deployable systems remains open (de Leon et al. 2021). A key limitation for most systems is the scalability of the number of qubits and the number of quantum information processing units. To overcome this, hybrid systems which combine the favorable properties of different qubit implementations and novel material platforms which are compatible with existing technologies are explored.

In this work, erbium dopants in silicon are investigated as a novel material platform for quantum technologies. The motivation to investigate this material platform stems

from its compatibility with established silicon nanofabrication technology and with fiber-optical networks. The material platform is thus particularly attractive for elementary quantum network nodes and promises unprecedented scaling potential once sufficient control of individual qubits can be achieved.

1.1. Quantum Networks

A central goal associated with quantum communication is the realization of quantum networks (Kimble 2008). Future quantum networks will provide entanglement, the central resource for quantum information processing, between stationary network nodes. The shared entanglement will enable, e.g., communication with verifiable security, distributed quantum sensing, and blind and distributed quantum computing (Wehner, Elkouss, and Hanson 2018) between the remote nodes. To create shared entanglement between the remote nodes, they will be connected with quantum links. These quantum links will be photonic links that allow the distribution of quantum states encoded in photons at the fastest possible speed, the speed of light, similar to the information exchange in classical networks based on classical electromagnetic fields (Reiserer 2022).

In the simplest case, the photonic link operates by sending a single qubit encoded in a single photon. To realize network nodes, these flying qubits have to be interfaced with stationary qubits, which allow storing and manipulating the quantum states locally. Stationary qubits for quantum network nodes should fulfill two requirements. First, their coherence must exceed the time of flight of the photon from one node to another and the signaling time for classical information exchange between the two nodes after photon arrival. Second, the stationary qubits require an efficient coupling to the flying qubit (DiVincenzo 2000). These requirements can be fulfilled by spin qubits encoded in long-lived electronic spin, nuclear spin, or superhyperfine states of atom-like emitters. Many quantum network protocols are further enhanced or enabled by embedding the emitters into an optical resonator (Reiserer 2022).

Examples of atom-like emitters that couple to spin states with sufficient coherence times are neutral atoms or ions trapped in vacuum and optically addressable spin qubits in solid-state host materials. Neutral atoms trapped in vacuum have been established as one of the leading platforms for quantum network nodes and offer several advantages. First, all atoms are completely identical, i.e., the individual qubits do not require further characterization, and the frequencies of two emitters are always identical. Second, they are very well isolated from their environment in ultra-high vacuum, resulting in sufficiently long coherence times (Reiserer and Rempe 2015).

In contrast, many optically addressable solid-state qubits studied to date are more susceptible to decoherence induced by their environment, in particular their host crystal. However, an advantage of this material platform is that the technological effort to operate a network node can be lower, in particular, because neither laser trapping and laser cooling nor ultra-high vacuum chambers are required. This may reduce both the cost and the difficulty of operating a quantum network node based on solid-state spin qubits (de Leon et al. 2021). In addition, solid-state systems could potentially be integrated on

a single chip, which could significantly increase the qubit density. This miniaturization and scaling potential is particularly large if the host material is compatible with established semiconductor nanofabrication methods (Wolfowicz et al. 2021). Examples for optically addressable solid-state spin qubits with sufficient coherence times for quantum networking are color centers in large band-gap semiconductors and rare-earth dopants (Reiserer 2022). This thesis focuses on erbium dopants, which are part of the group of rare-earth elements.

1.2. Rare-earth dopants in solids

The rare-earth elements, i.e., the lathanides, yttrium and scandium, are a group of elements which have similar chemical properties. In solids, rare-earth dopants are typically found in their triply ionized state. In materials with a sufficient band gap and dilute dopant concentration, they form atom-like quantum systems surrounded by an effective semiconductor vacuum which exhibit optical transitions between the *4f* orbitals. These transitions are electric-dipole-forbidden in free space but become partially allowed when embedded in a host crystal (Liu and Jacquier 2005). Still, the oscillator strength of these transitions remains weak even in host crystals. Compared with color centers, rare-earth dopants thus have usually orders of magnitude longer optical lifetimes.

Furthermore, the *4f* orbitals are closer confined to the atomic nuclei than the completely filled *5s* and *5p* orbitals (shown in Fig. 1.1 a for erbium) (Liu and Jacquier 2005). Therefore, the electrons in the *5s* and *5p* orbitals partially compensate for the electric field induced by neighboring atoms of the host crystal. This characteristic shielding of the inner *4f* electrons leads to the long spin lifetimes and excellent spin coherence times observed for many rare-earth dopants. Furthermore, due to this characteristic shielding, the host crystal of rare-earth dopants acts more like a perturbation on the Hamiltonian of the ion in free space, rather than defining it. In particular, the host crystal lifts the degeneracy of the spin-orbit energy levels of the optical ground and excited states. However, the level splittings induced by the crystal field remain typically orders of magnitude smaller than the optical transition energy. For instance, erbium dopants typically exhibit a crystal field splitting of about 1 THz to 10 THz, but the optical transition is found at $\approx$ 195 THz independent of the host crystal (Fig. 1.1 b, c). Importantly, this implies that for rare-earth dopants, the choice of the host material can be seen as an engineering degree of freedom.

Rare-earth dopants are further classified into Kramers ions with an odd number of electrons in the 4f shell and non-Kramers ions with an even number, each in the triply ionized state. Non-Kramers ions (e.g., Pr, Eu, Tm) at sites with sufficiently low symmetries have quenched electronic moments (Macfarlane 2002) which are less sensitive to magnetic noise and thus provide excellent coherence properties. A record coherence time of 6 h is found for nuclear spin states of Eu ions in an yttrium orthosilicate (YSO) host (Zhong et al. 2015) despite the high density of nuclear spins in the crystal used.

In contrast, Kramers ions (e.g., Er, Nd, Yb) cannot have quenched electronic moments and typically tend to interact more strongly with the surrounding magnetic environment.

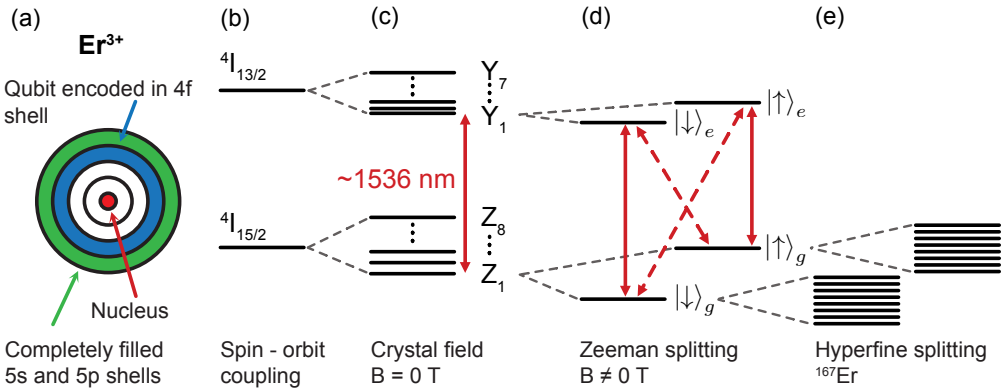

Figure 1.1.: **Er^{3+} in a dielectric host crystal**. (a) Schematic spatial distribution of the radial wavefunctions of an Er^{3+} ion. The valence electron in the 4f shell (blue) is located closer to the nucleus (red) than the electrons in 5s and 5p shells (green) leading to an effective shielding from the environment. This has direct consequences on the energy levels of the Er^{3+} ion (b-e). In particular, any dielectric host material acts only as a perturbation (c) on the free space Hamiltonian of Er^{3+} (b) lifting the degenerate spin-orbit energy levels. This is called the crystal field splitting. (d) By applying a magnetic field, the electron spin degeneracy is further lifted, and a qubit can be encoded in the optical ground state. (e) All but one erbium isotope do not have a nuclear spin. Only ^{167}Er has a nuclear spin of 7/2, which gives rise to a hyperfine splitting.

In general, this is detrimental to the spin lifetimes and coherence times (Car et al. 2019). In particular, it is challenging to achieve long coherence times in presence of strong and anisotropic interactions even with dynamical decoupling sequences (Merkel, Cova Fariña, and Reiserer 2021). To overcome this, quantum states can be encoded in hyperfine (Kindem et al. 2020) or nuclear (Ruskuc et al. 2022) spin states. A particular interesting approach is to freeze out the electronic spin of Kramers ions by applying sufficiently large magnetic fields at sufficiently low temperatures. Under these conditions, coherence times exceeding seconds are found (Rančić et al. 2018). As an alternative, Kramers ions at low dopant concentrations (Böttger et al. 2006; Cova Fariña et al. 2021) in crystals with few and weak nuclear spin moments (Dantec et al. 2021; Ourari et al. 2023) are promising. In this case, an advantage of the Kramers ions is that the single unpaired electron behaves as an effective spin-1/2 system (Maryasov and Bowman 2012), i.e., an ideal qubit (Thiel, Böttger, and Cone 2011; Reiserer 2022), once a magnetic field is applied to lift the degeneracy of the spin state (Fig. 1.1 d).

1.3. Erbium

Initial experiments with elementary quantum network nodes have been carried out in laboratory environments, where the propagation loss of the photonic links is typically not limiting. Once such networks are scaled up to global distances, this propagation loss becomes a major concern. Depending on the wavelength of the transmitted light, the absorption coefficient varies by several orders of magnitude (Fig. 1.2 a), which has drastic consequences for the transmission probability of a single photon through 50 km of optical glass fiber (Fig. 1.2 b). The wavelength range around the absorption minimum from 1500 nm to 1600 nm is therefore also called the telecommunication window and is used for most modern fiber-based communication technologies. However, most of the emitters studied to date couple to photons in the visible range, including defects in diamond and silicon carbide (red in Fig. 1.2), neutral atoms and ions trapped in free space (green), and various rare-earth dopants (blue). Importantly, only transitions originating from long-lived optical ground states which provide sufficiently long memory times are included here. To this end, single quantum dots are not shown, despite their wide tunability, because of the unsolved challenge of coupling them to suitable memory qubits (Lodahl, Mahmoodian, and Stobbe 2015).

Fig. 1.2 b shows that visible photons are transmitted over 50 km with a probability of $< 1 \times 10^{-10}$ which prevents communication at a reasonable rate. To overcome this, quantum frequency conversion (QFC) can be applied to the photonic qubits. To this end, a photon of any wavelength is converted locally at the network node to another photon typically within the telecom window while preserving all the encoded quantum information (Krutyanskiy et al. 2023; Zhou et al. 2023). State-of-the-art QFC devices have already achieved device efficiencies of around $\approx 60\,\%$ (van Leent et al. 2022), but the additional technological overhead seems detrimental for scaling up quantum networks. To avoid this, other emitters, i.e., color centers in silicon and silicon carbide, and erbium dopants, are investigated, which exhibit optical transitions closer to the absorption minimum.

Erbium features an optical transition at ≈ 1536 nm and is the only emitter precisely in the minimum. After 50 km of optical fiber, the probability that an emitted photon is transmitted is still about $10\,\%$ (Reiserer 2022). Remarkably, the coherence of this optical transition approaches the lifetime limit in optical cavities (Merkel, Ulanowski, and Reiserer 2020).

Due to the limited influence of the host crystal on the optical transition frequency, the compatibility with optical fiber networks is preserved in most transparent host crystals (Sec. 1.2). Thus, the choice of the host material is a degree of freedom that can be used to optimize the properties of the spin-photon interface. To fully exploit the technological potential of erbium dopants, the material system formed by the dopants and the host should fulfill four properties: (1) The erbium dopants should integrate at a well-defined lattice site leading to a high integration yield. (2) The smallest energy splitting between the lowest, long-lived state in each crystal field manifold and the nearest crystal field level should be as large as possible since this determines the temperature at which the spin qubit can still be operated coherently. In particular, this excludes the integration

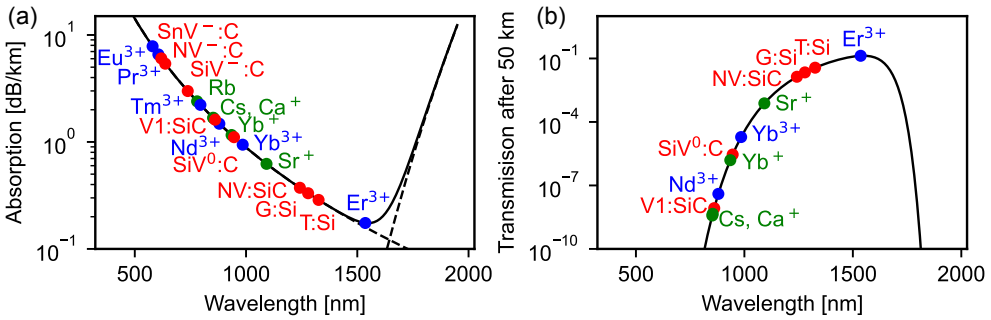

Figure 1.2.: **Absorption and transmission after** 50 km **in optical glass fiber.** The black solid lines indicate (a) the absorption coefficient and (b) the transmittance after 50 km, respectively. Dots (red: color centers, green: trapped atoms and ions, blue: rare-earth ions) indicate the optical transition wavelengths of different material systems studied in the context of quantum technologies. The dashed lines in (a) indicate the contributing processes, i.e., Rayleigh scattering for short wavelengths and infrared multi-photon absorption for longer wavelengths (Reiserer 2022). In most commercially available fibers, OH-groups generated during fiber fabrication cause several peaks of the absorption coefficient between 1200 nm and 1550 nm (not shown) (Thomas et al. 2000). The Er^{3+} ion stands out as the only emitter with an optical transition at the maximum transmittance. Figure adapted from (Reiserer 2022).

of erbium dopants at lattice sites with too high symmetries, e.g., cubic sites, where the degeneracy of the spin-orbit energy levels in free space may not be entirely lifted by the host (Stevenson et al. 2022). (3) The host crystal should provide a magnetic vacuum, i.e., it should consist of atoms without nuclear spin moments. This excludes all host matrices consisting (partially) of elements with odd principal quantum numbers. (4) The host material should be compatible with nanofabrication to allow up-scaling by on-chip integration.

So far, erbium has been extensively studied in yttrium-based crystals, e.g. YSO, in which erbium dopants substitute yttrium very well thus satisfying condition (1). Furthermore, YSO also satisfies condition (2) since the smallest crystal field splitting (≈ 1.1 THz) is sufficiently large to operate spin qubits at temperatures of about 1.7 K accessible with ^{4}He cryocoolers. Unfortunately, all yttrium isotopes carry a small magnetic moment, and yttrium crystals appear to be notoriously incompatible with nanofabrication. Hence, YSO does not satisfy conditions (3) and (4). To overcome this, erbium dopants have recently been integrated in other host crystals, such as calcium tungstate ($CaWO_4$) (Ourari et al. 2023; Dantec et al. 2021), titanium dioxide (TiO_2) (Phenicie et al. 2019), and magnesium oxide (MgO) (Stevenson et al. 2022). In all of these hosts, magnetic vacuum (i.e., condition (3)) can be achieved by isotopic purification, but nanofabrication is

difficult and typically requires hybrid integration. Another alternative is the integration of erbium dopants in silicon, which is the focus of this work. Conditions (3) and (4) are fulfilled very well by silicon. Conditions (1) and (2), i.e., the dopant integration and the crystal field splitting, are studied in this thesis.

1.4. Silicon

The semiconductor industry has driven the nanofabrication capabilities of the silicon electronics platform to a unique level of maturity. In addition, silicon is one of the most studied materials for nanophotonic applications. The band gap in silicon is only 1.12 eV corresponding to a free space wavelength of ≈ 1100 nm (Gross and Marx 2018). Silicon photonics is therefore not compatible with visible wavelengths. Moreover, for wavelengths in the proximity of the band gap, i.e., in the near-infrared regime, silicon photonic devices are limited to low optical powers, below the onset of two-photon absorption processes. Once this condition is met, the absorption in silicon can be very low because samples with residual impurities on the level of 50 ppm or lower are available. In addition, silicon has a large refractive index ≈ 3.45 at 1550 nm. In combination with the established nanofabrication techniques, this allows the realization of optical resonators with ultra-high quality factors (1×10^7) (Asano et al. 2017) and ultra-low mode volumes ($1 \times 10^{-3}\,(\lambda/n)^3$) (Hu et al. 2018). Furthermore, arrays of cavities with near-unity vertical coupling efficiency can be fabricated in a 300 mm full-wafer processing run using UV-lithography demonstrating the scaling potential of the platform (Panuski et al. 2022).

In addition to its favorable optical properties, silicon can also be an excellent host for spin qubits. For this purpose, silicon is isotopically purified to avoid decoherence due to the nuclear spin of the ^{29}Si isotope, which has a natural abundance of $\approx 5\,\%$. Importantly for photonic applications, silicon-on-insulator wafer with a pure ^{28}Si device layer grown by molecular-beam-epitaxy have also been realized (Liu et al. 2022). Single spins embedded in an isotopically purified ^{28}Si environment exhibit coherence times up to 3 h at cryogenic temperatures (Saeedi et al. 2013). Even at room temperature, a spin coherence time of 39 min is measured in a configuration where spin initialization and readout are performed at cryogenic temperatures (Saeedi et al. 2013). Quantum dots and single spins in purified silicon have thus demonstrated one- and two-qubit gate fidelities close to the requirements for fault-tolerant quantum computing (Xue et al. 2022; Noiri et al. 2022; Philips et al. 2022; Mądzik et al. 2022).

However, to date, spins in silicon have not been controlled optically as required for quantum networks. Optically active quantum dots in silicon and thus spin-photon interfaces based on quantum dots are hindered by the indirect band gap of silicon (Lodahl, Mahmoodian, and Stobbe 2015). Instead, color centers in silicon like the T center (Higginbottom et al. 2022; Simmons 2023) or the G center (Saggio et al. 2023; Redjem et al. 2020; Hollenbach et al. 2022; Komza et al. 2022) and erbium dopants (this work) seem to be promising candidates to exploit the outstanding scaling potential and the excellent magnetic vacuum provided by silicon.

Thesis outline

This thesis consists of two main parts. First, I investigate the properties of erbium dopants in a silicon host crystal (Chap. 2). For this purpose, ensembles of erbium dopants are integrated into nanophotonic waveguides and studied spectroscopically (Weiss et al. 2021). In pure silicon and with optimized sample preparation methods, erbium dopants integrate at two sites with favorable optical properties (Gritsch et al. 2022). These two sites are investigated in detail. Furthermore, I show that erbium dopants can also be studied in commercially fabricated samples (Rinner et al. 2023).

I then turn to the second part of this thesis which focuses on resolving and controlling single dopants in silicon. To facilitate such measurements, individual emitters are coupled to a cavity mode (Chap. 3). To this end, a suitable photonic crystal cavity is designed and fabricated (Chap. 4). Next, Purcell enhancement of single erbium dopants in silicon is demonstrated in this cavity (Chap. 5) (Gritsch, Ulanowski, and Reiserer 2023). In addition, the electronic spin states of a single erbium dopant are resolved by applying a magnetic field. These electronic spin states form a solid-state spin qubit. To characterize this qubit, optical initialization, optical single shot readout, and direct driving of the spin states using microwave pulses are investigated.

Finally, I give a short conclusion of the results achieved with ensembles of erbium dopants in silicon and single erbium dopants in nanophotonic silicon cavities (Chap. 6).

2. Ensembles of erbium dopants in silicon

In this chapter, the properties of ensembles of erbium dopants in silicon are investigated. The work presented in this chapter has so far resulted in three publications (Weiss et al. 2021; Gritsch et al. 2022; Rinner et al. 2023). First, the experimental approach to study ensembles of erbium dopants by integrating them into nanophotonic silicon waveguides is presented (Sec. 2.1). Then, the effect of impurities and implantation-induced defects on the integration of erbium dopants is discussed, motivating novel implantation and annealing conditions (Sec. 2.2). Next, a detailed overview of the samples (Sec. 2.3) and the nanophotonic waveguides (Sec. 2.4) studied in this work is given. Resonant spectroscopy on these waveguides reveals that erbium dopants are reproducibly integrated at a few novel, well-defined lattice sites in the silicon host matrix (Sec. 2.5). Two of these sites stand out for their favorable properties. In particular, the erbium dopants at these sites exhibit large crystal field splittings $> 1.7\,\mathrm{THz}$ (Sec. 2.6), narrow inhomogeneous linewidths of about $0.5\,\mathrm{GHz}$ (Sec. 2.7), short optical lifetimes $< 200\,\mu\mathrm{s}$ (Sec. 2.8), and narrow homogeneous linewidths smaller than $10\,\mathrm{kHz}$ (Sec. 2.9). The latter implies exceptional optical coherence, which remains intact up to temperatures of about $8\,\mathrm{K}$ due to the large crystal field splittings. Furthermore, the electronic spin states of the erbium dopants are resolved by applying a magnetic field (Sec. 2.10). Finally, these results are summarized and an outlook on future experiments with ensembles of erbium dopants in silicon is provided (Sec. 2.11).

2.1. Resonant fluorescence spectroscopy in nanophotonic waveguides

The integration of erbium dopants in silicon requires a non-equilibrium technique due to the low solubility of erbium in silicon (Kenyon 2005). The low solubility is explained by the ionic size mismatch of the erbium dopants and the silicon atoms (Rahm, Hoffmann, and Ashcroft 2016) and by the mismatch in the chemical nature of their bonds. Silicon exhibits covalent bonding while erbium dopants form triply positively charged ions in solids (Sec. 1.2).

The most commonly used non-equilibrium integration technique is ion implantation (Kenyon 2005), which is also used in this work. The implantation depth from the crystal surface is proportional to the energy used to accelerate the ions and is typically limited to the order of $\sim 1\,\mu\mathrm{m}$.

Alternatively, erbium dopants can be integrated during the growth of the silicon crystal, for example, by molecular beam epitaxy (MBE) or chemical vapor deposition (CVD) (Polman 1997; Vinh, Ha, and Gregorkiewicz 2009). The thickness of the erbium-doped

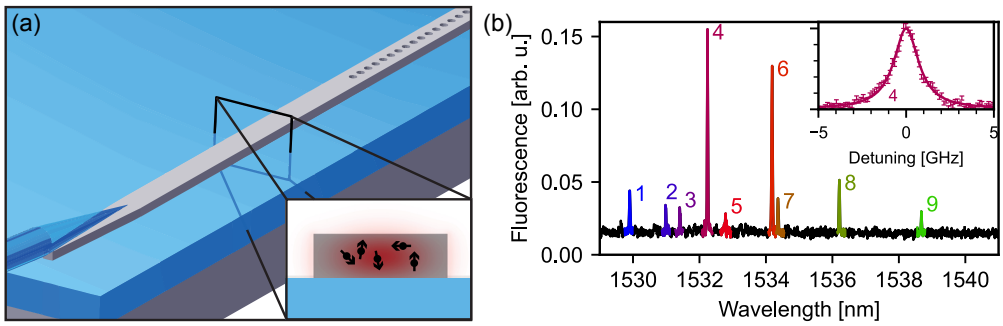

Figure 2.1.: **Resonant fluorescence spectroscopy in nanophotonic waveguides.** (a) Illustration of an experimental device (not to scale). Erbium dopants are integrated in a nanophotonic silicon waveguide (light grey) fabricated on a silicon-on-insulator (SOI) chip (buried-oxide (BOX) layer: blue, handle: grey). Light is efficiently coupled in and out of the waveguide by an adiabatic coupling interface formed by an inversely tapered waveguide end and a tapered optical fiber (blue cone). The other end of the waveguide is terminated by a broadband photonic crystal reflector formed by air holes. Bottom right inset shows the cross-section of the waveguide overlayed with its fundamental mode (red) and sketches the position of the dopants (black arrows). (b) In our first experiment, nine narrow peaks are found in the fluorescence spectrum between 1529 and 1539 nm after resonant excitation (Weiss et al. 2021). Inset: Lorentzian fits to the peaks show imhomogeneous linewidths of about 2 GHz.

silicon layer that is achieved using MBE or CVD techniques is comparable to ion implantation and limited by finite growth rates.

Thus, all these integration techniques have in common that they create a quasi two-dimensional doped region along the surface of the sample. This is a challenge for conventional photoluminescence or fluorescence spectroscopy techniques, where an excitation laser illuminates the sample perpendicular to the surface and thus to the two-dimensional doped region. Only a small fraction of the dopants is then within the laser spot. In addition, the high refractive index of silicon leads to a small critical angle for total internal reflection, and thus the outcoupling efficiency perpendicular to the two-dimensional layer into free space is small. This makes it difficult to study erbium ensembles with low dopant concentrations.

To overcome this, we have developed a novel approach and integrated erbium dopants into nanophotonic silicon waveguides extending in the two-dimensional doped region (Fig. 2.1 a) (Weiss et al. 2021). These waveguides provide sufficient fluorescence to study ensembles with low emitter concentrations. For this purpose, the ~ 220 nm-thin device layer of a commercially available silicon-on-insulator (SOI) wafers is homogeneously implanted with erbium dopants. Millimeter-long nanophotonic waveguides are then fabricated in these device layers. An efficient and broadband fiber-to-chip coupling

interface is realized by adiabatic side-coupling between a tapered waveguide end and a tapered optical fiber. On their other end, the nanophotonic waveguides are terminated with a broadband photonic crystal mirror.

Most previous experiments focusing on this material platform applied off-resonant excitation of the erbium dopants by creating free charge carriers in the conduction band. This above band-gap excitation mechanism is attractive for building solid-state lasers that could then be electrically pumped (Priolo et al. 1998; Kenyon 2005; Przybylinska et al. 1996). With this method, narrow photoluminescence lines and even indications for low optical gain were found (Ha et al. 2010). A major limitation of this off-resonant excitation is that it is sensitive only to the subsets of erbium dopants that couple efficiently to the conduction band. In contrast, resonant excitation is sensitive to all erbium dopants that decay predominantly radiatively. The lack of coupling to the electronic band structure seems even advantageous in the context of materials for quantum technologies as it reduces a potential source of decoherence. In addition, resonant excitation selectively addresses only one site at a time, which improves the signal-to-noise ratio.

In the first experiment of this kind, nine sharp resonances are observed in the fluorescence signal (Fig. 2.1 b) with a typical width of about 2 GHz (inset) (Weiss et al. 2021). This demonstrated that erbium dopants in nanophotonic silicon structures can be integrated at well-defined sites.

2.2. Implantation induced defects and impurities

Erbium implantation, even at low energies and doses, results in significant damage to the silicon host crystal in the form of lattice defects. These defects increase the optical absorption of the silicon layer to a level that hinders any optical measurements. To restore the transparency of the silicon, an appropriate thermal treatment during or after implantation is required. The thermal treatment partially heals the damage and restores the crystalline structure of the silicon matrix. Importantly, the thermal treatment must not recrystallize the silicon from its melt (melting point of silicon: 1687 K) which would cause all impurities, including the erbium dopants, to cluster and to diffuse to the surfaces.

In our first measurements, we examine samples that have been heated up to 1000 K for 10 min after the ion implantation step (Sec. 2.1, Fig. 2.1) (Weiss et al. 2021) as it has already been shown that erbium dopants in silicon become optically active under these conditions (Yin et al. 2013). Using similar implantation conditions, eight out of the nine resonances found in our sample and about 50 additional resonances are observed in erbium-doped silicon by another group (Berkman et al. 2023a) demonstrating the reproducibility of this result. Although the narrow inhomogeneous linewidths of these resonances are promising, their large number indicates a variety of different sites. This is detrimental for quantum applications that rely on a high optical depth at a single, well-defined site, e.g., ensemble-based quantum memory protocols including atomic frequency comb (AFC), electromagnetically induced transparency (EIT), or controlled reversible inhomogeneous broadening (CRIB).

Vacancy related defects		Interstitial related defects	
Defect	Temperature [K]	Defect	Temperature [K]
$V \cdot \mathrm{P}$	400	B_i	310
$V \cdot \mathrm{H}$, $V \cdot \mathrm{H}_2$	500	C_i	330
$V \cdot V$	550	$\mathrm{C}_i \cdot \mathrm{P}_s$	380
$V \cdot \mathrm{O}$	620	$\mathrm{Si}_i \cdot \mathrm{H}_2$	495
		$\mathrm{C}_i \cdot \mathrm{C}_s$	550
		$\mathrm{C}_i \cdot \mathrm{O}_i$	650

Table 2.1.: **Defects in silicon.** Selected intrinsic defects in silicon with annealing temperatures above room temperature. Temperature are rounded to multiples of 10 K. The defects are formed by vacancies V and the following elements: phosphor P, hydrogen H, oxygen O, boron B, and carbon C. The indices indicate interstitial i and substitutional s lattice positions. Data from (Watkins 2000).

At the same time, this large number of observed resonances is unexpected at first glance since silicon is a highly symmetric monoatomic crystal. Therefore, the incorporation of a single erbium dopant should result in only a limited number of possible integration configurations. A possible explanation for the large number of resonances is gettering of the erbium dopants, i.e., that they tend to form clusters with other dopants, impurities, or lattice defects. Assuming gettering, each site would be formed not just by a single erbium dopant at different lattice positions but by an erbium dopant surrounded by other erbium dopants, crystal defects, impurities, or a combination of these. Furthermore, gettering is consistent with the strong dependence of the properties of erbium dopants in silicon on implantation conditions, including different types of co-doping, on annealing conditions, and on the properties of the silicon layer, observed in various studies (Berkman et al. 2023a; Berkman et al. 2023b; Przybylinska et al. 1996; Kenyon 2005; Vinh, Ha, and Gregorkiewicz 2009; Ha et al. 2010). In particular, the increase in erbium solubility and photoluminescence intensity in silicon co-doped with oxygen suggests the formation of erbium-oxygen clusters (Kenyon 2005).

To achieve a higher integration yield on a single lattice site, we choose novel implantation and annealing conditions. The idea is to study erbium in pure silicon, i.e., to aim for a single erbium dopant surrounded only by silicon atoms. For this purpose, we prepare samples that satisfy two conditions. First, the silicon starting material should be as pure as possible, i.e., free of any other elements. Second, the annealing temperature should be significantly lower than 1000 K, at which erbium dopants in silicon start to become mobile (Kenyon 2005). In particular, the annealing temperature is chosen to be 800 K. This annealing temperature is still sufficient to heal most known crystal defects in silicon (Watkins 2000) (Tab. 2.1).

2.3. Sample preparation

In this chapter, ensembles of erbium dopants are studied in four different types of samples with properties listed in Table 2.2. All of these samples are based on commercially available SOI wafers from different suppliers (Subsec. 2.3.1). The samples are then implanted with erbium dopants (Subsec. 2.3.2). In addition, nanophotonic waveguides are fabricated on each of these samples (Subsec. 2.3.3).

The waveguides on three out of the four sample types are fabricated in-house. These three sample types differ in the crystal growth technique used for the silicon device layer, i.e., float zone (FZ), Czochralski (CZ), and chemical vapor deposition (CVD). In addition, the waveguides on the fourth sample type are fabricated in a commercial multi-project wafer (MPW) run at Advanced Micro Foundry (AMF). Accordingly, the four types of samples are labeled FZ, CZ, CVD, and AMF.

2.3.1. Starting material: Silicon-on-insulator wafers

The CVD samples are fabricated starting from a SOI wafer (University Wafer (UW)) with a silicon device layer thickness of 70 nm and a buried oxide layer (BOX) thickness of 2 µm. The CVD growth process is performed at the Lawrence Semiconductor Research Lab (LSRL). To prepare the top surface of the device layer for the growth process, the samples are baked in hydrogen for one minute at 1200 K. During this process, the top oxide and parts of the silicon device layer are evaporated. The top surface of the device layer is then used as the seed for the crystal growth. To this end, a silicon layer of around 0.14 µm is grown by chemical vapor deposition, resulting in a overall device layer thickness of about 0.19 µm. X-ray measurements show that the epitaxial layer has a single crystalline structure, and white-light interferometry confirms that the CVD-grown layer has a small surface roughness ($R_{rms} = 0.28(3)$ nm).

The CZ samples (Silicon Valley Microelectronics) have a comparable device layer thickness of 0.22 µm and a BOX layer thickness of 3 µm. In general, SOI wafers with a device layer thickness in this range are also called "thin SOI". In contrast, the FZ samples (Ultrasil) have an approximately ten-fold thicker device layer of 2 µm in thickness and a BOX layer of 1 µm in thickness. SOI wafer with such device layer thicknesses are called "thick SOI". The device layer thickness of the commercial AMF samples is also 0.22 µm, but the other properties of the wafer remain undisclosed by the foundry. In contrast to the FZ, CZ, and CVD samples, the nanophotonic structures on the AMF samples are fabricated prior to the implantation of erbium dopants.

The impurity concentrations in the CZ and CVD samples are characterized by secondary ion mass spectroscopy (SIMS) at RTG Mikroanalyse GmbH Berlin. In the CZ (CVD) samples, a carbon concentration of $1 \times 10^{17}\,\mathrm{cm}^{-3}$ ($2 \times 10^{16}\,\mathrm{cm}^{-3}$) and an oxygen concentration of $1 \times 10^{17}\,\mathrm{cm}^{-3}$ ($1 \times 10^{17}\,\mathrm{cm}^{-3}$) are found. The available SIMS characterization is not sensitive enough to measure the impurities in the FZ samples used in this work. In general, FZ crystal growth is crucible-free hence FZ silicon is expected to be significantly less contaminated with impurities, which is in good agreement with the thousand times higher specified resistivity of the FZ samples used in this work compared

Sample type	CZ	CVD	FZ	AMF
		Silicon-on-insulator wafer		
Manufacturer / vendor	SVM	UW, LSRL	Ultrasil	AMF
Device layer thickness [µm]	0.22	0.19	2	0.22
BOX thickness [µm]	3	2	1	undisclosed
Device layer bonding	smart-cut	smart-cut	bond-and-cut-back	undisclosed
Resistivity [$\Omega\,\mathrm{cm}$]	10(2)	unknown	> 10000	undisclosed
Doping concentration [cm^{-3}]	boron, 1×10^{15}	undoped (seed: unknown)	undoped	undisclosed
Carbon impurities [cm^{-3}]	1×10^{17} (*)	unknown	$< 1 \times 10^{16}$ (*)	undisclosed
Oxygen impurities [cm^{-3}]	1×10^{18} (*)	unknown	$< 1 \times 10^{16}$ (*)	undisclosed
		Erbium implantation		
Site	IBS	IBS	ELBE	IBS
Dose [$10^{12}\,\mathrm{cm}^{-2}$]	3.6	2.9	2, 20	3.6
Energies [MeV]	0.07, 0.16, 0.35	0.1, 0.35	1.5, 2.5, 4.0	0.07, 0.16, 0.35
Simulated peak concentration [cm^{-3}]	2×10^{17}	2×10^{17}	2×10^{16} and 2×10^{17}	2×10^{17}
Isotopic content	^{170}Er	^{170}Er, ^{167}Er (50 %:50 %)	all	^{170}Er
Angle	7°	7°	7°	7°
		Annealing		
Temperature [K]	800	800	800, 900, 1000	300, 700, 800, 900
During / post implantation	during	during	post	sweep

Table 2.2.: **Sample overview.** Properties of the silicon-on-insulator (SOI) wafers, implantation and annealing conditions of the different sample types investigated in this chapter. Abbreviations: Silicon Valley Microelectronics (SVM), Advanced Micro Foundry (AMF), Ion Beam Services (IBS), University Wafer (UW), Lawrence Semiconductor Research Lab (LSRL), and ELBE at Helmholtz-Zentrum Dresden-Rossendorf (ELBE).
(*): Literature values: (Ouaddah et al. 2019; Jakiela et al. 2018; Muiznieks et al. 2015)

to the CZ and the CVD samples. In the literature, typical values for the upper bound of oxygen and carbon impurities are between $1 \times 10^{15}\,\mathrm{cm}^{-3}$ and $1 \times 10^{16}\,\mathrm{cm}^{-3}$ (Ouaddah et al. 2019; Jakiela et al. 2018; Muiznieks et al. 2015).

2.3.2. Implantation and annealing

To maximize the fluorescence signal for a given peak dopant concentration, the implantation should target a homogeneous dopant distribution in the device layer. For a single implantation energy, the depth profile of the implantation is a Gaussian distribution. Thus, in order to obtain an approximately homogeneous depth profile, erbium dopants are implanted with multiple energies. For this purpose, the implantation depth profiles depending on the implantation energy are calculated numerically (Ziegler, James 2023). The resulting depths are further corrected by applying a heuristic correction factor (Palmetshofer, Gritsch, and Hobler 2001). Then, two or three implantation energies and suitable implantation doses are selected for each implantation run. The resulting implantation profiles are shown in Figure 2.2.

The CVD samples are implanted with two energies, 0.1 MeV and 0.35 MeV, for each of the isotopes ^{167}Er and ^{170}Er. The corresponding implantation doses are listed in Tab. 2.2. This procedure is performed at Ion Beam Services. During the implantation process, the samples are held at 800 K and mounted at an angle of 7° to avoid channeling. After the implantation, the samples are diced into pieces of 10 mm × 10 mm.

The CZ and AMF samples are implanted together at the same supplier and with a similar process as the CVD samples. To facilitate joint implantation, the CZ samples are diced into pieces of 10 mm × 10 mm. Multiple chips of both sample types are then attached to a silica wafer with double-sided tape. The silica wafer is then mounted in the implantation apparatus. In contrast to the CVD samples, only the isotope ^{170}Er is implanted. Furthermore, three different implantation energies are used instead of two to improve the homogeneous distribution of the ions. The implantation energies are 0.07 MeV, 0.16 MeV, and 0.35 MeV. The implantation doses are chosen accordingly. An approximately homogeneous erbium dopant concentration of $\sim 2 \times 10^{17}\,\mathrm{cm}^{-3}$ in the device layer is achieved for the CVD, CZ, and AMF samples. Furthermore, to compare the effect of the annealing temperature, additional batches of AMF samples are implanted at different temperatures, i.e., 300 K, 700 K, and 900 K.

The FZ samples are similarly diced into pieces of 10 mm × 10 mm before implantation and mounted on a silica wafer with double-sided tape. The FZ samples are then implanted in the Tandetron accelerator at ELBE at the Helmholtz-Zentrum Dresden Rossendorf. Due to their thick device layer, significantly higher energies are required to achieve a homogeneous distribution of erbium dopants throughout the device layer. Again, three different implantation energies are chosen: 1.5 MeV, 2.5 MeV, and 4 MeV. Two batches of FZ samples are implanted with different doses resulting in homogeneous erbium concentrations of $\sim 2 \times 10^{16}\,\mathrm{cm}^{-3}$ (FZ) and $\sim 2 \times 10^{17}\,\mathrm{cm}^{-3}$ (FZ high dose), respectively. Similar to the other samples, the erbium dopants are implanted with an angle of 7°. The FZ samples are implanted with the natural abundance of erbium isotopes since isotope selection is not available at ELBE. Furthermore, the sample temperature during

implantation cannot be controlled hence annealing during implantation is not possible. To overcome this, the FZ samples are annealed after implantation in a home-built rapid thermal annealing furnace. During this process, a sample is heated to a temperature of 800 K within 3 min. This temperature is stabilized for 1 min. Then, the sample starts to cool down with an initial ramp rate of about $7\,\mathrm{K\,s^{-1}}$ without active cooling.

2.3.3. Nanofabrication

The waveguides on the FZ, CZ, and CVD samples are fabricated following the same nanofabrication procedure. A detailed description of each step is given in App. A. Furthermore, the process of optimizing the nanofabrication is outlined in Sec. 4.3 for photonic crystal cavities which are more sensitive to imperfections than the nanophotonic waveguides measured in this chapter.

In short, the wafer pieces of 10 mm×10 mm are cleaned and spin-coated with a positive-tone electron-beam resist. The resist is then patterned by electron-beam lithography and developed in n-amyl acetate and methyl isobutyl ketone. Reactive-ion etching is applied to transfer this mask into the device layer. The etch process applied for the waveguide samples involves a mixture of argon (Ar), oxygen (O_2), and sulfur hexafluoride (SF_6). During the etch process, the samples are kept at cryogenic temperatures of about −100 °C. This etch process relies predominantly on physical Ar sputtering as the main etch mechanism. The mixture of O_2 and SF_6 passivates the sidewalls at cryogenic temperatures ensuring an anisotropic etch profile. In addition, SF_6 helps to transport individual silicon atoms away from the samples (de Boer et al. 2002).

2.4. Nanophotonic waveguides

The silicon device layer of the FZ samples is about ten times thicker than the device layer of the other sample types (Tab. 2.2). As a result, different nanophotonic waveguides and fiber-to-chip coupling schemes are required. To this end, rib waveguides are designed for the thick samples and ridge waveguides are designed for the thin samples (Subsec. 2.4.1). Due to their small cross-section, ridge waveguides modify the local photonic density of states and thus affect the optical lifetime in these waveguides compared to bulk crystals (Subsec. 2.4.2). In addition, the effect of erbium implantation on the propagation loss is characterized (Subsec. 2.4.3).

2.4.1. Design and fiber-to-chip coupling

On the CZ and CVD samples, ridge waveguides are fabricated which are defined by fully etched trenches (Fig. 2.2 b). The length of these waveguides ranges from 0.1 mm to 6 mm. The width of the ridge waveguides is typically 0.7 µm, unless specified otherwise. This value is a trade-off between the number of emitters that can be excited and measured, which increases with width, and the fraction of light that is guided in the fundamental TE-like mode, which decreases with width. For a width of 0.7 µm, at least one additional TE-like mode and one additional TM-like mode are also guided (Yamada 2011).

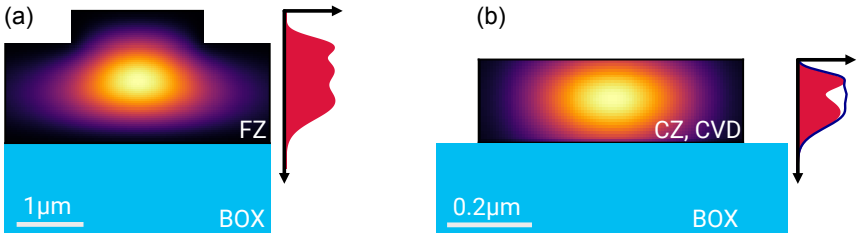

Figure 2.2.: **Different waveguide designs.** Different thicknesses of the silicon device layers require different waveguide designs to confine a single mode (intensity profile of fundamental mode shown in colors). (a) Rib waveguides are fabricated in the 2 µm thick device layer of the FZ samples. Erbium is implanted with three different energies resulting in an approximately homogeneous distribution of dopants within the device layer (red profile). (b) Ridge waveguides are fabricated on all other samples, i.e., CVD, CZ, and AMF, with device layer thicknesses ranging from 0.19 µm to 0.22 µm. Similarly, an approximately homogeneous distribution of dopants is achieved by two (CVD, red profile) or three (CZ and AMF, dark blue line) implantation energies.

Efficient and broadband side coupling to the ridge waveguides is engineered as depicted in Fig. 2.1. To this end, the waveguide is tapered to a tip width of about 0.1 µm over a length of 30 µm (Weiß 2022). This waveguide taper is then aligned with high precision to a tapered single-mode optical fiber. The tapered optical fibers used for this fiber-to-chip coupling scheme are fabricated in-house. In short, bare ends of optical fibers are dipped into hydrofluoric acid covered with silicone oil. This mixture is then gradually pumped out of the etching vessel with a syringe pump so that the fiber end becomes conically shaped. Further details can be found in (Weiß 2022; Nikbakht et al. 2015; Burek et al. 2017). This fiber-to-chip coupling scheme achieves one-way efficiencies of about 20 % for these waveguides (Weiß 2022) limited by the loss to the BOX layer. By removing the latter, one-way coupling efficiencies larger than 90 % are expected (Weiß 2022; Zeng et al. 2023).

The other end of each of the nanophotonic waveguides is terminated with a photonic crystal mirror formed by 30 air holes with a lattice constant of 0.33 µm. The design diameter of the holes ranges from 0.15 µm to 0.18 µm, which accounts for the different thicknesses of the respective device layers and provides increased robustness against fabrication imperfections.

Similar to the CZ and CVD samples, the waveguides on the AMF samples are also ridge waveguides but with a slightly smaller width, i.e., 0.5 µm. Again, broadband and efficient side-coupling is achieved by a tapered optical fiber and an inversely tapered waveguide end. The limited resolution of the applied optical lithography process prevents the fabrication of holes with a feature size smaller than 0.2 µm and thus the fabrication of photonic crystal mirrors. Therefore, instead of a photonic crystal reflec-

tor, the waveguides on the AMF samples are terminated with a loop reflector. The loop reflector is formed by a balanced 1×2-beamsplitter where the two arms are connected to form a loop.

On the FZ samples, rib waveguides are fabricated (Fig. 2.2 a) which support only a single optical mode despite their significantly larger cross-section (Powell 2002). By design, the width of the rib waveguides is 2 µm, and the trench depth is 0.45 µm.

The thick device layer prevents the fabrication of fully etched holes and waveguide bends for either photonic crystal or loop reflectors, and efficient off-chip coupling to a tapered optical fiber. Thus, the waveguides are fabricated over the entire $10\,\text{mm} \times 10\,\text{mm}$ chip so that the waveguides are terminated by the diced edges. The chip edges are then polished to create a smooth surface. Light can then be coupled from one of the rib waveguides to a cleaved single-mode fiber (SMF-28) positioned directly in front of the waveguide facet. The fiber is glued to this waveguide facet at room temperature. For this purpose, the sample is clamped on a fixed mount, and the fiber is positioned using a three axis stack of micrometer screws. The fiber position is optimized based on the light transmitted through the waveguide measured with an IR camera on the opposite facet of the waveguide. After optimization, the fiber is glued with an UV-curing low outgassing epoxy (Norland NOA 88).

The mode diameter of the single-mode fiber is still significantly larger than the mode diameter of the rib waveguide thus limiting the expected coupling efficiency to less than 5 %. At the same time, the coupling is more robust against displacement during the cooldown which is induced by different thermal contraction coefficients. The second facet of the waveguide is kept open without any dedicated mirror such that the only back reflection occurs at the silicon-air interface. Therefore, the fluorescence signal measured on the FZ samples originates mostly from ions emitting backwards, i.e., in the opposite direction to the excitation pulse. Future samples could be improved either by depositing a thin layer of a metal with high reflectivity, such as gold, on this second facet, or by gluing a second fiber to this facet, allowing simultaneous measurements at both ends of the waveguide.

2.4.2. Modification of the local density of states

For light fields with vacuum wavelengths of about 1.55 µm, the refractive index of silicon at cryogenic temperatures is 3.45 (Li 1980). Thus, in bulk silicon, these light fields exhibit wavelengths of about 0.45 µm. At the same time, the dimensions of the ridge waveguides on the thin-SOI samples with cross-sections of about $0.22\,\mu\text{m} \times 0.7\,\mu\text{m}$ are on the same scale. In this case, when the dimensions of a dielectric are comparable to the optical wavelength, the local density of states of the optical modes is affected. To get a qualitative understanding of this effect, the ridge waveguides are modeled numerically with MEEP, an open-source finite-difference time-domain (FDTD) software (Oskooi et al. 2010).

The simulation comprises electric dipole emitters which are placed in a ridge waveguide with a cross-section of $0.19\,\mu\text{m} \times 0.7\,\mu\text{m}$ corresponding to the CVD samples. The cross-sections of the CZ ($0.22\,\mu\text{m} \times 0.7\,\mu\text{m}$) and AMF ($0.22\,\mu\text{m} \times 0.5\,\mu\text{m}$) samples are only

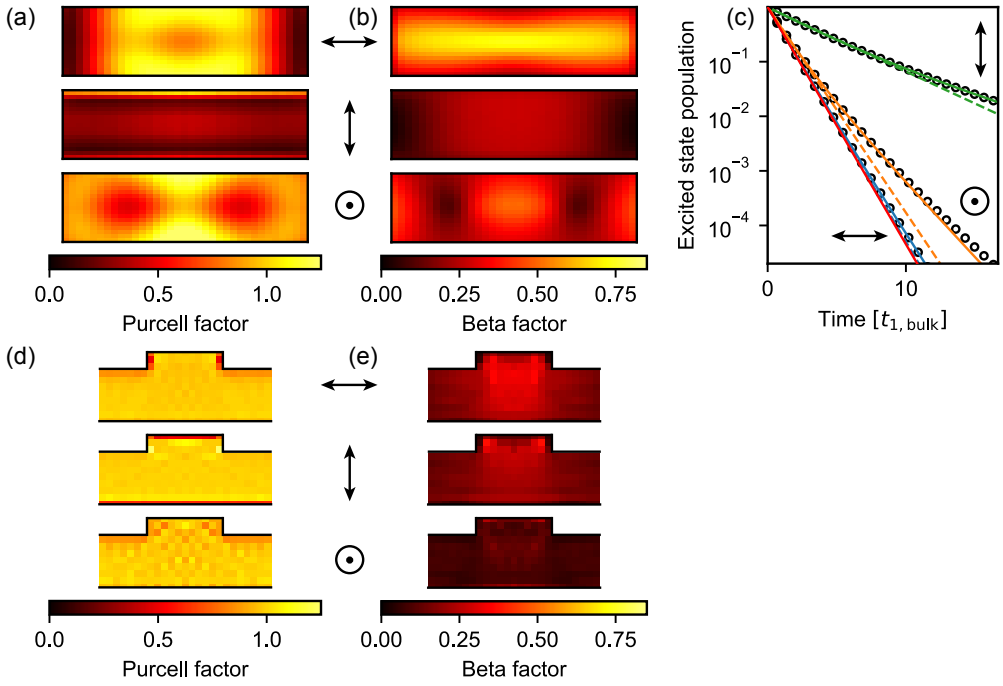

Figure 2.3.: **Modification of the local density of states in nanophotonic waveguides.** Purcell factors P and β-factors of the electric-dipole emission are modeled numerically by finite-difference time-domain (FDTD) calculations depending on the emitter position (cross-sectional images) and the dipole orientation (black symbols). (a, b) In ridge waveguides, which are fabricated on the CZ, CVD, and AMF samples, Purcell factors and β-factors strongly depend on the emitter position and the dipole orientation. In addition, the Purcell factors significantly deviate from the bulk value $F_P = 1$. (c) To model the effect on optical lifetime measurements in these waveguides, the temporal decay of the excited state probability for an ensemble of emitters with random position within the waveguide cross-section is calculated for the three dipole orientations (black circles). Single (dashed) and bi-exponential (solid) decays are fit to the data for each dipole orientation. The (fast) lifetimes extracted from these fits vary within a factor of ~ 3 and are longer than the actual bulk decay (red). (d, e) In contrast to the ridge waveguides, the rib waveguides on the FZ samples, which have a significantly larger cross-section, do not show a significant deviation of the Purcell factor from the bulk value and show smaller but more homogeneous β-factors. The rib waveguides are thus better suited to measure the optical lifetime of erbium dopants.

slightly different. Thus, a comparable effect is expected. The exact orientation of the dipole moments of the erbium transition is unknown. Therefore, dipoles oriented along all three main axes of the coordinate system are examined as an example. For each dipole orientation, the local density of states is calculated for different positions within the waveguide cross-section. The Purcell factor P, depending on the position $\vec{r}$ and the dipole orientation i of the emitter, is then calculated from these local densities of states (LDOS):

$$P_i\left(\vec{r},\omega\right) = \frac{\pi}{4\epsilon\left(\vec{r}\right)}\mathrm{LDOS}_i\left(\vec{r},\omega\right), \tag{2.1}$$

where ϵ is the dielectric function, and ω is the angular frequency. Figure 2.3 a shows the Purcell factor for the three dipole orientations within the cross-section of the waveguide. A Purcell factor of $P = 1$ corresponds to the Purcell factor in bulk silicon. The Purcell factor strongly depends on the dipole orientation and the position of the emitter within the waveguide cross-section. The maximum Purcell factor of about 1.2 is found for dipoles oriented along the width of the waveguide. The largest suppression ($P \sim 0.3$) of the emission is found for dipoles oriented along the height of the waveguide.

Similar to the local density of states, the small waveguide cross-section affects the probability to emit into a guided waveguide mode, i.e., the β-factor. The β-factor can be calculated from the ratio of the emission rate into the waveguide γ_{wvg} to the sum of all emission rates γ_{total}:

$$\beta = \frac{\gamma_{\mathrm{wvg}}}{\gamma_{\mathrm{total}}}, \tag{2.2}$$

For a purely radiative emitter, the β-factor can thus be calculated in a numerical model by comparing the intensity emitted into the waveguide with the total emitted intensity for a single electrical dipole.

Figure 2.3 b shows that the β-factor strongly depends on the dipole orientation and the emitter position, similar to the Purcell factor. The largest values of the β-factor are found at the center of the waveguide for a dipole oriented along the width of waveguide. Again, the smallest values for the β-factor are found for dipoles oriented along the height of the waveguide.

Importantly, the modification of the local density of states directly affects lifetime measurements in these nanophotonic waveguides. This effect is modeled numerically (Gritsch et al. 2022). In this model, an emitter $E(x, y, d)$ is represented by three random variables, i.e., the x- and the y-coordinates within the waveguide cross-section and the dipole orientation d. The ensemble of erbium dopants is represented by a large number of these emitters. The emitter positions within the waveguide cross-section are chosen from probability distributions representing the implantation profile (Fig. 2.2 b). In addition, each emitter is randomly assigned to one of the three dipole orientations. For each emitter, the Purcell factor is then extracted from the simulation data shown in Figure 2.3 a. From the Purcell factor, the optical lifetimes are calculated for each emitter. Next, the time-resolved ensemble fluorescence decay is calculated for each dipole orientation (Fig. 2.3, black dots). For this purpose, the fluorescence decays of all individual emitters with the same dipole orientation are weighted by their β-factors and

summed.

The model shows that the measured lifetime of ensembles of emitters in nanophotonic ridge waveguides depends significantly on both the dipole orientation and the emitter position. For all dipole orientations (colors), bi-exponential decays (Fig. 2.3 c, solid lines) fit the simulated data better than single exponential decays (dashed). Interestingly, the actual bulk decay (red, dotted) is faster than all single exponentials and all fast components of the bi-exponentials.

For comparison, the Purcell factor and the β-factor are also calculated for the rib waveguides on the FZ samples. Figure 2.3 d shows that for these waveguides, the Purcell factor is always close to one, independent of the dipole orientation and the position within the waveguide cross-section. Therefore, rib waveguides are more suitable than ridge waveguides for measuring the bulk lifetime of dipolar emitters. The β-factor in rib waveguides (Fig. 2.3 e) shows a slight dependence on the dipole orientation and the emitter position and is typically smaller than the β-factor in the ridge waveguides.

2.4.3. Implantation-induced propagation loss

The integration of erbium dopants into the nanophotonic waveguides can increase the optical propagation loss α. To analyze this effect, erbium-doped samples (type CVD) are compared with undoped reference samples from the same SOI wafer using our room-temperature characterization setup. Further details of this setup are given App. B. For this purpose, waveguides of different lengths L are fabricated on both samples. For each waveguide, the wavelength-averaged relative power, i.e., the ratio of the optical power after $P_{\text{reflected}}$ to before the P_{in} reflection at the sample, is measured:

$$\frac{P_{\text{reflected}}}{P_{\text{in}}} = R\eta^2 \exp\left(-2\alpha L\right). \tag{2.3}$$

The reflectivity R of the photonic crystal mirror and the fiber-to-chip coupling efficiency η can be altered by fabrication imperfections. To overcome this, the reflected power is measured on multiple structures for each waveguide length L. For each length, all but the structures with the highest relative power are then discarded. For the remaining structures, the coupling efficiency and the reflectivity of the mirror are close to their respective maxima: $\eta \simeq \eta_{\text{max}}$ and $R \simeq R_{\text{max}}$. Figure 2.4 shows the relative power for these remaining structures as a function of the waveguide length for both the doped and undoped samples. An exponential fit to each dataset allows extracting the propagation losses. The propagation loss is $\alpha_{\text{doped}} = 5.7(12)\,\text{dB}\,\text{cm}^{-1}$ for the doped sample and $\alpha_{\text{undoped}} = 3.5(12)\,\text{dB}\,\text{cm}^{-1}$ for the undoped sample, respectively.

In addition, the propagation loss is also investigated using nanophotonic ring resonators. To this end, ring resonators with a round-trip length of 70 µm are fabricated on a CVD sample. The individual modes of the ring resonators show quality factors of about 1×10^5. This allows us to calculate an upper bound for the propagation loss $\alpha_{\text{doped}} < 8(1)\,\text{dB}\,\text{cm}^{-1}$ (Bogaerts et al. 2012). This value is in good agreement with the first approach. In conclusion, the implantation of erbium dopants in silicon (with the dopant concentration of the CVD samples) could lead to a slight increase of the propa-

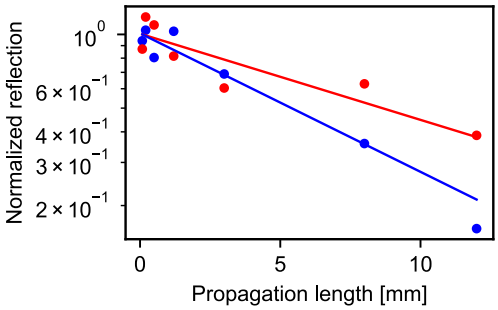

Figure 2.4.: **Implantation-induced loss in ridge waveguides.** The reflectance of waveguides with different lengths is measured on a CVD sample (blue) and an undoped reference sample (red). Exponential fits to the data reveal propagation losses of $\alpha_{\text{doped}} = 5.7(12)\,\text{dB}\,\text{cm}^{-1}$ and $\alpha_{\text{undoped}} = 3.5(12)\,\text{dB}\,\text{cm}^{-1}$ for the doped waveguides and undoped waveguides, respectively.

gation loss. The reason for this could be residual crystal damage which was not cured by the annealing step. Improving the annealing conditions could thus help to further reduce the propagation loss. A second possible explanation is that the roughness of the etched sidewalls might be increased for the implanted samples, leading to additional scattering loss.

2.5. Novel integration sites in silicon

After the nanofabrication, the samples with the erbium-doped waveguides are mounted in a closed-cycle cryostat with a base temperature of 2 K. The cryostat is equipped with a variable temperature insert (VTI) that allows the temperature to be adjusted between the base temperature and room temperature. For the spectroscopic characterization of the erbium dopants, a wavelength-tunable, continuous-wave laser is pulsed by acousto-optic modulators (AOMs) to resonantly excite the dopants. After the excitation laser is turned off, the fluorescence signal is recorded with superconducting nanowire single-photon detectors (SNSPDs). Further details on the cryogenic setup as well as the pulse shaping and data acquisition are given in App. B.

In the first measurement, the excitation wavelength is scanned from 1530 nm to 1540 nm where the intra-4f transitions are expected for erbium dopants. During the scan, the laser wavelength is modulated over approximately 1 pm to ensure that no narrow spectral features are missed. Figure 2.5 shows the recorded fluorescence integrated within the first 450 µs after an excitation pulse of 5 µs on an FZ sample. In this data, several narrow peaks are identified. Three of these peaks are approximately ten times brighter than the others. The three bright peaks have not been observed in previous studies, including our own work which investigated samples prepared with different annealing conditions (Sec. 2.1) (Weiss et al. 2021).

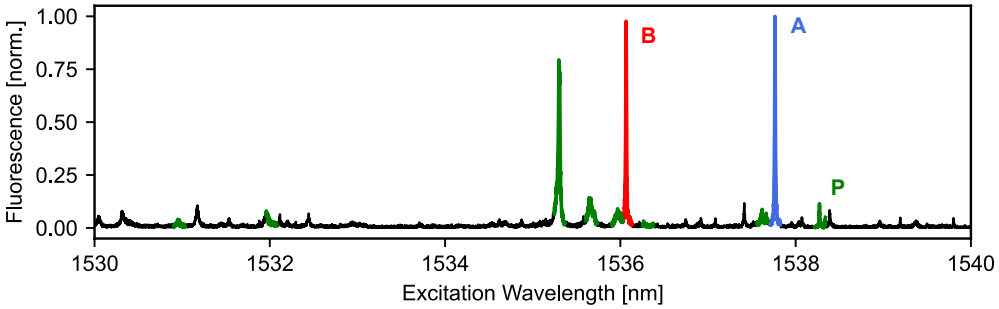

Figure 2.5.: **Novel integration sites in silicon.** The fluorescence spectrum of erbium dopants measured in the nanophotonic silicon waveguides shows several sharp resonances. The three bright resonances correspond to three previously unreported sites and are labeled (and colored) A (blue), B(red), and P (green). Sites A and B exhibit favorable properties for quantum applications and are the focus of this work.

To demonstrate the reproducibility of these novel sites, similar measurements are repeated on the three other sample types, i.e., CVD, CZ, and AMF (Fig. 2.6). Due to the different waveguide geometries and fiber-to-chip coupling efficiencies, the pulse power and pulse amplitude is optimized on each sample waveguide individually for the best signal-to-noise ratio of the bright peaks. The measured spectra on all four sample types are very similar despite the different starting materials, implantation conditions, and sample preparation methods (Sec. 2.3). This implies that the novel integration sites of erbium dopants in silicon are reproducible.

In the following sections, we will show that two of the three bright peaks correspond to erbium integration sites with favorable properties for quantum applications (Gritsch et al. 2022). These novel sites are named A and B and are colored blue and red throughout this chapter. The third bright site is named P for a precipitate or pair site and is colored green. This site has about twice as many crystal field levels in the excited state manifold (Gritsch et al. 2022) as possible for a single erbium dopant. This indicates that site P involves at least two erbium dopants. Moreover, the integration yield of site P relative to the integration yield of sites A and B increases with implantation dose, e.g., from the FZ samples to the FZ (high dose) samples (Weiß 2022). Overall, these properties of site P do not seem attractive for quantum technology applications. Therefore, site P will not be discussed further in this thesis. Details can be found in (Gritsch et al. 2022; Weiß 2022).

The remaining narrow peaks observed in Figure 2.6 have not yet been investigated. In principle, these sites could also have interesting properties and could therefore be studied in future experiments. A certain disadvantage of these sites is the low yield on these sites for the novel implantation and annealing conditions compared to the yield on sites A and B.

In addition to the three bright sites, i.e., A, B and P, and the other narrow peaks, a

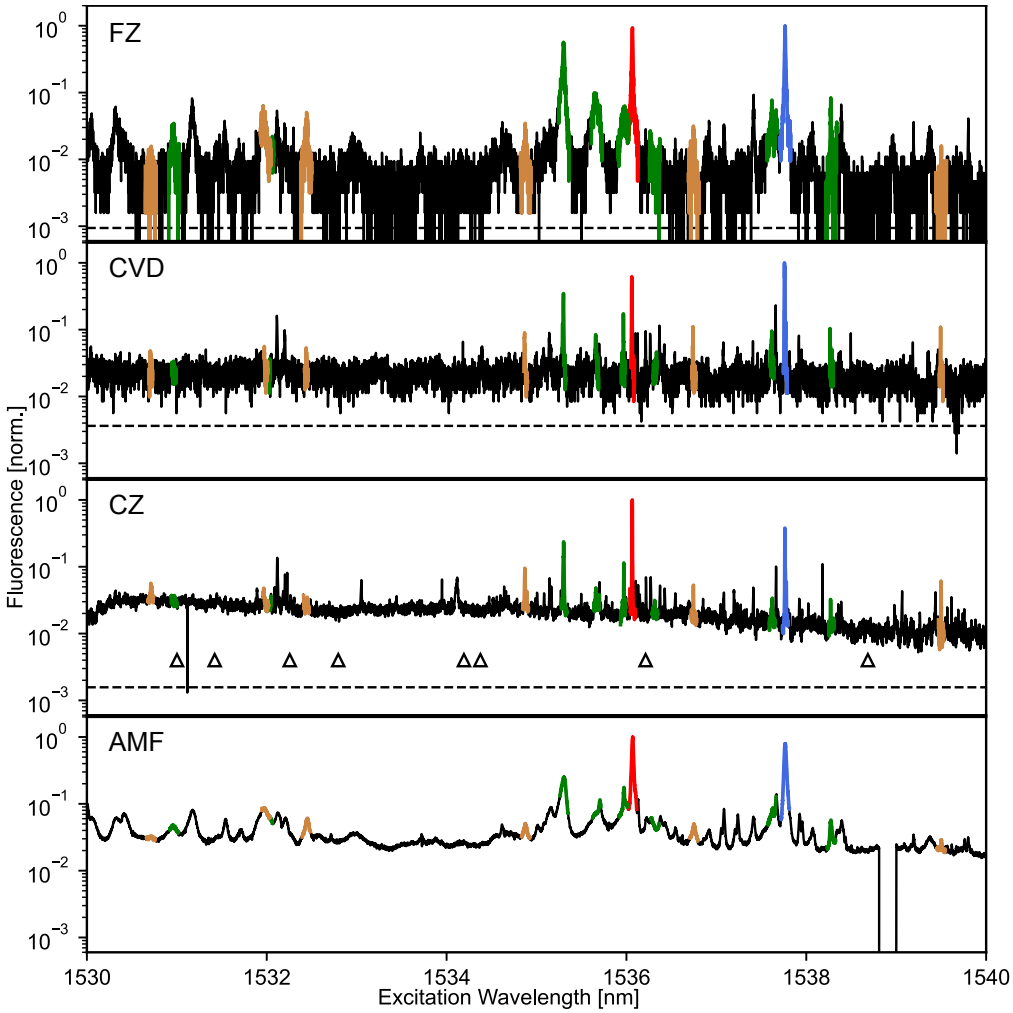

Figure 2.6.: **Reproducible integration of erbium dopants in silicon.** Comparing the flourescence spectra measured on the four different sample types FZ, CVD, CZ, and AMF shows that erbium dopants integrate reproducibly at sites A, B, P, and O under the novel annealing conditions motivated in Section 2.2 independent of the starting material. These sites are fundamentally different than the sites found in previous work on a CZ sample prepared with different annealing conditions indicated by the black triangles at the bottom of the CZ panel (Weiss et al. 2021).

broadband background is observed in the fluorescence signal (Fig. 2.6). The emission spectrum of this background shows several sharp peaks, independent of the excitation wavelength. Therefore, this background can be explained by the creation of free charge carriers in the conduction band of silicon. Furthermore, the sharp resonances in the emission spectrum indicate the presence of at least one optically active site. The optically active site is labeled O and colored brown. Similar to site P, site O will not be discussed further. Details can be found again in (Gritsch et al. 2022; Weiß 2022).

The broadband background significantly reduces the signal-to-noise ratio. The background, and thus the free charge carriers, seems to originate from erbium dopants since it is observed predominantly in the wavelength range between 1530 nm to 1545 nm and strongly suppressed at longer wavelengths. In addition, two-photon absorption is expected to be negligible for the optical intensities in the waveguides during the excitation pulses in undoped silicon (Sinclair et al. 2019).

The smallest relative amplitude of the background is observed in the FZ samples. One possible explanation is that the free charge carriers in the rib waveguides can diffuse into regions where the β-factor is very small before recombining. In contrast, in ridge waveguides, the diffusion of the free charge carriers is stopped at the sidewalls of the waveguide where the β-factor is still significant. Another explanation is that free charge carriers contributing to the broadband background are created at clusters of multiple dopants and impurities. The reduced relative background fluorescence in the FZ samples could then also be explained by the ten times lower peak concentration of erbium and the smaller concentrations of oxygen and carbon relative to erbium concentration (Tab. 2.2). The latter would be in good agreement with previous studies showing that co-implantation of oxygen also increases the photoluminescence intensity and the optical activity of erbium in silicon (Kenyon 2005; Vinh, Ha, and Gregorkiewicz 2009).

2.6. Crystal field

We begin our study of sites A and B by measuring the crystal field levels (Fig. 1.1 c). For this purpose, a tunable narrowband filter with a full width at half maximum (FWHM) of 0.11 nm is inserted into the detection path of the experiment. First, this filter is tuned on resonance with the transitions between the lowest crystal field levels (Z_1 - Y_1, Fig. 1.1), i.e., 1537.76 nm for site A and 1536.06 nm for site B (Fig. 2.5). To identify the remaining levels in the crystal field manifold of the optical excited state, the excitation wavelength is scanned to shorter wavelengths, and the fluorescence after the excitation pulse is recorded for each site (Fig. 2.7 a). The peaks observed in the fluorescence spectrum correspond to the transitions between Z_1 and the excited state crystal field levels. For site A and site B, seven excited state crystal field energy levels are observed. This corresponds to the maximum number of excited state crystal field levels for a single erbium dopant in the ${}^4I_{\frac{13}{2}}$ manifold. The degeneracy of the spin-orbit states is thus completely lifted indicating that the erbium dopants are integrated on a site of low symmetry (Liu and Jacquier 2005). Subsequently, the excitation laser is tuned to the brightest peak in the excited state crystal field manifold (Z_1 - Y_2 for both sites). This is

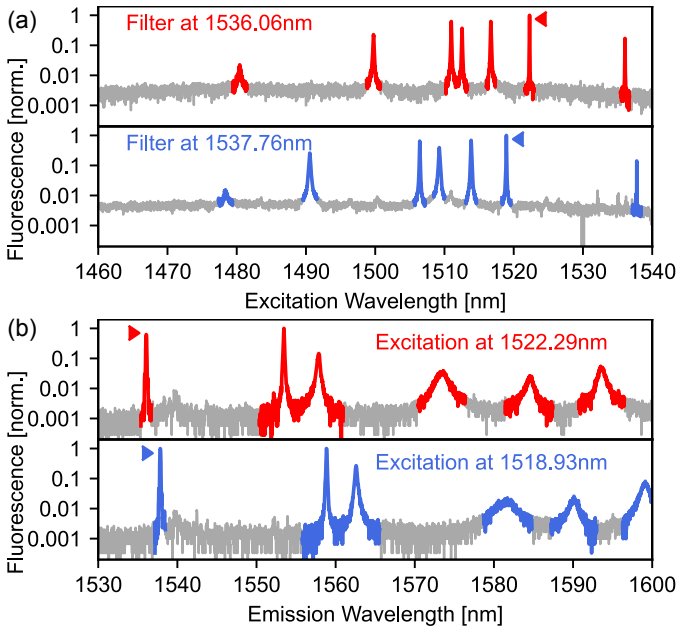

Figure 2.7.: **Crystal field spectroscopy**. Inserting a tunable narrowband filter in the detection path allows determining the crystal field energy levels in the ground and excited state. (a) The narrowband filter is tuned on resonance (triangles in panel b) with site A (blue) and site B (red), respectively, and the excitation laser is scanned to shorter wavelengths. The resonances correspond to the transitions from the lowest-lying energy level in the ground state to the excited state energy levels. (b) The excitation laser is then kept at the brightest resonance (triangles in panel a), and the narrowband filter is tuned to longer wavelengths for each site. The resonances correspond to the transitions from the lowest-lying energy level in the excited state to the ground state energy levels.

possible because the timescale on which the excitation decays via phonons within each crystal field manifold, i.e., to Y_1 and Z_1, is much faster than the optical decay (Liu and Jacquier 2005). The narrowband filter is then scanned to longer wavelengths (Fig. 2.7 b). The energy levels in the optical ground state crystal field manifold are extracted from the positions of the resonances in the resulting emission spectra. Eight energy levels are resolved in the ground state manifold which is expected for dopants in the ${}^4I_{\frac{15}{2}}$ configuration on a low symmetry site. Six of them are shown in Fig. 2.7 b, and the remaining two are found at longer wavelengths (Tab. 2.6). The crystal field splitting in the ground state is thus consistent with the splitting in the excited state.

The extracted crystal field splittings are summarized in Table 2.3. The energy splitting between the two lowest-lying crystal field levels of site A and site B is larger than in any

	Ground State	
CF level - Z_1	**site A** [GHz]	**site B** [GHz]
Z_2	2634.2	2186.5
Z_3	3095.9	2730.5
Z_4	5388.9	4636.1
Z_5	6414.3	5969.1
Z_6	7477.9	7045.8
Z_7	9456(10)	8461(10)
Z_8	12 264(10)	12 095(10)
	Excited State	
CF level - Y_1	**site A** [GHz]	**site B** [GHz]
Y_2	2417.9	1766.3
Y_3	3080.9	2492.8
Y_4	3685.3	3035.6
Y_5	4057.0	3241.2
Y_6	6175.9	4725.9
Y_7	7832.5	7334.7

Table 2.3.: **Crystal field levels.** The frequency splittings of the crystal field (CF) levels in the excited and the ground states for sites A and B. The smallest energy splittings in both the ground state and the excited state exceed the crystal field splittings reported for erbium dopants for any other material (Tab. 2.6).

other known host (Tab. 2.6). In particular, site A exhibits splittings of 2634(1) GHz in the ground state and 2187(1) GHz in the excited state. Site B shows only slightly smaller splittings of 2418(1) GHz and 1766(1) GHz for the ground and the excited states, respectively. Large crystal field splittings are generally beneficial because they set the temperature scale for the Orbach process. The Orbach process is a spin-lattice relaxation process that reduces the electron spin lifetime and thus can limit the optical coherence. This effect will be studied in detail later in this chapter (Sec. 2.9).

In addition, the branching ratio of the direct decay from the lowest level of the excited state Y_1 to the lowest level of the ground state Z_1 is measured. This branching ratio is important because this is the transition between the long-lived crystal field levels in the ground and excited manifold. This property is thus required for the calculation of the Purcell enhancement of the erbium dopants in optical resonators which will be discussed later in this work (Chap. 3). The branching ratio is measured by calibrating the transmission through the filter and then measuring with and without the filter. A

branching ratio of 23(5) % is obtained for both sites (Gritsch et al. 2022). The large uncertainty of this value results from the decrease of both the detector efficiency and the transmission of the fiber optical elements for longer wavelengths. In addition, the different decays may have different dipole orientations which can induce a systematic error in the branching ratio because each transition would then have a different effective β-factor.

2.7. Inhomogenenous broadening and erbium integration

On the FZ, CZ, and CVD samples, erbium dopants integrated on site A and site B exhibit inhomogeneous broadenings (Tab. 2.4) that are comparable to or narrower than the inhomogeneous broadening observed for other sites in previous studies. These narrow broadenings indicate that the dopants are integrated at well-defined lattice sites and that the dopants are not inducing large inhomogeneous strain fields in their local environments. The inhomogeneous broadening is determined by fitting a Lorentzian distribution to the fluorescence after resonant excitation. Similar to the crystal field measurements, the fluorescence signal is filtered using the tunable narrowband filter. In contrast to the previous measurements, the excitation laser frequency is no longer modulated and the excitation power is reduced to avoid artificial line broadening.

The smallest inhomogeneous broadenings are measured on the CZ sample where a FWHM of 0.46(1) GHz is extracted for site A and a FWHM of 0.50(1) GHz is extracted for site B (Fig. 2.8) (Gritsch et al. 2022). Similar values for the FWHM are measured on the CVD sample. However, instead of a single peak, each site splits into two peaks with a separation of 0.65(1) GHz for site A and 0.36(1) GHz for site B. This double peak structure could be caused by inhomogeneous strain distributions resulting from the CVD growth (Subsec. 2.3.1) or by the two isotopes which have been implanted in these samples.

The FZ samples show considerably broader lines, i.e., 0.96(1) GHz for site A and 1.07(1) GHz for site B despite the approximately tenfold lower concentration of erbium dopants. This suggests that the dominant broadening mechanism is caused by the implantation process itself due to the higher implantation energies necessary to achieve a homogeneous dopant concentration in the thicker device layer. This is consistent with the approximately tenfold broader lines (A: 7.8(1) GHz, B: 13.9(1) GHz) measured on the FZ (high dose) sample which has a tenfold higher erbium concentration than the FZ samples (Weiß 2022). To further test this hypothesis, another FZ (high dose) sample is annealed at 900 K instead of 800 K (Tab. 2.2). This leads to a significant reduction of the inhomogeneous linewidth to 1.8(1) GHz for site A and to 3.8(1) GHz for site B. To further investigate this trend, another FZ (high dose) sample is annealed to 1000 K, a common annealing temperature in previous studies, including our own work (Weiss et al. 2021), again with a hold time of 1 min. At this temperature, erbium dopants in silicon start to become mobile (Kenyon 2005). Strikingly, after annealing at this temperature, sites A and B are no longer observed. This indicates that erbium dopants have formed clusters with other impurities or other erbium dopants. These results further imply that

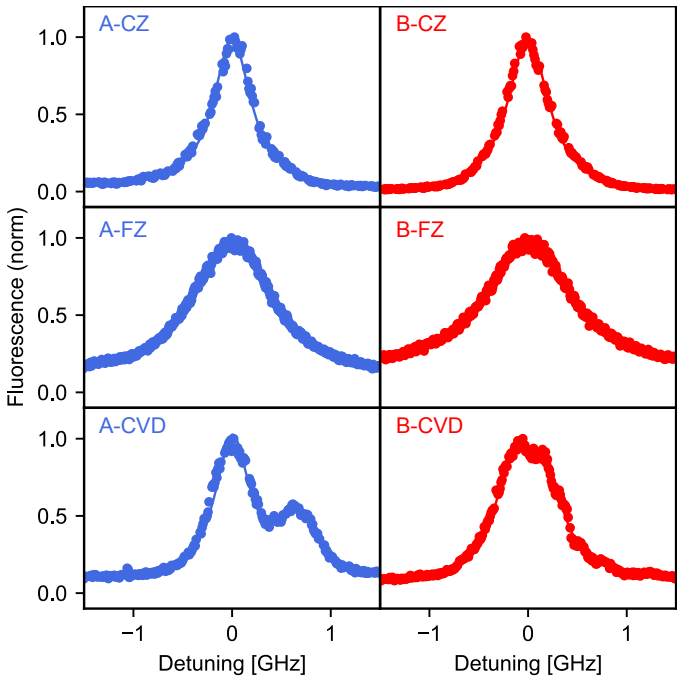

Figure 2.8.: **Inhomogeneous broadenings.** Filtered resonant fluorescence after resonant excitation of dopants integrated on sites A and B. The narrowest inhomogeneous broadening is observed in the CZ samples (top). The larger broadening observed for the FZ samples (center) is attributed to additional implantation-induced damage and the natural abundance of isotopes. The linewidth of the CVD samples (bottom) is comparable to the CZ, but a double peak is clearly visible.

the annealing conditions can still be optimized. Unfortunately, further studies with different annealing conditions using the FZ or the FZ (high dose) samples were not possible due to the limited amount of wafer pieces available.

Instead, samples of type AMF are used for further investigation. For this purpose, AMF samples are implanted at room temperature, 700 K, 800 K, and 900 K (Rinner et al. 2023). The residual crystal damage on the sample which was implanted at room temperature is too large for any optical measurements. Sufficient transparency of the silicon waveguides is restored when the sample temperature is kept at 700 K during the implantation process. On this sample, erbium dopants are again observed at sites A and B with inhomogeneous broadenings of 3.3(1) GHz and 1.8(2) GHz, respectively. These broadenings are significantly larger than the values found for the CZ, CVD, and even the FZ samples. Similar values are also found for implantation at 800 K and for the sample implanted at room temperature after an additional annealing step at 800 K using the same recipe and conditions as for the FZ samples (Tab. 2.4). The combination of the

Sample	Isotopes	Annealing: Temperature [K]	Annealing: during / post implantation	Inhomogeneous Linewidth: site A [GHz]	Inhomogeneous Linewidth: site B [GHz]
CZ	^{170}Er	800	during	0.46(1)	0.50(1)
FZ	all	800	post	0.96(1)	1.07(1)
CVD	^{170}Er, ^{167}Er	800	during	double peak 0.40(1)	double peak 0.44(1)
FZ (high dose)	all	800	post	7.8(1)	13.9(4)
FZ (high dose)	all	900	post	1.8(1)	3.8(1)
FZ (high dose)	all	1000	post	not visible	not visible
AMF	^{170}Er	700	during	3.3(1)	1.8(2)
AMF	^{170}Er	800	post	3.3(1)	2.4(1)
AMF	^{170}Er	800	during	double peak 3.8(5)	1.4(2)
AMF	^{170}Er	900	during	not visible	not visible

Table 2.4.: **Inhomogeneous linewidths depending on sample type and implantation conditions.** The inhomogeneous linewidths of the erbium dopants observed on the CZ and CVD samples are comparable to the narrowest inhomogeneous linewidths for erbium dopants in any known host crystals (Tab. 2.6). Further, the inhomogeneous linewidth is a good indicator for studying the effect of annealing on implantation-induced damage of the host crystal. For the FZ (high dose) samples, the inhomogeneous linewidth is significantly reduced with increasing annealing temperature indicating potential for further improvement. In contrast, the inhomogeneous linewidth on the AMF samples shows no clear dependence on the annealing temperature implying other sources for the inhomogeneous broadening. In addition, sites A and B disappear at different annealing temperature in the FZ (high dose) and AMF samples, which is attributed to additional impurities clustering with the erbium dopants in the AMF samples, which become mobile at already at lower temperatures.

broadened lines and the different dependence on the annealing temperature indicates that the AMF samples exhibit different dominant broadening mechanisms compared to the other samples. A possible explanation is that, in contrast to the other samples, the nanophotonic structures are fabricated prior to implantation such that the erbium dopants are directly implanted into the waveguides. Moreover, the silicon device layer of the AMF samples may be contaminated with more or different impurities than the silicon device layers of the other samples. This hypothesis is strengthened by the observation that already at an annealing temperature of 900 K, sites A and B are no longer observed in the AMF samples.

In conclusion, strain fields stemming from implantation-induced damage still broaden the inhomogeneous linewidth. Thus, further optimization of the implantation and annealing conditions may result in even narrower lines. In addition, residual broadening is caused by strain sources not associated with ion implantation, i.e., different thermal expansion coefficients of the silicon and the BOX layers as well as the mixed isotopic composition of the crystal and residual impurities. The amount and nature of the latter depend on the purity of the starting material. As a result, the optimal implantation and annealing conditions may ultimately depend on the starting material, particularly in the presence of impurities that become mobile at temperatures below the onset of erbium mobility and tend to cluster with erbium dopants at the same time.

In future experiments to further optimize the annealing and implantation conditions, the absolute integration yield at a given site should also be determined and included in the comparison. So far, this has been hindered by the different fiber-to-chip coupling efficiencies, waveguide losses, and by changes in the optical setup in between the measurements. Furthermore, the heating and cooling rates during annealing are of the same order of magnitude or even longer than the actual holding times at the designated annealing temperature. To further optimize this, a rapid thermal annealer with higher heating rates and active cooling seems attractive. As an alternative, even higher ramp rates are expected once individual waveguides can be annealed directly with a laser. With these improvements, a better understanding of the underlying microscopic processes is expected.

2.8. Optical lifetime

To measure the optical lifetime, the narrowband filter is tuned on resonance with the transition between Y_1 and Z_1. For the best signal-to-noise ratio, the erbium dopants are excited at the brightest crystal field level (Y_2 for both sites). This also ensures that the resonant background contribution to the signal, which has a different lifetime from the dopants on the sites A and B, is negligible. The time-resolved fluorescence is integrated in frequency within one inhomogeneous linewidth for each site (Fig. 2.9). For the rib waveguides on the FZ samples, the resulting decay is fit with a single exponential decay for each site. From these fits, optical lifetimes of 142(1) µs and 186(1) µs are extracted for sites A and B, respectively. These values correspond to the bulk lifetimes of sites A and B since the Purcell factor is not significantly modified in the rib waveguides (Sec. 2.4)

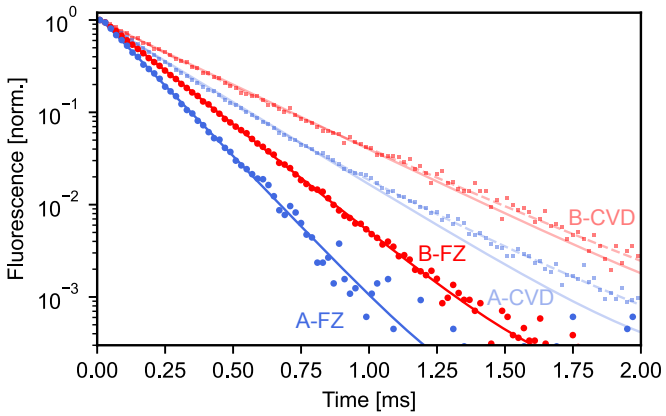

Figure 2.9.: **Optical lifetime.** The time-resolved resonant fluorescence decay is measured after excitation of a higher crystal field to avoid resonant background contributions on the FZ (dots) and CVD (squares) samples. The lifetimes extracted from single exponential fits (solid lines) to the data for sites A (blue) are shorter than for site B (red). The lifetimes of 142(1) µs for site A and 186(1) µs for site B observed in the rib waveguides on the FZ sample correspond to the bulk lifetime of the erbium dopants. In contrast, the local density of states in the ridge waveguides on the CVD samples is modified such that slower decays are found which are better described with bi-exponential fits (dashed).

The observed optical lifetime is more than an order of magnitude shorter than the lifetime of erbium dopants in all other known host crystals. These optical lifetimes are also significantly shorter than the expected lifetime of about 2.4 ms for a purely magnetic dipole transition despite the silicon large refractive index of silicon, i.e., $n_{\mathrm{Si}} = 3.45$ (Dodson and Zia 2012). Instead, this observation implies that the erbium dopants on sites A and B exhibit an electric dipole transition induced by the host material. Furthermore, the fast optical decays may indicate that these dopants are integrated on interstitial rather than substitutional sites. For interstitial sites in silicon, the local correction factor is about ten times larger than for substitutional sites (de Vries and Lagendijk 1998). Interstitial sites seem also consistent with the large crystal field splittings assuming that the perturbation of the free-space Hamiltonian of the erbium dopants induced by the silicon atoms increases with a shrinking distance between them and the erbium dopant (Sec. 2.6).

In contrast to the FZ samples, the Purcell factor is modified in the ridge waveguides of the CVD samples. As expected from the model (Sec. 2.4), the decay is better fit with a bi-exponential fit whereby both extracted timescales are slower than the bulk decay. An exact quantitative modeling that would allow a parameter-free fit to the decay requires a detailed understanding of the dipole strengths and orientations of the erbium sites.

To rule out that different lifetimes are caused by the different sample preparation

techniques, an additional CZ sample is fabricated with ridge waveguides of different cross-sections. On this sample, the waveguide width is varied from 0.45 µm to 0.9 µm. As expected, the optical lifetime observed for these waveguides decreases from narrower to wider waveguides. This confirms that the different lifetimes observed in different ridge waveguide geometries are a consequence of the modification of the photonic density of states. Furthermore, the dependence of the measured lifetime on the photonic density of states implies that the decay from the optically excited state to the ground state is predominantly radiative (Gritsch et al. 2022).

2.9. Homogeneous linewidth

For quantum technologies based on the exchange of photons, optical coherence of the emitters is a fundamental requirement. The established method for measuring the optical coherence of an ensemble of emitters is the photon echo technique (Liu and Jacquier 2005). For the ensembles of erbium dopants in the nanophotonic silicon waveguides, no photon echoes could be observed so far. In these samples, several effects impede this measurement technique which are discussed in the following:

First, a photon echo is a collective effect that relies on coherent rephasing of many emitters. Therefore, a sufficiently large number of emitters is required. In the nanophotonic waveguides, the concentration of dopants at the sites of interest is small. Optimizing the integration yield at sites A and B will help to increase the number of emitters present in future samples. In addition, longer waveguides will also increase this number as long as the propagation loss is negligible.

Second, in the samples studied in this work, the silicon is not isotopically purified. The natural abundance of ^{29}Si, which carries a nuclear spin, is about 5 %. Thus, erbium dopants can interact with ^{29}Si nuclear spins via the superhyperfine interaction leading to a fast collapse of the echo signal. The effect of these nuclear spins can be frozen out by applying large magnetic fields (Car, Le Gouët, and Chanelière 2020) or avoided by using transitions between hyperfine states of ^{167}Er (Ortu et al. 2018). Alternatively, the effect of the ^{29}Si can be eliminated by studying erbium dopants in isotopically purified samples.

The third effect that may prevent the observation of photon echoes is induced by the excitation pulses. For the latter, large excitation pulse powers are desirable because the visibility of photon echoes is expected to increase with stronger but shorter, and thus spectrally broader, pulses. However, in the samples studied in this work, the fluorescence stemming from the broadband background increases with the excitation pulse power. The broadband background is related to the creation of free charge carriers in the conduction band (Sec. 2.5) by the excitation pulses. The free charge carriers can induce electric fields at the positions of the erbium dopants or change the state of localized charge traps. In this case, the transition frequency of the erbium dopants could be Stark-shifted. The excitation pulses then effectively cause instantaneous spectral diffusion preventing the coherent rephasing and thus the emission of a photon echo. To overcome this, the integration yield of erbium dopants at sites contributing to the

broadband background should be minimized. If this is not possible, the nanophotonic waveguides could also be integrated into a suitable p-i-n diode (Lodahl, Mahmoodian, and Stobbe 2015; Anderson et al. 2019; Appel et al. 2021). In such a configuration, the charge carriers created during the excitation pulses may be removed fast enough from the surroundings of the erbium dopants to reduce the instantaneous spectral diffusion. Furthermore, even without the creation of free charge carriers, exciting neighboring erbium dopants may lead to instantaneous spectral diffusion if either the electric dipole, the magnetic dipole, or the locally induced strain field differs between the optical ground state and the excited state (Louchet-Chauvet et al. 2023). In this case, a reduction of the dopant concentration in the waveguides or spectrally narrower pulses that address only a fraction of the dopants might be necessary.

In addition to the spectral diffusion caused by the excitation pulses, the emitters could be exposed to spectral diffusion from other sources. One possible source are residual paramagnetic impurities that can interact with the erbium spins. Similar to ^{29}Si, the detrimental effect of these impurities can be overcome by freezing them out at large magnetic fields (Rinner et al. 2023) or by removing them from the starting material. Furthermore, spectral diffusion could also be caused by two-level systems or charge traps at the surfaces of the nanophotonic structures. To reduce the resulting electrical noise, the integration of the waveguides into p-i-n diodes seems promising again.

In conclusion, the photon echo technique is not very well suited to study the optical coherence of the erbium dopants in the samples studied in this work. As an alternative, the optical coherence time T_2 can be inferred indirectly by measuring the homogeneous linewidth γ_0 of the erbium transition. The homogeneous linewidth is related to the optical coherence as follows:

$$T_2 = \frac{1}{2\pi\gamma_0}. \tag{2.4}$$

In the following, a transient spectral holeburning scheme to measure the homogeneous linewidth using only weak excitation pulses is introduced (Subsec. 2.9.1). This scheme is then applied to extract an upper bound for the homogeneous linewidth by varying the intensity of the excitation pulses (Subsec. 2.9.2). The homogeneous linewidth is further investigated as a function of the sample temperature (Subsec. 2.9.3). In addition, persistent spectral holes are observed which are attributed to the polarization of the electronic spin states (Subsec. 2.9.4). Furthermore, measuring the homogeneous linewidth allows an order of magnitude estimate of the integration yield at sites A and B (Subsec. 2.9.5). Finally, we show that similar values for homogeneous linewidth are found with the measurement scheme introduced in (Berkman et al. 2023a) (Subsec. 2.9.6).

2.9.1. Measuring the homogeneous linewidth using weak pulses

The measurement scheme to characterize the homogeneous linewidth using weak excitation pulses was pioneered for erbium dopants by our group (Weiss et al. 2021) inspired by previous work with other emitters (Szabo 1975). The scheme is called transient spectral hole burning and allows measuring the power-broadened homogeneous linewidth $\gamma_{\mathrm{hom}}(I)$. For this purpose, the ensemble of emitters is excited by N laser fields with

equidistant detunings δ and intensities I (Fig. 2.10 b, inset). The measurement scheme is qualitatively understood by comparing the fluorescence S expected from an ensemble of emitters in two regimes. In the first regime, the detuning between the laser fields is much larger than the power-broadened homogeneous linewidth. In this case, the different laser fields address different subsets of the inhomogeneously broadened ensemble. Then, the fluorescence depends linearly on the number of laser fields:

$$S \propto N, \text{ for } \delta \gg \gamma_{\text{hom}}(I). \tag{2.5}$$

In the second regime, the detuning between the laser fields is much smaller than the power-broadened homogeneous linewidth. Then, the equidistant laser fields address the same emitters, and the fluorescence follows the saturation laws, i.e., it increases with a square root dependence on the number of laser fields:

$$S \propto \sqrt{N}, \text{ for } \delta \ll \gamma_{\text{hom}}(I). \tag{2.6}$$

In both cases, the frequency span of the equidistant laser fields is assumed to be significantly smaller than the inhomogeneous broadening: $N\delta \ll \gamma_{\text{inhom}}$.

We model this measurement scheme numerically. In this model, an emitter $E(x, y, \omega_0)$ is defined by three random variables. Similar to the model in Subsec. 2.4.2, x and y represent the coordinates of the emitter within the waveguide cross-section. For simplicity, we assume the same dipole orientation for all emitters. From the mode profile of the waveguide (Fig. 2.2), the intensity $I(x, y)$ of the laser fields at the position of each emitter can be calculated. The third parameter, ω_0, represents the transition frequency of the emitter and is a random variable with a Lorentzian probability distribution (FWHM: 0.5 GHz, Sec. 2.7) to account for the inhomogeneous broadening. The dynamics of the excited state probability p_e for each emitter in the presence of N laser fields is described by the rate equation for a two-level system:

$$\frac{d}{dt}p_e = -Ap_e - (2p_e - 1)\sum_{i=1}^{N}\sigma_i\Phi_i. \tag{2.7}$$

In this equation, A is the spontaneous emission rate. The term describing the stimulated emission and absorption is generalized for the N laser fields by introducing the sum over all laser fields. This term can be simplified further. Since the intensity in each applied laser field is identical and the detuning between these fields is much smaller than the transition frequencies of the dopants, i.e., $\delta \ll \omega_0$, the photon flux $\Phi_i = \Phi(x, y)$ is identical for all fields and depends only on the position of the emitter within the waveguide. In addition, the absorption cross-section for each laser field σ_i depends on the normalized detuning $\tilde{\Delta}_i$ of the laser field and the transition frequency of the emitter as follows:

$$\sigma_i\left(\tilde{\Delta}_i\right) = \frac{\sigma(\Delta = 0)}{1 + \tilde{\Delta}_i}, \quad \tilde{\Delta}_i = \frac{(\omega_i - \omega_0)^2}{\gamma_0^2}, \tag{2.8}$$

where $\sigma(\Delta = 0)$ is the absorption cross-section on resonance. The steady state solution

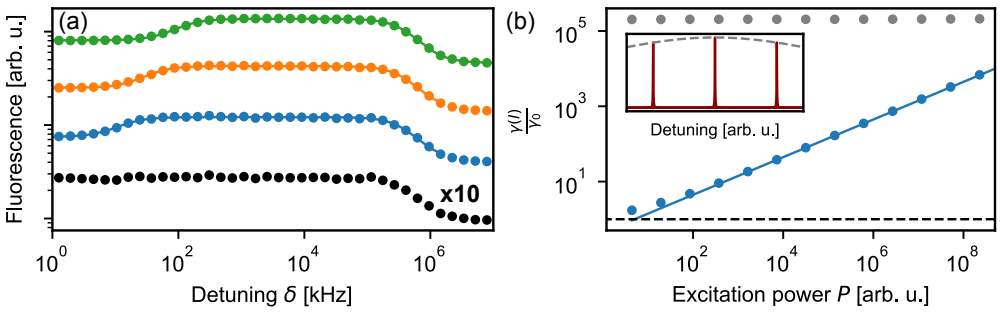

Figure 2.10.: **Transient spectral hole burning.** (Inset in b). Schematic depiction of three equidistant laser fields applied to measure the power-broadened homogeneous linewidth. (a) The calculated fluorescence (dots) depending on the detuning δ between the three laser fields for three different power setpoints (colors) shows two dips at small and large detunings, which are well-fit with double-Lorentzian functions (solid lines). From the fit to the dip at small detunings, the power-broadened homogeneous linewidth is extracted. (b) With decreasing excitation power, this power-broadened homogeneous linewidth (blue, dots) converges to homogeneous linewidth (black dashed). The data points are well-fit with a saturation law (blue, solid). For even smaller excitation powers, the dip at small detunings vanishes (black in panel a, calculated fluorescence scaled by a factor of 10). The linewidth of the second dip at large detunings corresponds to the inhomogeneous linewidth and is independent of the excitation power (gray dots).

$(t \to \infty)$ of Eq. 2.7 can then be expressed as a function of the ratio $\tilde{I}$ of the excitation intensity I to the saturation intensity I_S:

$$p_e\left(\tilde{I}\left(x,y\right),\omega_0\right) = \frac{1}{2}\frac{\tilde{I}\left(x,y\right)}{\tilde{I}\left(x,y\right)+\frac{1}{\sum_{i=1}^{N}\left(1+\tilde{\Delta}_i\right)^{-1}}} \leq 0.5,\ \ \tilde{I}\left(x,y\right) = \frac{I\left(x,y\right)}{I_S} = \frac{2\Phi\left(x,y\right)\sigma\left(\Delta=0\right)}{A}. \tag{2.9}$$

The expected fluorescence for the ensemble of emitters is then calculated by summing over all emitters:

$$S\left(\tilde{I}\right) \propto \sum_{E(x,y,\omega_0)} p_e\left(\tilde{I}\left(x,y\right),\omega_0\right)\beta\left(x,y\right), \tag{2.10}$$

with the β-factor (Subsec. 2.4.2) which depends on the position of the emitter within the cross-section of the waveguide. This model still contains two free parameters, the homogeneous linewidth and the saturation intensity. A quantitative prediction for the homogeneous linewidth could be made if the saturation intensity can be directly calculated from the dipole moment of the erbium transition.

As an example, the expected fluorescence is calculated for three laser fields $N = 3$

and three different excitation powers (Fig. 2.10, colors) as a function of the detuning δ between the laser fields. For each excitation power P, the values for the intensities $\tilde{I}(x, y)$ at the positions of the dopants are calculated according to the fundamental mode of the waveguide. Fig. 2.10 a shows that the fluorescence decreases with decreasing excitation power. For each power setpoint, the fluorescence exhibits two dips as a function of the detuning. The first dip is found at large detunings and is explained by the finite inhomogeneous broadening, i.e., the signal is reduced once the detuning of the sidebands approaches γ_{inhom}. The width of this dip is not affected by decreasing the excitation power (Fig. 2.10 b). The width of the second dip at small detunings is proportional to the power-broadened homogeneous linewidth. Since the laser fields have the same intensity, the power-broadened homogeneous linewidth is given by half of the dip width. The dip depth is approximately $\sqrt{N} = \sqrt{3}$, as expected from comparing Eq. 2.5 and Eq. 2.6. The fluorescence is fit with a model consisting of two Lorentzians centered at $\delta = 0$ to account for both dips. Fig. 2.10 b shows the homogeneous linewidth extracted from such fits to the fluorescence as a function of the excitation power. The homogeneous linewidths are fit with a saturation model:

$$\gamma_{\mathrm{hom}} \propto \gamma_0 \sqrt{1 + P} \tag{2.11}$$

The model fits the data very well (Fig. 2.10 b). Importantly, the slope of this fit function is not a free parameter, but given by the square-root dependence. For small excitation intensities, the power-broadened homogeneous linewidth converges to the homogeneous linewidth γ_0 and the dip depth at small detunings decreases. For even smaller excitation powers, no dip is visible any more (Fig. 2.10 a, black). Therefore, we conclude that this measurement scheme allows measuring an upper bound for the homogeneous linewidth which corresponds to a lower bound for the optical coherence time. The advantage of this measurement scheme is that only weak excitation pulses are required.

2.9.2. Optical coherence

Experimentally, three equidistant laser fields are efficiently generated from a single laser by an electro-optic phase modulator (EOM) in the excitation path (App. B). The detuning between the laser fields is then given by the EOM modulation frequency. The RF driving power of the EOM is adjusted so that the carrier and the two first-order sidebands have approximately equal power. In this configuration, the higher order sidebands are still strongly suppressed and can be neglected. The ensemble is then excited with 150 µs long pulses. To avoid persistent spectral holeburning (Subsec. 2.9.4), the carrier frequency is shifted in between two subsequent excitation pulses within the inhomogeneous line. The fluorescence is then recorded after each excitation pulse. Figure 2.11 a shows the fluorescence as a function of the applied EOM modulation frequency for different excitation powers (different colors) measured for site B on a CVD sample. The measured fluorescence is in good qualitative agreement with the prediction from the model (Fig. 2.10). Similar to the numerical results, the datasets for the different excitation powers are fit with the model including two Lorentzian terms, for the power-

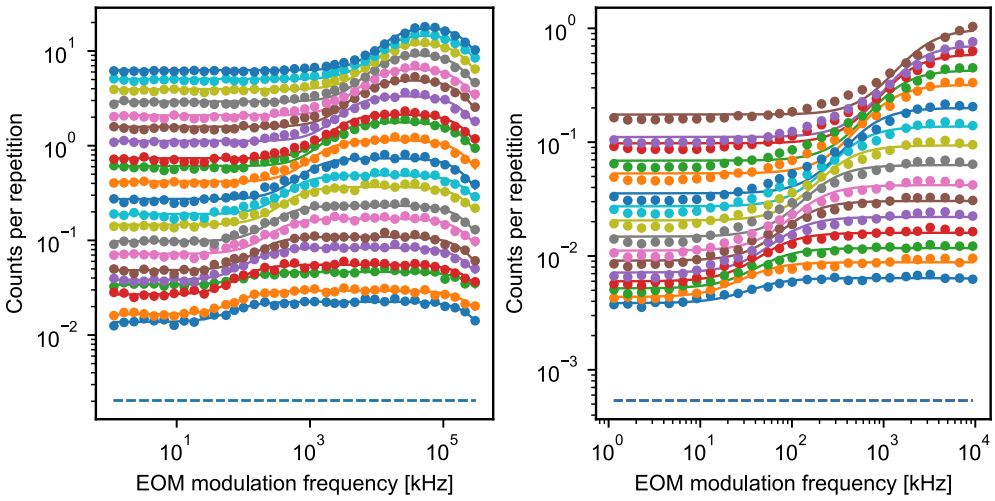

Figure 2.11.: **Measuring the homogeneous linewidth.** N equidistant laser fields are generated with electro-optic phase modulators. The fluorescence is measured for different excitation powers (colors) as a function of the detuning between the laser fields. The datasets are in good qualitative agreement with the numerical model (Fig. 2.10). The dips at small modulation frequencies correspond to the power-broadened homogeneous linewidths which are well-fit with a Lorentzian decrease with excitation power. (a) For $N = 3$, the fit function contains a second Lorentzian term describing the reduction of fluorescence at large modulation frequencies due to the inhomogeneous linewidth. (b) For $N = 27$, the contrast of the power-broadened homogeneous linewidths is enhanced facilitating measurements at even lower excitation powers than for $N = 3$.

broadened homogeneous linewidth and for the inhomogeneous broadening, respectively. For small excitation powers, the fluorescence signal approaches the dark count level of the detector preventing further measurements at lower powers. To overcome this, the number of equidistant laser fields is increased from three to 27. For this purpose, three EOMs are concatenated in the excitation path. For the same power per laser field, the same power-broadened homogeneous linewidths are measured, but the signal-to-noise ratio is significantly improved (Fig. 2.11 b) allowing us to continue the measurement at lower powers.

In the experiment, a deviation of the dip depth is observed from the expected values of $\sqrt{3}$ and $\sqrt{27}$ for three and 27 laser fields, respectively. This deviation could be caused by unequal powers of laser fields generated by the EOMs, by fluorescence induced by second-order sidebands, and by a contribution originating from broadband background. The dip decreases when the power-broadened homogeneous linewidth approaches the homogeneous linewidth at small powers due to the finite spectral densities of the emitters,

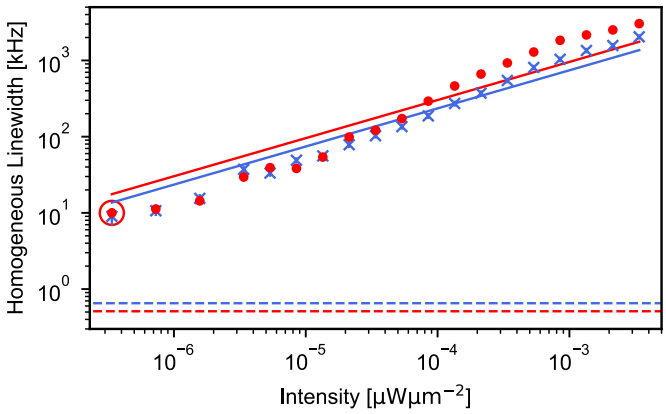

Figure 2.12.: **Homogeneous linewidth.** Power-broadened homogeneous linewidth as function of the excitation power using 27 equidistant laser fields for sites A and B measured on a CVD sample. The data points are well-fit with a saturation law. The narrowest power-broadened homogeneous linewidths, 9(3) kHz for site A (blue crosses) and 10(2) kHz for site B (red dots), set an upper bound for the homogeneous linewidth of the emitters which is approximately 20 times larger than the lifetime-limited linewidth. For site B, these data points are extracted from the measurements shown in Fig. 2.11 b.

which is also observed in the numerical model. In addition, for small powers where the signal-to-noise ratio decreases, the detector dark counts can also lead to a deviation of the dip depth.

Figure 2.12 shows the extracted homogeneous linewidths from measurements on both sites with 27 laser fields as a function of the excitation intensity. Similar to the numerical model, the homogeneous linewidths are well-fit with saturation laws. At the powers that give the smallest measurable signal, homogeneous linewidths of 9(3) kHz and 10(2) kHz are observed for site A and site B, respectively. These values correspond to an upper bound for the homogeneous linewidth. They are only a factor of ~ 20 larger than the lifetime-limited linewidth in the CVD samples of ~ 0.6 kHz. Due to the modification of the LDOS, the lifetime in the CVD samples is longer than in the FZ samples, hence the lifetime-limited linewidth is slightly smaller (Sec. 2.8).

The narrow homogeneous linewidths measured for both sites are comparable to the narrowest spectral features observed in nanostructured devices (Zhong and Goldner 2019). Based on the homogeneous linewidths, lower bounds for the optical coherence times of 17(6) µs for site A and 16(3) µs for site B are expected which imply exceptional coherence properties of the erbium dopants. Comparable homogeneous linewidths are also observed on the FZ and CZ samples (Gritsch et al. 2022).

Nevertheless, spectral diffusion of a few Megahertz at longer timescales is expected for

the erbium dopants similar to most other solid-state quantum emitter (Wolfowicz et al. 2021). This spectral diffusion is attributed to the nuclear spin bath and to the proximity to charge traps at the surfaces of the nanostructures and will be further discussed in Sec. 5.3.

2.9.3. Temperature dependence and spin-lattice relaxation processes

The optical coherence time T_2 cannot exceed the spin lifetime t_1. This is because the effective magnetic field at the position of the erbium dopants is always non-zero due to the Earth's magnetic field and the nuclear spin bath even without applying an external magnetic field. This effective magnetic field leads to a Zeeman splitting of the electronic spin states of the erbium dopants. Due to the Zeeman interaction, the different spin states have slightly different energies, and thus a spin flip always induces instantaneous spectral diffusion annihilating the optical coherence.

For small dopant concentrations, the electron spin lifetimes of rare-earth dopants in solids are usually limited by spin-lattice relaxation processes (Liu and Jacquier 2005). Three spin-lattice relaxation processes are known to occur for rare-earth dopants: one-phonon direct relaxation, and the Raman and the Orbach processes which are two-phonon processes (Wolfowicz et al. 2021). At cryogenic temperatures and in the absence of an external magnetic field, the direct process can be neglected. The Orbach process (Orbach and Bleaney 1997) involves the absoprtion of a phonon resonant with another energy level which, in case of erbium dopants, is usually a neighboring crystal field level. From this energy level, the electron then decays again while emitting a phonon. In contrast, the Raman process describes a process in which no resonant energy level is present, and thus only virtual phonons are exchanged. The transition rates of all three processes are intrinsically strongly dependent on the sample temperature since they scale with the phonon population in the crystal.

To investigate this experimentally, the sample temperature is tuned from base temperature to 18 K. The homogeneous linewidth of site A is measured for four different power setpoints (Fig. 2.13, different symbols). For all power setpoints, the homogeneous linewidth remains constant up to temperatures of ~ 8 K. Above ~ 8 K, the homogeneous linewidth increases with temperature. We find, that this temperature dependence is well-fit with an Orbach model:

$$\Gamma_{\mathrm{orb}}(T) = \frac{A_{\mathrm{orb}}}{2\pi} \sum_{\Delta_i \text{ in } \Delta_{ES},\Delta_{GS}} \frac{\Delta_i^3}{\exp\left(\frac{\Delta_i}{T}\right) - 1} + \Gamma_{\mathrm{offset}}. \tag{2.12}$$

The model sums over all crystal field levels in the ground and excited states (Δ_{ES}, Δ_{GS}) and assumes that the Orbach coefficient A_{orb} is identical for all crystal field levels. Furthermore, Γ_{offset} is added to account for the offset of the homogeneous linewidth due to power broadening. Since the crystal field splittings are measured independently, this model has only two free fit parameters, i.e., A_{orb} and Γ_{offset}. From the fits to the data, Orbach coefficients of $1.1(4) \times 10^3\,\mathrm{s^{-1}\,K^{-3}}$ and $0.9(4) \times 10^3\,\mathrm{s^{-1}\,K^{-3}}$ are extracted for site A and site B, respectively. These values are approximately 60-fold smaller than the

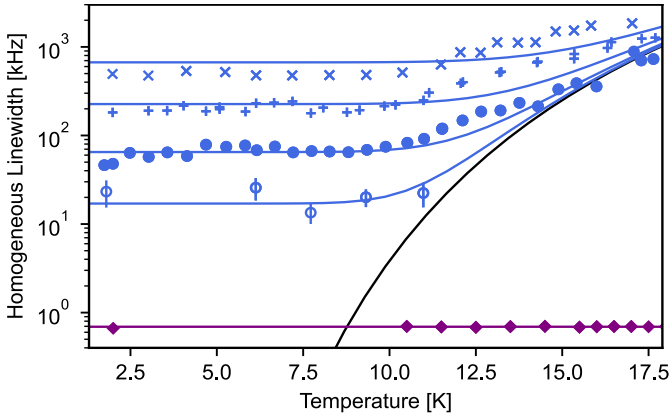

Figure 2.13.: **Temperature dependence of homogeneous linewidth.** We measure the homogeneous linewidth for four different power setpoints (different symbols) as a function of the temperature for site A on a CVD sample. The temperature is controlled by a resistive heater connected to the VTI. Simultaneously, the optical lifetime is measured so that the lifetime-limited homogeneous linewidth (purple) can be calculated. The lifetime-limited homogeneous linewidth does not increase within the shown temperature range. In contrast, the homogeneous linewidth starts to increase for temperatures larger than 10 K. From a Orbach fit to the data, we can extrapolate that lifetime-limited linewidths may be obtained below a temperature of 8 K (black).

Orbach coefficient found for erbium dopants in Y_2SiO_5 (Dibos et al. 2018) implying a favorable scaling with temperature.

In addition, the optical lifetime is measured for the different temperatures to ensure that the increase of the homogeneous linewidth is not caused by an increasing lifetime-limited linewidth. As expected for a predominately radiative decay (Sec. 2.8), the optical lifetime and the corresponding lifetime-limited linewidth remain constant (Fig. 2.13, purple diamonds). A similar dependence of the homogeneous linewidth on the temperature is observed for site B (Gritsch et al. 2022).

This result is of significant technological importance. In particular, the lifetime of the electron spin of erbium dopants in silicon does not limit the optical coherence at temperatures which are accessible with ^{4}He pulse-tube cryostats. These cryostats reach base temperatures between 1 K to 4 K. Such cryostats are much cheaper than the dilution refrigerators needed to achieve temperatures below 1 K.

2.9.4. Persistent spectral holes

In the previous homogeneous linewidth measurements, the frequencies of the applied laser fields are always shifted by a random global offset between two successive exci-

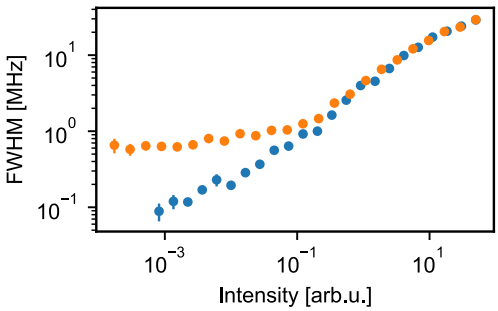

Figure 2.14.: **Persistent spectral holes.** The linewidths measured with the transient holeburning scheme show a saturation at small powers (orange) attributed to persistent spectral holeburning. The persistent spectral holes are explained by the polarization of the electron spin states which are non-degenerate due to the finite magnetic field at the position of the dopants even without an externally applied magnetic field. To overcome this effect, a random global frequency offset is added to the laser fields in between two subsequent excitation pulses. This allows measuring power-broadened homogeneous linewidths not limited by persistent spectral hole burning (blue).

tation pulses. In the following, this measurement technique is further motivated. In the previous Subsec. 2.9.3, we found that the effective magnetic field at the position of the erbium dopants is always finite and that below temperatures of about 8 K, the electronic spin lifetimes are expected to exceed the optical lifetimes. This implies that, when the ensemble is probed at a single frequency, the population in the electronic spin states can be transferred to the ground state which is not resonant with the excitation light. This results in persistent spectral holeburning (Fig. 2.14, orange). In this case, the homogeneous linewidth measurement probes the width of these persistent holes once the width of the power-broadened homogeneous linewidth becomes smaller than these persistent holes. The measured linewidths then converge to the width of the persistent holes for small powers.

To avoid probing the persistent spectral hole width, the excitation frequency of the laser fields is randomly shifted within 20 MHz in between two successive excitation pulses. Then, the measured linewidth does no longer saturate at small excitation powers (Fig. 2.14, blue). Instead, the measured linewidth again follows a square-root dependence as expected for the power-broadened homogeneous linewidth.

2.9.5. Integration yield

The homogeneous linewidth measurements can be used to estimate the integration yield at sites A and B. The integration yield is the fraction of implanted ions which is integrated on the respective sites after implantation and annealing.

For each site, the fluorescence signal is recorded at the center of the inhomogeneous broadening. For the same pulse parameters, the power-broadened homogeneous linewidth is then measured. With the detection efficiency of photons in the nanophotonic waveguides, the number of dopants contributing to the fluorescence signal can be deduced. By comparing the inhomogeneous and the homogeneous linewidths, this number of dopants can be related to the total number of dopants at the respective integration site. This number is then compared to the implanted dose. For the nanophotonic waveguides, an approximate yield between 0.05 % to 1 % for sites A and B is extracted.

This measurement technique allows us to obtain an order of magnitude lower bound for the integration yield. In particular, it omits all types of photon losses in the nanophotonic waveguides. These include propagation loss and mirror imperfections as well as finite β-factors (Subsec. 2.4.2).

In future samples, the integration yield may be more accurately determined from absorption measurements. In the samples used in this work, the low dopant concentration combined with oscillating reflection signals from the fiber-to-chip interfaces hindered absorption measurements. In addition to increasing the optical depth, either by increasing the dopant density or by using longer waveguides, absorption measurements can also benefit from a geometry without mirror. This allows obtaining a pure transmission measurement that avoids the effect of photon backscattering at the fiber-to-chip interface.

2.9.6. Alternative transient holeburning measurement scheme

The measurement scheme introduced in Subsec. 2.9.1 is compared to a second transient hole burning scheme which was first reported in (Berkman et al. 2023a) after our initial results were published (Weiss et al. 2021). For the experimental implementation of this scheme, only one laser field with a single frequency is required. The dopants are excited with a burn pulse and a probe pulse with same length and power, which are applied without any temporal delay in between. The fluorescence is then measured as a function of the frequency detuning between the burn and the probe pulse. Again, we can get an intuition by comparing two regimes. In the first regime, the shift between the two pulses is much smaller than the power-broadened homogeneous linewidth. Then, the probe pulse continues to excite the same dopants as the burn pulse. In the second regime, the detuning between the burn and probe pulse is much larger than the power-broadened homogeneous linewidth of the dopants. In this case, the laser field addresses a different set of dopants, which have not yet been excited, after shifting the excitation frequency. This scheme exploits that the excitation dynamics, i.e., the solution of Eq. 2.7, follow an exponential behavior. Because of this behavior, the increase of the excited state probability is largest at the beginning of the excitation process. Therefore, a larger fluorescence is expected in the second case (Berkman et al. 2023a).

Experimentally, the frequency shift of the laser field is applied by using an acousto-optic modulator (AOM). In Figure 2.15, both techniques are compared. For the transient holeburning scheme described in this section (dark blue), two pulses with lengths of 12.5 µs are applied. For the comparison with the other scheme, an EOM is additionally used to apply these pulses at three different frequencies with a separation of 80 MHz.

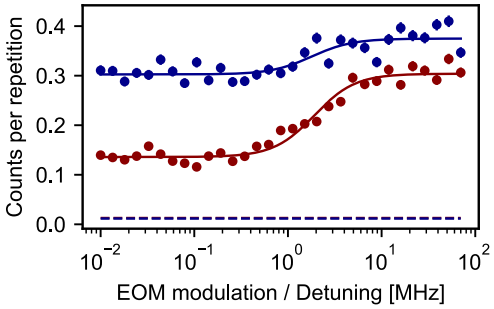

Figure 2.15.: **Different transient hole burning schemes.** The transient holeburning scheme used in this work (dark red) is compared to the transient holeburning scheme introduced in (Berkman et al. 2023a). Lorentzian fits (solid lines) to the measurements show that with both schemes, the same power-broadened homogeneous linewidth is measured. The scheme used is this work provide a better dip contrast improving the SNR.

For the transient hole burning scheme described in Subsec. 2.9.1 (dark red) pulses with the same power and with lengths of 25 µs, and three laser fields are applied. For both measurement schemes, dips corresponding to the power-broadened homogeneous linewidth are observed at low modulations frequencies which are well-fit with Lorentzians. From these fits, linewidths of 3.8(1) MHz and 3.8(4) MHz are extracted for the scheme used in this work and for the scheme introduced by (Berkman et al. 2023a), respectively. The power-broadened homogeneous linewidths are identical within the uncertainty, but the scheme used in this work provides a better signal-to noise-ratio.

2.10. Electronic spin states

Having focused on the optical properties of the erbium dopants in the previous sections, we now turn to their spin. Erbium dopants integrated at sites that completely lift the degeneracy of their *4f* orbitals form effective spin 1/2 systems (Sec. 1.2, Fig. 1.1 c, d). Furthermore, the *g*-tensor of the erbium dopants is generally anisotropic and different for the ground g_g and excited g_e state (Maryasov and Bowman 2012).

Thus, when a magnetic field is applied to an ensemble of erbium dopants, several magnetic classes can be observed. The magnetic classes emerge because the same erbium integration site can be found at multiple positions within the unit cell of the host crystal with different orientations with respect to the magnetic field axis. In addition, for each of these classes, two spin-preserving transitions with a splitting of $\Delta_{sp} \propto |g_g - g_e| B$ and two spin-flip transitions with a splitting of $\Delta_{sf} \propto |g_g + g_e| B$ can be spectrally resolved.

To investigate this for erbium dopants in silicon, a magnetic field is applied along the [100] crystallographic axis of an AMF sample implanted at room temperature and annealed to 500 °C (Sec. 2.3, Tab. 2.2). This sample is doped only with ^{170}Er which has

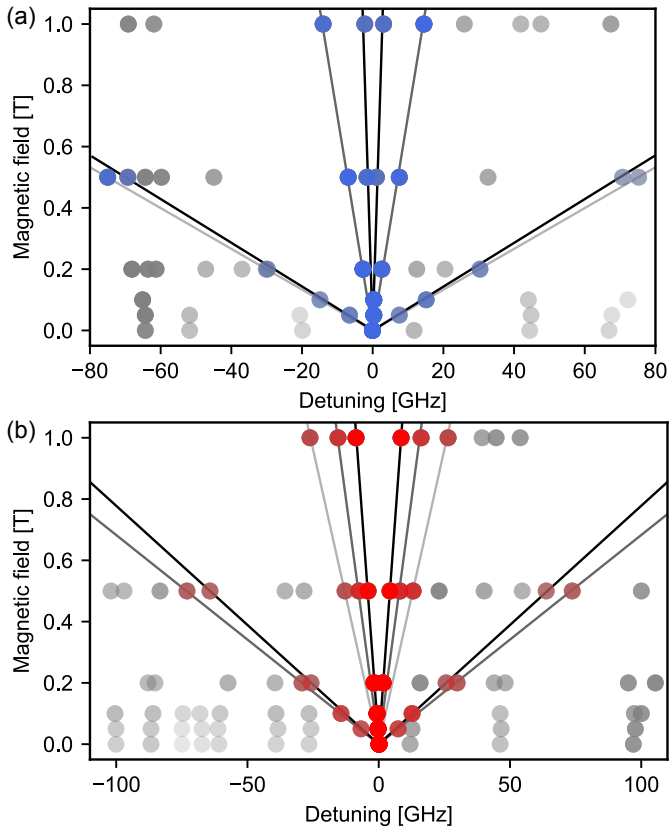

Figure 2.16.: **Magnetic field dependence.** For several different magnetic field amplitudes applied along (100), the peak positions (dots) in the fluorescence spectra are extracted. Peaks that occur symmetrically around the center frequency at zero field of site A (a) and site B (b) belong to the respective sites and are colored while the gray peaks belong to other sites. The saturation of the dots indicates the amplitude of the respective peak. Two magnetic classes are observed for site A and three magnetic classes for site B. From linear fits to the colored peaks, the differences (spin-preserving) and sums (spin-flip) of the g-factors g_g and g_e are calculated (Tab. 2.5).

no nuclear spin. In the cryostat, the sample temperature is kept at a temperature of 14 K so that the spin lifetime is short compared to the optical lifetime and persistent population transfer to the other spin state is avoided (Subsecs. 2.9.3 and 2.9.4).

Fluorescence spectra with ranges of 200 GHz around the center frequencies of the two sites A and B are then recorded for several magnetic field strengths ranging from 0 T to 1 T. In these spectra, several peaks are observed. In Figure 2.16, the center frequencies of these peaks (dots), extracted from Lorentzian fits, are shown as a function

Site	Spin-flip: $\lvert g_g + g_e \rvert$	Spin-preserving $\lvert g_g - g_e \rvert$
A	21.48(6)	0.39(5)
A	20.26(20)	2.04(5)
B	18.37(12)	1.22(1)
B	20.94(13)	2.23(7)
B	-	3.72(16)

Table 2.5.: **Sums and differences of effective g-factors along (100).** Sums and differences of the effective g-factors extracted for the magnetic classes of sites A and B found in Figure 2.16. The energy splitting in the optical ground state exceeds the energy splitting in the excited state, but the spin-preserving lines can not yet be assigned to the spin-flip lines to determine g_g and g_e.

of the applied magnetic field. The brightness of the peaks is hereby proportional to the saturation of the colors. For both sites, pairs of peaks that occur symmetrically around the center frequency at zero field are assigned to the respective site (colored blue and red). The effective sums and differences of the g-factors in the ground and the excited state are then extracted from linear fits to these peak positions. At least two magnetic classes for site A and at least three magnetic classes for site B are observed (Tab. 2.5).

By repeating the measurement at a large magnetic field of several Tesla and a temperature of 2 K, where the electron spin starts to freeze out, we find that the high energy branch is more populated indicating that the splitting in the ground state is larger than in the excited state. Nevertheless, the spin-preserving and spin-flip transitions cannot be unambiguously assigned to each other. This prevents the calculation of g_g and g_e for each class. Basically, single dopants can be studied to assign the spin-preserving to the spin-flip transitions since each of them can only belong to one magnetic class. This will be discussed later in this work (Subsec. 5.3.4). However, an intrinsic disadvantage of this technique is that single dopants may exhibit deviations from the ensemble g-tensors due to lattice defects in their local environment.

In future experiments with ensembles of dopants, the spin-preserving and spin-flip lines can be related by spectral holeburning. For such measurements, a pump laser field is used to polarize the spin population in the optical ground state. A weaker probe field is then applied to measure the spin population on the other transitions. Intrinsically, a population transfer is only observed between the transitions belonging to the same magnetic class.

In addition, samples exclusively doped with ^{167}Er will be studied in the future. The ^{167}Er isotope has a nuclear spin of 7/2. At potential zero-first-order-Zeeman (ZEFOZ) points at small magnetic fields or at very large magnetic fields, which freeze out the electron spin, the nuclear spin states of ^{167}Er can exhibit exceptional coherence times (Ortu et al. 2018; Rančić et al. 2018).

2.11. Summary and outlook

In summary, we have found that erbium dopants integrate into silicon at two novel sites, i.e., site A and site B, which have promising properties for quantum technologies. Site A and site B are reproducibly formed by ion implantation and annealing under novel conditions. These sites are also observed in commercially available nanophotonic structures fabricated on wafer scale, demonstrating the scaling potential of this material platform. Compared to erbium dopants in other host materials (Tab. 2.6), the novel erbium sites in silicon show inhomogeneous broadenings that are only a factor of two larger than the narrowest broadenings reported in the literature. Moreover, these sites exhibit radiative decays that are more than an order of magnitude faster than in any other host material and narrow homogeneous linewidths indicating excellent optical coherence. Due to the large Debye temperature in silicon and the crystal field splittings which are larger than in any other host, the narrow homogeneous linewidths are preserved up to temperatures of 8 K. These results make silicon a highly promising host material for erbium dopants.

In future experiments, the microscopic composition of the two novel sites will be further investigated, which may help to optimize the integration yield. For this purpose, an applied magnetic field will be rotated relative to the sample along at least three axes. From such measurements, the symmetry of the sites can be determined. Moreover, the position of the erbium dopants within the unit cell of the silicon host crystal may be inferred in combination with the crystal field measurements.

A challenge for this material system is to increase the fluorescence in the nanophotonic waveguides. One way to do this is to increase the length of the waveguides if the waveguide propagation loss is small enough. To this end, the origin of the slightly increased propagation loss observed for waveguides fabricated after erbium implantation will be further studied. In addition, the integration yield at sites A and B could be improved. This will require further optimization of the implantation and annealing conditions. This optimization should also focus on reducing the background contribution which will increase the signal-to-noise ratio.

With an increased fluorescence, the spin dynamics in the ensemble of erbium dopants could be probed with spectral holeburning techniques. If sufficiently narrow spectral features can be prepared, the erbium dopants could be used to realize chip-based quantum memories, e.g., with the atomic frequency comb protocol (Afzelius et al. 2009). Due to the narrow homogeneous linewidths, microsecond long optical coherence, and thus similar storage times, can be expected for such a quantum memory. The storage times might be further enhanced by using the nuclear spin states of ^{167}Er isotope at zero or very large magnetic fields. Then, the coherence time is likely limited by the spin bath induced by natural abundance of the ^{29}Si isotope which can be eliminated by isotopic purification (Liu et al. 2022). This may result in potentially second (Rančić et al. 2018) or even-hour long coherence times (Saeedi et al. 2013).

Another possible application, which will be pursued in the next chapters, is the realization of a spin-photon interface with a single erbium dopant in silicon coupled to an optical cavity.

	Si (site A)	Si (site B)	Y_2SiO_5 (S1)	Y_2SiO_5 (S2)
Wavelength [nm]	1537.76	1536.06	1536.48	1538.90
Optical Lifetime [ms]	0.142	0.186	11.4	9.2
Branching ratio	0.23(5)	0.23(5)	0.2	-
Min inhom. LW [GHz]	0.45(2)	0.50(2)	0.2	0.2
homogeneous LW [kHz]	<10	<10	0.07	0.7
Lifetime limited LW [kHz]	1.121	0.856	0.014	0.017
CF splitting Z_2 [THz]	2.634(3)	2.187(3)	1.9	1.4
CF splitting Z_2 [cm^{-1}]	87.9(1)	73.0(1)	63.4	46.7
CF splitting Y_2 [THz]	2.418(3)	1.766(3)	1.2	1.2
CF splitting Y_2 [cm^{-1}]	80.7(1)	58.9(1)	40.0	40.0
Debye temperature[K]	640	640	580	580

	$CaWO_4$	$Y_3Al_5O_{12}$	$LiNbO_3$	TiO_2	YVO_4	Y_2O_3
Wavelength [nm]	1532.2	1527	1531.52	1520	1529.2	1535.69
Optical Lifetime [ms]	2.8	6.9	2	5.3	3.3	8.5
Branching ratio	-	-	-	-	0.42	0.22
Min inhom. LW [GHz]	1	30	250	0.45	0.2	0.4
homogeneous LW [kHz]	2	5	3	-	1	0.6
Lifetime limited LW [kHz]	0.057	0.023	0.080	0.03	0.048	0.022
CF splitting Z_2 [THz]	0.6	0.66	1.9	1.06	1.1	1.2
CF splitting Z_2 [cm^{-1}]	20.0	22.0	63.4	35.4	36.7	40
CF splitting Y_2 [THz]	0.25	1.5	1.9	0.46	0.055	1
CF splitting Y_2 [cm^{-1}]	8.3	50	63.4	15.3	1.8	33.4
Debye temperature [K]	267	405	503	740	443	230

Table 2.6.: **Comparison of erbium dopants in different host materials.** References: Si (site A) and Si (site B): (Gritsch et al. 2022), Y_2SiO_5 (S1) and Y_2SiO_5 (S2): (Thiel, Böttger, and Cone 2011), Y_2O_3: (Thiel, Böttger, and Cone 2011; Fukumori et al. 2020), $CaWO_4$: (Thiel, Böttger, and Cone 2011; Ourari et al. 2023), $Y_3Al_5O_{12}$: (Thiel, Böttger, and Cone 2011), $LiNbO_3$: (Thiel, Böttger, and Cone 2011), TiO_2: (Phenicie et al. 2019), YVO_4: (Li et al. 2020; Xie et al. 2021).

3. Spin-photon interfaces with single emitters in optical cavities

Spin-photon interfaces enable quantum logic operations, e.g., quantum gates between spin qubits and photonic qubits. In quantum networks, such interfaces are required at each network node so that entangled states between flying qubits encoded in optical photons and stationary qubits encoded in spin states can be created. These photonic qubits are used in turn to create entanglement between spin qubits located at remote nodes. To facilitate this, the spin-photon gates require an optical nonlinearity which is inherently provided by single emitters. Furthermore, these gates should be fast, and implemented with high success probability, enabling large quantum information processing rates, which requires a strong, ideally deterministic spin-photon interaction (Borregaard, Sørensen, and Lodahl 2019). Single emitters in free-space or bulk materials do not fulfill this requirement because they have only a small absorption cross-section compared to a diffraction-limited laser spot. To overcome this, single emitters can be embedded in optical resonators (Reiserer and Rempe 2015). Optical resonators can confine light fields in time and space at the location of the emitter such that even deterministic interactions can be achieved. Single emitters in optical cavities then become pristine candidates for quantum networking (Reiserer 2022) and quantum computation (Simmons 2023).

In this chapter, important aspects that allow the modeling of single erbium dopants embedded in an optical cavity are reviewed (Sec. 3.1). Then, it is discuss how such a device can be used to create entanglement between a spin and a photon, and between two spins (Sec. 3.2). Finally, different cavity realizations suitable for single erbium dopants in silicon are compared (Sec. 3.3).

3.1. Single emitters in optical cavities

An emitter embedded in an optical resonator experiences a strong modification of the local photonic density of states. Thus, the light-matter interaction inside the resonator can be fundamentally different compared to the situation in free-space. To describe this, the cooperativity (Subsec. 3.1.1), the central figure of merit to describe the coherent interaction between a cavity mode and an emitter, and the Purcell enhancement (Subsec. 3.1.2), the lifetime reduction of the optically excited state, are introduced. In addition, the reflection coefficient of a resonator and the probability to couple photons out of the emitter-cavity system are outlined (Subsec. 3.1.3).

3.1.1. Cooperativity

The interaction between a single emitter and a cavity mode is defined by three parameters (Fig. 3.1). These are the emitter-photon coupling parameter g, the photon decay rate of the cavity mode κ, and the total dephasing rate of the emitter γ (Fox 2006; Janitz, Bhaskar, and Childress 2020). Note that here κ and γ are intensity decay rates. In the literature, they are sometimes used to express the electric field decay rates which leads to factors of 2 in all equations (Reiserer 2022).

The emitter-photon coupling rate, which is generally defined by the electric field amplitude $\vec{E}$ at the position of the emitter and the electric-dipole vector $\vec{\mu}_{eg}$, is given in a resonator as (Fox 2006):

$$g = \frac{\vec{\mu}_{eg}\vec{E}}{\hbar} = \left(\frac{\mu_{eg}^2 \omega}{2\varepsilon_0 \hbar V}\right)^{\frac{1}{2}}, \tag{3.1}$$

with the vacuum permittivity ε_0, the Planck constant $\hbar$, and the angular frequency ω of the resonant transition. In addition, optimal alignment between the dipole and the electric field is assumed in this equation. The mode volume V is a property of the cavity that measures the spatial confinement of the resonant light fields and is defined as (Reiserer and Rempe 2015):

$$V = \frac{\int \epsilon \left|\vec{E}\right|^2 d^3r}{\max\left(\epsilon \left|\vec{E}\right|^2\right)}, \tag{3.2}$$

where ϵ is the permittivity within the cavity volume. A stronger spatial photon confinement leads to a smaller modal volume and thus to a larger emitter-photon coupling rate.

The photon decay rate is given by the sum of all photon scattering rates out of the cavity (Fig. 3.4) and thus corresponds to the temporal confinement of the photons in the cavity mode (Reiserer and Rempe 2015):

$$\kappa = \kappa_{out} + \kappa_{loss} = \Delta\omega \tag{3.3}$$

Albeit the dynamics in the cavity is not affected by in which of the channels the photons are lost, it is of practical importance to distinguish between the outcoupling channel κ_{out} where the photons are collected and measured and all other channels where the photons are lost and thus undetectable κ_{loss}. In addition, κ is proportional to the linewidth in frequency domain of the resonator mode $\Delta f = \frac{\Delta\omega}{2\pi}$, which can be measured by sweeping the frequency of a laser over the cavity resonance. To compare cavities with different resonant frequencies, the dimensionless quality factor (Q-factor) is introduced (Janitz, Bhaskar, and Childress 2020):

$$Q = \frac{\omega}{\Delta\omega} = \frac{\omega}{\kappa} = \frac{f}{\Delta f}. \tag{3.4}$$

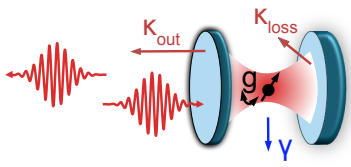

Figure 3.1.: **Single emitter in an optical cavity.** The dynamics of an emitter (black dot) coupled to a cavity mode (red) is defined by three parameters: the emitter-photon coupling g, the photon decay rate of the cavity mode κ, and the total dephasing rate γ. The photon decay rate consists of two components corresponding to the light scattered out of the cavity in the direction where it is collected (κ_{out}) and the light scattered into other modes (κ_{loss}). The emitter-cavity system is controlled and probed by light fields with single or few photons (curly arrows) impinging on one of the two cavity mirrors.

The total dephasing rate of the emitter is given by the homogeneous linewidth of the emitter. It results from multiple effects: the optical decay through the cavity-coupled transition γ_0, radiative or non-radiative decay through non-coupled transitions γ_1, and the pure dephasing rate of the emitter γ_d:

$$\gamma = \gamma_0 + \gamma_1 + \gamma_d \tag{3.5}$$

These three parameters are combined into a single quantity, the cooperativity C, which expresses the probability of coherent emitter–photon interaction (Janitz, Bhaskar, and Childress 2020; Borregaard, Sørensen, and Lodahl 2019):

$$C = \frac{4g^2}{\kappa\gamma}. \tag{3.6}$$

In particular, for $C > 1$, the emitter-photon interaction inside a resonator can become deterministic (Reiserer and Rempe 2015). Furthermore, two different regimes are distinguished for the light-matter interaction in the resonator. In the strong coupling regime $g > \max(\kappa, \gamma)$, the light-matter interaction is reversible. In this case, $C > 1$ is trivially satisfied such that the interaction is always deterministic. The dynamics of the system is then described by the Jaynes-Cummings Hamiltonian. In contrast, in the weak coupling regime, also called the fast cavity or Purcell regime $g < \max(\kappa, \gamma)$, the light-matter interaction is not reversible. Importantly, also in this regime, for $C > 1$, which can be realized by $\kappa > g \gg \gamma$, the light-matter interaction can be deterministic.

3.1.2. Purcell enhancement

Similar to Subsec. 2.4.2, the modification of the local density of states leads to a change in the lifetime of the emitter, i.e., the Purcell effect or Purcell enhancement. In particular,

in cavities with large Q-factors and small mode volumes, the transition rate of the emitter to the cavity-coupled light mode γ_c is drastically increased compared with the bulk transition rate γ_0. This can be accessed experimentally by measuring the optical lifetime of the emitter in the cavity T_1 and comparing it with the bulk lifetime $T_{1,\text{bulk}}$.

$$\gamma_c = P\gamma_0, \quad T_1 = \frac{T_{1,\text{bulk}}}{P}, \tag{3.7}$$

where P is the Purcell factor. P can be expressed as (Janitz, Bhaskar, and Childress 2020):

$$P = C\frac{\gamma}{\gamma_0} = \frac{4g^2}{\kappa\gamma_0} = \frac{3}{4\pi}\left(\frac{\lambda}{n}\right)^3\frac{Q}{V}, \quad \gamma_0 = \frac{\mu_{eg}^2\omega^3}{3\pi\varepsilon_0\hbar c^3} \tag{3.8}$$

where λ is the vacuum wavelength, and n is the refractive index. Typically, the mode volume is expressed in units of $(\lambda/n)^3$, which makes it easier to compare resonator designs for different wavelengths. In contrast to the cooperativity, the Purcell factor depends only on cavity parameters since g^2 and γ_0 are both proportional to the transition dipole matrix element μ_{eg} such that it cancels out in the equation for P (Reiserer 2022).

The Purcell factor in Eq. 3.8 represents the theoretically largest value for an ideal, optimally placed and orientated two-level emitter in a cavity. However, the Purcell factor of an emitter embedded in a cavity at position $\vec{r}$ can be reduced by the following effects:

First, the Purcell enhancement decreases if the emitter is not placed exactly at the position with the largest field intensity. In this case, the reduction of the Purcell factor is given by the ratio of the field intensity at the position emitter compared with the intensity maximum. This is particularly relevant for solid-state systems in which the position of the emitter cannot be changed, and its location typically stems from probabilistic integration techniques like ion implantation.

Second, misalignment of the electric field vector and the orientation of the induced dipole leads to a reduction proportional to the scalar product of the direction vectors of the dipole and the electric field. Again, for emitters in the solid-state, this term can be significant because the dipole orientation of the transition is determined by the host crystals which often cannot be orientated arbitrarily with respect to the cavity mode.

Third, the Purcell enhancement is also reduced in presence of other decay channels, e.g., nonradiative decay or transitions to other energy levels of the emitter. This applies to almost all emitters. In particular for erbium dopants, this term is given by the branching ratio $Y_1 \rightarrow Z_1$ (Dibos et al. 2018) (Sec. 2.6). For color centers, it is usually given by the Debye-Waller factor, i.e., the branching ratio into the zero-phonon line (Janitz, Bhaskar, and Childress 2020).

Fourth, the Purcell enhancement is also reduced if the transition frequency of the emitter and the resonance frequency of the cavity are detuned (Fox 2006). Including all of these effects, the Purcell factor can be then written as:

$$P(\vec{r},\omega) = \frac{3}{4\pi}\frac{Q}{V}\left(\frac{E(\vec{r})}{E_{max}}\right)^2\frac{\left|\vec{E}(\vec{r})\,\vec{\mu}_{eg}\right|}{\left|\vec{E}(\vec{r})\right|\left|\vec{\mu}_{eg}\right|}\frac{\gamma_0}{\gamma_0+\gamma_1}\frac{1}{4\left(\frac{\omega_c-\omega}{\Delta\omega}\right)^2+1}, \tag{3.9}$$

where ω_c is the resonance frequency of the cavity. Because of Eq. 3.8, the same correction terms also apply for the cooperativity.

Importantly for erbium dopants, the Purcell enhancement reduces the long excited state lifetimes $> 100\,\mu s$ which would significantly limit the repetition rate of many quantum information processing operations.

3.1.3. Cavity reflection spectrum and outcoupling efficiency

To probe the dynamics in the cavity, light fields are reflected off the cavity. The response is given by the reflection coefficient $r(\omega)$, which can be derived from input-output theory (Reiserer and Rempe 2015):

$$r(\omega) = 1 - \frac{2\kappa_{out}}{2i(\omega - \omega_c) + \kappa + \frac{4g^2}{2i(\omega-\omega_0)+\gamma}} \tag{3.10}$$

Remarkably, the reflection coefficient can be affected by the presence of a single emitter (Reiserer and Rempe 2015) for sufficiently low probe photon fluxes which do not saturate the cavity-coupled transition. The reflection spectrum of the cavity is further given as $R = |r(\omega)|^2$.

Furthermore, the modification of the local photonic density of states also affects the distribution of spatial and frequency modes in which the photons are emitted. In particular, the fraction of photons emitted into the cavity mode is given as:

$$\beta_c = \frac{P}{1+P}. \tag{3.11}$$

Thus, in resonators with large Purcell enhancement, almost all photons are emitted into the cavity mode. In addition, the fraction of photons which are coupled out of the cavity can be calculated from the ratio of the scattering rates κ_{out} and κ_{loss}. The outcoupling efficiency η, which describes the probability that an excitation of the two-level system creates an outcoupled photon, is then given as:

$$\eta = \frac{\kappa_{out}}{\kappa}\beta_c = \frac{\kappa_{out}}{\kappa_{loss}+\kappa_{out}}\frac{P}{1+P}. \tag{3.12}$$

Optimizing the outcoupling efficiency is critical for some applications of optical resonators, e.g., single-photon sources (Knall et al. 2022).

3.2. Generating entanglement

Protocols entangling spin qubits with optical photons and remote spin qubits were first demonstrated in pioneering experiments with the electronic spin of an NV center in diamond (Bernien et al. 2013; Hensen et al. 2015). Remarkably, these experiments could be realized without an optical cavity due to the large transition dipole moment of the NV center. In comparison, the transition dipole moment of erbium dopants in

silicon is about four orders of magnitude smaller such that even for proof-of-concepts experiments cavity integration seems mandatory.

In the following, we thus consider the general case of a single optically addressable spin qubit embedded in an optical cavity. This applies specifically for a spin qubit encoded in the Zeeman states of a single erbium dopant embedded in a cavity and generally for many other solid-state qubits (Wolfowicz et al. 2021). The cavity is further assumed to be on resonance with one of the two spin-preserving optical transitions, i.e., the bright state of the spin qubit ($|\uparrow\rangle$, Fig. 3.2). The other spin state $|\downarrow\rangle$ is assumed to be off-resonant with the excitation laser and thus "dark".

To enable two-qubit entangling gates between the spin and the photon and also between different spins, the following control operations must be available for the spin qubit (DiVincenzo 2000):

First, these control operations include the initialization of the spin qubit in the eigenstates of the Z-basis ($|\uparrow\rangle, |\downarrow\rangle$). This can be achieved by optical pumping on either the spin-flip or the spin-preserving transitions. Depending on the detuning of these transitions with respect to the resonance frequency of the cavity, the required fields might be applied in different polarization or spatial modes.

Second, coherent qubit rotations are required to prepare the spin in superposition states. These rotations can be realized by direct driving of the spin transition with radiation fields in the microwave (MW) domain or with all-optical Raman control using two-color laser fields. Moreover, these rotations can be applied for dynamical decoupling sequences to extend the coherence time of the spin qubit.

Third, one needs the ability to determine the state of the qubit after each experimental sequence, which can be implemented by fluorescence state detection. In this scheme, the bright spin-preserving transition is repeatedly probed, and the number of photons detected is used to discriminate between the dark and the bright state. This is possible if both the lifetime of the spin states exceeds the sequence length and the spin-flip probability from the optically excited state is sufficiently low. Embedding the spin qubit in an optical resonator can significantly improve the scheme either if the splitting between the spin-flip transitions and the probed transition is larger than the resonator linewidth or if the dipoles are oriented such that only the spin-preserving transition is enhanced. In both cases, the resonator increases the number of probe repetitions that can be applied before an unwanted spin-flip occurs such that this effect is called cavity-enhanced cyclicity (Raha et al. 2020).

In addition to these control operations, it is paramount that the emitted optical photons are coherent, i.e., indistinguishable in all degrees of freedom except the one degree of freedom which is used to encode the photonic qubit. This indistinguishability can be verified by Hong-Ou-Mandel interference of two subsequently emitted photons or, alternatively, by measuring the optical coherence time T_2 of the emitter with optical echo sequences. Ideally, the optical coherence time is lifetime-limited $T_2 = 2T_1$. For this purpose, cavities can be a key enabler in order to overcome emitter dephasing by sufficient reduction of the optical lifetime as long as the cavity itself does not introduce additional contributions to the dephasing (Reiserer 2022).

Once these requirements are fulfilled, the spin qubits can be used for interference-based

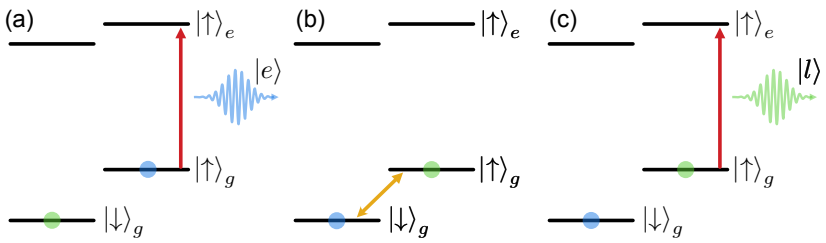

Figure 3.2.: **Time-bin entanglement.** The state of a qubit encoded in the optical ground state of a two-level spin system can be entangled with the emission time of an optical photon. For this purpose, the qubit is prepared in a superposition state (faint colored dots). (a) Then, an optical π-pulse resonant with one of the two spin-preserving transitions (red arrow) is applied. (b) Subsequently, the state of the qubit is rotated in the z-basis (orange). (c) Finally, another optical π-pulse is applied on the same transition as the first π-pulse.

quantum information protocols (Reiserer 2022). For this purpose, the spin qubits are first entangled with a photonic qubit. Photonic qubits can be defined in different degrees of freedom. Possible options are time of emission (Barrett and Kok 2005), polarization (Reiserer and Rempe 2015), or frequency (Moehring et al. 2007). Importantly, these photonic qubits are loss-tolerant in contrast to qubits encoded in the photon number states for which photon loss, which is unavoidable in any realistic implementation, leads to a rotation of the qubit.

In the following, we choose time-bin encoding, which has been successfully realized with optically addressable spin qubits in the solid-state (Fig. 3.2) (Bernien et al. 2013; Bhaskar et al. 2020). To generate an entangled state between the spin and the photon, the spin qubit is prepared in a superposition state (faint colored dots, Fig. 3.2). Then, an optical π-pulse (red arrow) is applied on the bright spin-preserving transition which is resonant with the cavity mode. The time interval after this π-pulse corresponds to the early time-bin $|e\rangle$ of the photonic qubit. Next, the population of the spin-qubit is swapped by a π-pulse on the qubit transition (orange arrow). Then, a second optical π-pulse is applied on the bright spin-preserving transition, and the subsequent time interval corresponds to the late time-bin $|l\rangle$. If the spin qubit is initially prepared in an equal superposition state, this protocol creates a maximally entangled state shared by the photon and the spin $|\Psi_{ps}\rangle$:

$$|\Psi_{ps}\rangle \propto |e\downarrow\rangle + |l\uparrow\rangle \tag{3.13}$$

The efficiency of this entanglement generation protocol can be greatly enhanced by embedding the spin qubit in a suitable cavity, but a cavity is not strictly required (Bernien et al. 2013). In contrast, for $C \geq 1$, a cavity-enabled dispersive phase gate can be realized, which was first demonstrated in pioneering experiments with trapped atoms

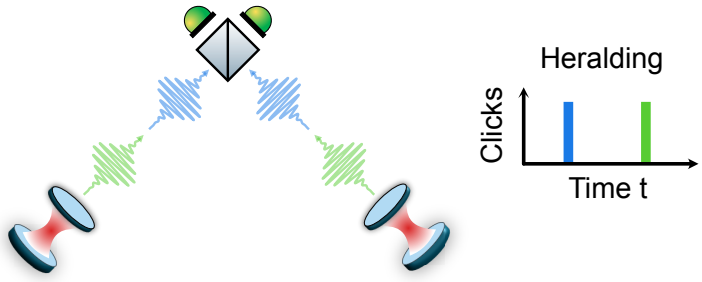

Figure 3.3.: **Remote entanglement.** To generate remote entanglement, the spins are at first entangled with photonic time-bin qubits. The emitted photons are interfered at a beamsplitter, to erase the which-path information. Exactly one click in both the early and the late time bin heralds successful generation of an entangled state shared by the two spins (Barrett and Kok 2005; Bernien et al. 2013).

(Reiserer et al. 2014; Tiecke et al. 2014) and could later be also implemented with SiV centers in diamond (Bhaskar et al. 2020; Stas et al. 2022). This gate relies on the effect that the reflection of a cavity can be changed by the presence of a single emitter (Eq. 3.10). For a sufficiently large cooperativity, this effects allows resolving the state of the spin qubit so that the spin-dependent reflection from the cavity can be used as a gate operation. Remarkably, this spin-photon gate avoids bringing the spin qubit to its optically excited state, which may reduce its decoherence.

After explaining these different ways to genereate spin-photon entanglement, it will be discussed how this can be used to establish an elementary quantum network link by generating remote entanglement between two spin qubits (Barrett and Kok 2005). This scheme has been successfully realized with NV centers in diamond (Bernien et al. 2013). To this end, two remote spin qubits are prepared in equal superposition states. Then, by applying the sequence described above, both spins are entangled with photonic time-bin qubits. The photonic qubits are then interfered at a beamsplitter to erase the which-path information (Fig. 3.3). If two clicks are detected in either the early or the late time bin, the spins are projected to a separable state. In contrast, if one photon is detected in each time-bin, the successful creation of a maximally entangled state $|\Psi\rangle$ shared by the two spin qubits is heralded.

$$|\Psi\rangle \propto |\downarrow\uparrow\rangle \pm |\uparrow\downarrow\rangle \tag{3.14}$$

Importantly, the spin qubits must not dephase during this sequence, thus the coherence time of the spin t_2 must exceed the sequence length including the traveling time of the photons to the measurement station.

3.3. Cavity designs for erbium dopants in silicon

Optical resonators suitable to resolve single erbium dopants in silicon can be divided into open microcavities and nanophotonic cavities. The most prominent example of open microcavities are Fabry-Perot cavities which are formed by two ultra-high reflectivity Bragg mirrors (Fig. 3.4 a). Such mirrors require surfaces with ultra-low scattering loss which can be fabricated by CO_2-laser ablation on glass substrates or on optical glass fibers and subsequent deposition of multiple dielectric layers (Hunger et al. 2012; Uphoff et al. 2015). To stabilize the resonant frequency of the cavity, the cavity length, i.e., the distance between the two mirrors, requires good passive stability and often also active stabilization. Passive stability is achieved by using appropriate dampers and soft springs to decouple the cavity from vibrations in the environment. This is particularly challenging in closed-cycle cryostats where helium pumps and compressors are connected to the sample space via a pulse tube cooler (Merkel, Ulanowski, and Reiserer 2020). In such settings, and generally for Fabry-Perot cavities with large Q-factors, additional active stabilization is implemented, e.g., with piezoelectric elements manipulating the distance between the mirrors and locking schemes such as the Pound-Drever-Hall technique (Merkel 2021; Black 2001).

With trapped atoms, ground-breaking experiments in the strong coupling regime ($C > 10$) were demonstrated in Fabry-Perot resonators (Reiserer and Rempe 2015). In addition, such cavities are compatible with all types of solid-state host materials, including silicon, which can be polished to sufficiently flat surfaces to avoid excessive scattering loss. The host material, usually thinned to a few micrometers (Merkel, Ulanowski, and Reiserer 2020) or in the form of nanocrystals (Casabone et al. 2021), is then placed in between the two mirrors. Erbium dopants in YSO membranes embedded in Fabry-Perot resonators demonstrated Purcell enhancements $P > 110$ (Ulanowski et al. 2023; Ulanowski, Merkel, and Reiserer 2022).

A special type of Fabry-Perot cavities are fiber cavities comprising at least one mirror fabricated on a facet of an optical fiber which can then be used for in- and outcoupling of light fields (Hunger et al. 2010). In contrast to conventional Fabry-Perot cavities, this eliminates the need for free-space optics to couple light in and out of the resonator and may also lead to a reduction in the device footprint. Erbium embedded in yttrium oxide (Y_2O_3) nanocrystals showed a Purcell enhancement $P > 120$ in such cavities (Deshmukh et al. 2023).

Alternatively, erbium dopants can be embedded in nanophotonic resonators. A key advantage of such cavities is that they are lithographically fabricated and thus can be integrated on photonic chips together with other photonic elements (Panuski et al. 2022), with only a fraction of the device footprint compared to open micro-cavities. Examples of such resonators are ring resonators (Fig. 3.4 b) or photonic crystal resonators (Fig. 3.4 c). The latter, specifically one-dimensional photonic crystal cavities, fabricated directly from erbium-doped silicon, are used for this work.

Photonic crystal cavities typically have mode volumes of about $1\,(\lambda/n)^3$ which is significantly smaller than the mode volumes of most ring resonators (Bogaerts et al. 2012) and Fabry-Perot cavities. Thus, the number of dopants within that volume which expe-

rience significant Purcell enhancement is reduced. The Q-factors achieved for photonic crystal cavities depend strongly on the material and the available nanofabrication methods. Large Q-factors have been observed in diamond, silicon nitride, and silicon carbide, but the largest Q-factors to date have been observed in silicon, enabled by the unique level of maturity of silicon nanofabrication (Asano et al. 2017).

The cooperativity and Purcell factors achieved in photonic crystal cavities exceed the values reported for all other cavities with record cooperativities $> 1 \times 10^2$ observed for a single SiV center in diamond (Bhaskar et al. 2020) and Purcell factors of about 1×10^3 observed for erbium dopants in $CaWO_4$ and MgO (Ourari et al. 2023; Horvath et al. 2023). Remarkably, the latter was achieved by a hybrid integration approach. To this end, nanophotonic silicon resonators are coupled evanescently to emitters in a different host material which is incompatible with nanofabrication (Dibos et al. 2018). In these devices, the maximum intensity of the electric and magnetic fields is still located in the silicon device such that even larger values of P can be expected if the dopants are directly integrated there.

Furthermore, nanophotonic resonators are monolithic, i.e., they are less susceptible to vibration-induced instabilities and do not require special passive or active stabilization. However, this entails also that the tuning of the resonance frequency after fabrication is limited (Sec. 4.5).

Finally, we note that, despite these promising properties of photonic crystal cavities, the intrinsic proximity of the erbium dopant to the surfaces be detrimental for the coherence of these emitters and induce additional spectral diffusion (Kuhlmann et al. 2013). This effect is avoided in micrometer-thin membranes in Fabry-Perot cavities such that measurements in such a setting can significantly enhance the understanding of the properties of single erbium dopants in silicon.

In the next chapter, the design, fabrication, and characterization of the one-dimensional photonic crystal cavities used in this work is described in detail.

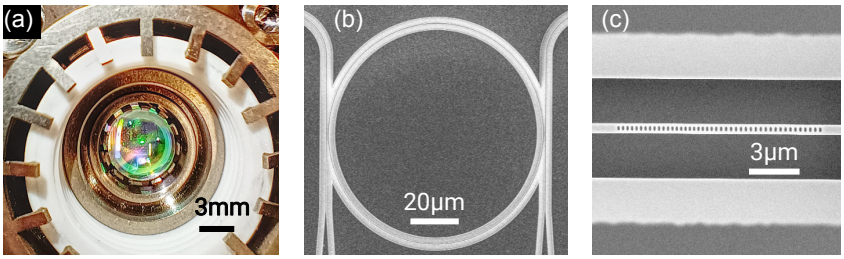

Figure 3.4.: **Comparison of different cavity types.** Different types of optical cavities in which erbium dopants in silicon can be investigated. The advantages and disadvantages of these cavities are discussed in the main text. (a) Optical image of an Fabry-Perot cavity formed by two mirrors with ultra-high reflectivity. (b) SEM micrograph of a ring resonator with two coupling waveguides. (c) SEM micrograph of a one-dimensional photonic crystal cavity formed by air holes in a waveguide.

4. Photonic crystal cavities

Nanophotonic one-dimensional photonic crystal cavities have been established as a leading platform for spin-photon interfaces with record cooperativities (Bhaskar et al. 2020) and Purcell enhancements (Ourari et al. 2023; Horvath et al. 2023) (Sec. 3.3). Silicon is a pristine material for fabricating of these devices due to the unrivaled maturity of available nanofabrication methods. Thus, the largest Q-factors (Asano et al. 2017) and the smallest mode volumes (Hu et al. 2018) achieved for photonic crystal cavities have been reported in silicon devices.

In this chapter, the concept of photonic crystals is introduced (Sec. 4.1). Starting from photonic band structure calculations, an optimized design process for one-dimensional photonic crystal cavities is outlined (Sec. 4.2). Then, optimized nanofabrication processes for these photonic crystal cavities are described (Sec. 4.3). To facilitate efficient prototyping, the photonic properties of the nanostructures are subsequently characterized at room temperature (Sec. 4.4). Moreover, techniques for tuning the resonance wavelength to the transition wavelength of the erbium dopants at cryogenic temperatures are discussed (Sec. 4.5).

4.1. Photonic crystals

Photonic crystal-based devices have been established as a versatile tool to modify the spatiotemporal properties of light modes on photonic chips (Joannopoulos 2008; Panuski et al. 2022). In general, photonic crystals are dielectric structures with a periodic modulation of the permittivity on the length scale of the optical wavelength in the material. In analogy to electrons or phonons in the solid-state, this periodicity leads to photonic Bloch modes supported in the material stack. This can be derived directly from the Maxwell equations in a medium without free charges or currents (Gross and Marx 2018):

$$\nabla \vec{B} = 0, \quad \nabla \times \vec{E} + \frac{\partial \vec{B}}{\partial t} = 0, \quad \nabla \vec{D} = 0, \quad \nabla \times \vec{H} - \frac{\partial \vec{D}}{\partial t} = 0. \tag{4.1}$$

The displacement field $\vec{D}$ can then be expanded in the electric field $\vec{E}$ (Joannopoulos 2008):

$$\frac{D_i}{\varepsilon_0} = \sum_j \varepsilon_{ij}\left(\vec{r},\omega\right) E_j + \sum_{j,k} \chi^{(2)}_{i,j,k}\left(\vec{r},\omega\right) E_j E_k + \sum_{j,k,l} \chi^{(3)}_{i,j,k,l}\left(\vec{r},\omega\right) E_j E_k E_l + \mathcal{O}\left(E^4\right). \tag{4.2}$$

with the vacuum permittivity ε_0 and the dielectric tensor ε_{ij}. For a photonic crystal consisting of air holes fabricated in the device layer of an SOI wafer, the dielectric tensor

is given by the scalar permittivities of silicon, silicon dioxide, and air, which are in good approximation isotropic and dispersion-free for wavelengths around the erbium transition at $\approx 1536\,\mathrm{nm}$, such that:

$$\varepsilon_{ij}\left(\vec{r},\omega\right) = \varepsilon\left(\vec{r}\right). \tag{4.3}$$

Importantly, the effect on the permittivity caused by the low erbium concentration $< 50\,\mathrm{ppm}$ in the silicon device layer (Sec. 2.3) can be neglected here. For small optical intensities, the expansion (Eq. 4.2) can be truncated after the linear term (Joannopoulos 2008). Nevertheless, we note that for centrosymmetric crystals such as silicon, the second order nonlinear term corresponding to the Pockels effect vanishes, i.e., $\chi^{(2)}_{i,j,k} = 0$ (Berciano et al. 2018). In contrast, the Kerr nonlinearity $\propto \chi^{(3)}_{i,j,k,l}$ is finite in silicon and may lead to small perturbations for very large optical powers (Sinclair et al. 2019).

Continuing with only the linear term and separating the spatial and temporal components, the following equation for the spatial solutions is derived (Joannopoulos 2008):

$$\nabla \times \left(\frac{1}{\varepsilon\left(\vec{r}\right)} \nabla \times \vec{H}\left(\vec{r}\right)\right) = \left(\frac{\omega}{c}\right)^2 \vec{H}\left(\vec{r}\right), \tag{4.4}$$

where $\mu_r \approx 1$ is used for the relative magnetic permeability of the material stack. This equation has the structure of an eigenvalue problem for the electromagnetic field represented by $\vec{H}\left(\vec{r}\right)$. Thus, the symmetries of the solutions of this equation are determined by the symmetries of the permittivity. In particular, a periodic modulation leads to periodic eigenmodes, which in turn give rise to photonic band structures of the guided modes (Joannopoulos 2008).

4.2. Design

A lattice defect in a photonic crystal can induce strongly localized modes. Photonic crystal resonators are devices that optimize the properties of these localized modes and use them as cavity modes (Akahane et al. 2003). To this end, dedicated engineering approaches have been developed for the design of the defect (Englund, Fushman, and Vuckovic 2005; Joannopoulos 2008). These optimization approaches are enabled by both finite-element methods (FEM) and finite-difference time-domain methods (FDTD). These methods numerically solve Maxwell's equations in time domain for different cavity designs such that key properties of the cavity modes, including Q-factors, mode volumes, and outcoupling efficiencies, and spatial mode profiles can be extracted (Joannopoulos 2008; Oskooi et al. 2010). Initially, photonic crystal cavities were designed by analyzing the scattering loss of the localized mode in Fourier space (Akahane et al. 2003; Srinivasan and Painter 2003). A key finding of this approach is that the spatial envelopes of the resonant modes should be Gaussian to maximize the Q-factors. Furthermore, this approach has been used to iteratively optimize the Q-factor by individually modifying photonic unit cells (Nakamura et al. 2016). This enabled the record Q-factor $Q \approx 1 \times 10^7$ observed experimentally for a photonic crystal resonator (Asano et al. 2017). Alterna-

tively, different numerical optimization methods are used to optimize the properties the cavity modes (Chan et al. 2012). To this end, genetic algorithms with a variety of fitness functions are applied to optimize for different cavity properties (Nguyen et al. 2019; Knall et al. 2022). In addition, genetic algorithms can also be combined with dedicated machine learning methods (Guimbao et al. 2022). Furthermore, photonic crystal cavity designs based on inverse design methods have also been proposed (Molesky et al. 2018).

In this work, a different design approach for one-dimensional photonic crystal cavities is used which was originally pioneered by (Quan and Loncar 2011). This design approach allows cavity designs with large Q-factors to be derived from photonic band structures without individually modifying photonic unit cells. This eliminates the need for computationally expensive optimization involving FEM or FDTD methods. Instead, this approach requires only photonic band structure calculations, which are computationally much cheaper (Oskooi et al. 2010), and a few FDTD simulations.

This design approach is presented in the following, starting with photonic band structures calculated for different unit cells (Subsec. 4.2.1). Based on these band structures, photonic crystal cavity designs with large Q-factors can be derived (Subsec. 4.2.2). Furthermore, different schemes are discussed which allow optimizing the cavity outcoupling efficiency (Subsec. 4.2.3). The designs are then finalized using FDTD methods (Subsec. 4.2.4).

4.2.1. Photonic band structures

The first step in designing a photonic crystal cavity is to choose the lattice, the fundamental unit cell, and the geometric degree of freedom which is used to induce the defect in the photonic lattice. The photonic unit cell used in this work comprises a single elliptical air hole in a silicon ridge waveguide (Fig. 4.1 a, inset), and the lattice is formed by a one-dimensional array of these unit cells. Elliptical air holes are advantageous over circular air holes because they maximize the width of the narrowest connections of the dielectric material in between two air holes, and between the air hole and the edge of the waveguide. Alternative unit cells include "alligator" (Burgers et al. 2019) or "sawfish" (Bopp et al. 2022; Pregnolato et al. 2023) designs, which are characterized by a variation of the waveguide width. As the sweep parameter to induce the geometrical defect, the lattice constant a is chosen, i.e., the length of the photonic unit cell which also corresponds to the distance between two air holes. In principle, the size of the air holes could also be used to induce the defect, e.g., by varying the hole radii (Quan and Loncar 2011; Quan, Deotare, and Loncar 2010), however, fabrication imperfections of air holes with diameters of about 100 nm can be strongly size dependent, so in principle, each hole size requires dedicated optimization.

For a given unit cell (waveguide width $w_y = 700\,\text{nm}$, waveguide thickness $w_y = 220\,\text{nm}$, semiaxes $h_x = 75\,\text{nm}, h_y = 162.5\,\text{nm}$, lattice constant $a = 358\,\text{nm}$), the first four photonic bands are then calculated numerically using the MPB library which is part of the MEEP software package (Oskooi et al. 2010). Fig 4.1 a shows the band structure along k_x, i.e., the momentum vector along the one-dimensional lattice. The modes located in the light cone (gray shaded) are not confined inside the silicon because the condition for

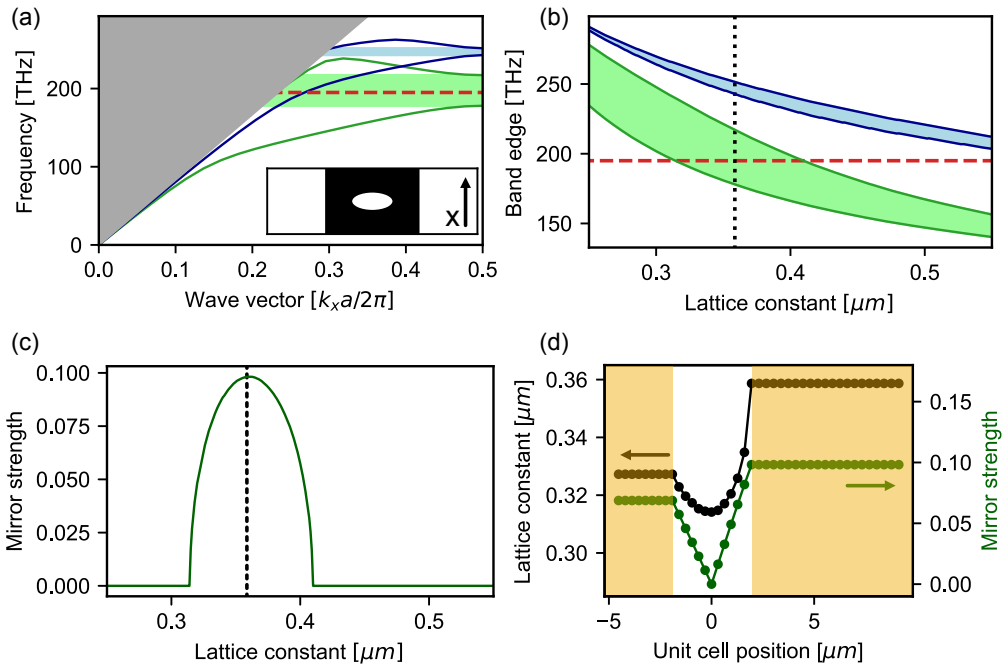

Figure 4.1.: **Photonic crystal cavity design from band structure calculation.** (a) (Inset) Top view of a unit cell of a one-dimensional photonic crystal with an elliptical air hole. (Main panel) The photonic band structure for the unit cell shows band gaps (green and blue shaded regions) between the two lowest lying quasi-TE (green) and quasi-TM (blue) bands. The resonance frequency of the erbium dopants (red dashed) is within the quasi-TE band gap. (b) Band edges (solid lines) and band gaps (shaded regions) for the quasi-TE (green) and quasi-TM (blue) bands as a function of the lattice constant, i.e., the length of the unit cell. With increasing lattice constant, the bands are shifted to smaller frequencies. The black dotted line indicates the lattice constant for which the full band structure is shown in (a). (c) Within the bandgap, the mirror strength of the unit cell is non-zero. For the target frequency (red dashed in b), the mirror strength is shown as a function of the lattice constant. The mirror strength is maximized in the center of the bandgap. (d) To form a cavity, the lattice constant of the first, e.g., $N_{\mathrm{taper}} = 7$ unit cells on both sides of the center are adapted such that the mirror strength is linearized. To facilitate efficient outcoupling through the coupling mirror (left), the mirror strength is only increased to a fraction of $\tilde{\gamma}_{\mathrm{coupling}} = 0.7$ relative to its maximum. In addition, extra unit cells (orange shaded) are added on both sides to increase the Q-factor.

total internal reflection is not fulfilled. Furthermore, the four guided modes obey two different parities and can thus be grouped into quasi-TE modes (green) and quasi-TM modes (Joannopoulos 2008). Photonic band gaps are observed for both parities (blue and green shaded). In general, the bands below the photonic band gaps, i.e., at lower frequencies, are called the dielectric modes, and the bands above the band gaps are called air modes. For the quasi-TE modes studied in this work, the principal electric field component of the dielectric mode is more strongly confined in the dielectric than the principal electric field component of the air mode (Joannopoulos 2008). For the given parameters of the photonic unit cell, the target frequency of the resonator $f_{\text{target}} = 195\,\text{THz}$, which is between the optical transition frequencies of the erbium dopants on sites A and B in silicon, is within the band gap of the TE-bands (red dashed).

To determine the photonic band gaps of different unit cells, it is sufficient to calculate the band edge frequencies, i.e., the frequencies at the edge of the unit cell in momentum space. Fig. 4.1 b shows these band edges for the first four guided modes depending on the lattice constant, i.e., the sweep parameter which induces the geometrical defect that generates the cavity mode. The band gaps for the different parities (green and blue shaded areas) shift to smaller frequencies with increasing lattice constant.

4.2.2. Linearzation of the mirror strength

The next step in the cavity design process is to calculate the mirror strengths. The mirror strength γ is the imaginary part of the complex k-vector, $k_x = k_{x,r} - i\gamma$, and is thus non-zero only within the photonic bandgap. For a given target frequency, the mirror strength can be calculated from the band edge frequencies for the different lattice constants a (Quan, Deotare, and Loncar 2010):

$$\gamma(a) = \sqrt{\left(\frac{f_2(a) - f_1(a)}{f_2(a) + f_1(a)}\right)^2 - \left(\frac{f_{\text{target}} - f_0(a)}{f_0(a)}\right)^2}, \quad f_0(a) = \frac{f_2(a) + f_1(a)}{2}, \tag{4.5}$$

with the dielectric band edge f_1, the air band edge f_2, and the mid-gap frequency f_0 (Quan, Deotare, and Loncar 2010). In Fig. 4.1 c, the mirror strength is plotted for the desired target frequency f_{target} and for quasi-TE parity.

Linearization of the mirror strength between adjacent unit cells leads to approximately Gaussian envelopes of the localized defect modes (Quan and Loncar 2011). These envelopes in turn lead to large Q-factors (Akahane et al. 2003).

The first step of composing the unit cells to a cavity design is choosing the lattice constant (or, more generally, the geometric sweep parameter) of the central photonic unit cell such that the dielectric band edge is resonant with the target frequency. Subsequently, a defined number of photonic unit cells N_{taper} is added on both sides of the central unit cell such that the mirror strength increases linearly until it reaches the maximum value for which the target frequency is exactly in the center of the photonic band gap (Fig. 4.1 d). In addition to these unit cells with tapered lattice constants, more unit cells with maximum mirror strength are typically added to further increase the Q-factor (Fig. 4.1 d, orange).

An intuitive understanding why a linearized mirror strength leads to approximately Gaussian envelopes can be gained by considering a plain-wave ansatz for the electric field $E(x) \propto e^{-ik_x x}$. Inserting the complex k-vector into this ansatz results in an oscillatory term $E(x) \propto e^{-ik_{x,r} x}$ and a damping term. The latter defines the envelope of the mode profile and becomes Gaussian for a generic linear mirror strength $\gamma(x)$:

$$E(x) \propto e^{-\gamma(x)x} \propto e^{-x^2}, \quad \text{for} \quad \gamma(x) \propto x. \tag{4.6}$$

4.2.3. Cavity-to-waveguide coupling

In this work, the cavities are designed for measurements in reflection. To this end, light is coupled in and out of the resonator by a feed waveguide which is attached to one mirror, i.e., the coupling mirror (Fig. 4.2 a). To facilitate efficient cavity outcoupling to the feed waveguide, an asymmetric cavity design is used in which the reflectivity of the coupling mirror is reduced compared to the back mirror. Albeit this reduces the Q-factor, the overall device performance may improve (Knall et al. 2022) depending on the application. Conventional designs typically realize this asymmetry by reducing the number of unit cells of the coupling mirror N_{coupling} compared to the number of unit cells of the back mirror N_{back} (Quan and Loncar 2011). A novel approach to optimize the outcoupling efficiency, recently introduced by (Knall et al. 2022), not only reduces the number of unit cells of the coupling mirror but also adjusts the relative maximum mirror strength of the coupling mirror to $\tilde{\gamma}_{\text{coupling}} = \frac{\gamma_{\text{coupling}}}{\max \gamma} \leq 1$ (Fig. 4.1 d).

In addition, the cavity-to-waveguide coupling efficiency can be improved by adding unit cells with tapered air hole sizes between the coupling mirror and the feed waveguide to improve the spatial mode matching (Knall et al. 2022). The number of these air holes is defined as N_{mm}.

4.2.4. Finite-difference time-domain simulations

To finalize the design, finite-difference time-domain (FDTD) simulations are applied which are implemented using MEEP (Oskooi et al. 2010). From these simulations, the Q-factor, the mode volume, the resonance frequency, and the spatial mode profile are extracted. By tuning the cavity design parameters, N_{taper}, N_{coupling}, and $\tilde{\gamma}_{\text{coupling}}$, the Q-factor and the mode volume can be adjusted. Importantly, this optimization does not involve an additional modification of individual photonic unit cells beyond linearizing the mirror strength. Thus, only few of these computationally expensive simulations are required to find suitable choices for the cavity design parameters. In addition, N_{back} is not optimized, but chosen such that it is significantly larger than N_{coupling} to facilitate an asymmetric design. Furthermore, the cavity resonance frequency calculated by FDTD deviates slightly from f_{target}. For given values of N_{taper}, N_{coupling}, and $\tilde{\gamma}_{\text{coupling}}$, this shift is approximately constant which is also reported in previous work (Quan and Loncar 2011). Thus, by tuning f_{target} of the cavity design, the resonance frequency is adapted to the desired frequency.

Applying this design approach, we find the following values for the cavity design

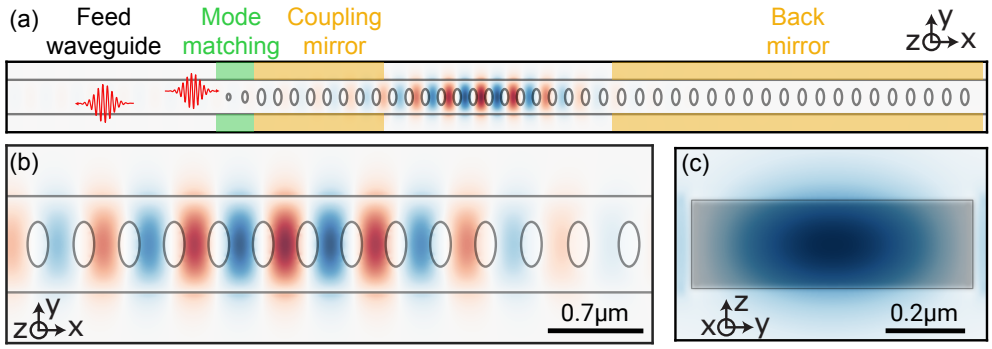

Figure 4.2.: **Finite-difference time-domain (FDTD) simulations.** (a) Top view of a one-dimensional photonic crystal cavity designed with the process described in the main text. From left to right, the cavity comprises a feed waveguide, $N_{\mathrm{mm}} = 2$ unit cells for spatial mode matching (green), a coupling mirror formed by $N_{\mathrm{coupling}} = 8$ unit cells with a relative mirror strength of $\tilde{\gamma}_{\mathrm{coupling}} = 0.7$ (orange), $N_{\mathrm{taper}} = 7$ unit cells with linearized mirror strengths on both sides of the center of the cavity, and $N_{\mathrm{back}} = 20$ unit cells forming the back mirror (orange). The amplitude of the principal electric field component of the fundamental quasi-TE mode, calculated with FDTD, is overlayed (red and blue). (b) Zoom into the central region of (a). (c) Cross-section at the center of the cavity, also overlayed with the principal electric field component of the fundamental quasi-TE mode.

parameters: $N_{\mathrm{taper}} = 7$, $N_{\mathrm{coupling}} = 8$, $\tilde{\gamma}_{\mathrm{coupling}} = 0.7$. Furthermore, $N_{\mathrm{back}} = 20$ and $N_{\mathrm{mm}} = 2$ are chosen independently to ensure the asymmetry and to improve the spatial mode matching, respectively (Fig. 4.2 a). For these settings, the FDTD simulation predicts a Q-factor of $Q = 0.68 \times 10^5$, a mode volume of $V = 0.83\,(\lambda/n)^3$, and a resonance frequency of $f_{\mathrm{sim}} = 1.9499 \times 10^5$ GHz corresponding to a resonance wavelength of $\lambda_{\mathrm{sim}} = 1537.5\,\mathrm{nm}$, for the fundamental cavity mode with quasi-TE parity. Fig. 4.2 b shows the amplitude of the principal electric field component of the latter at the center of the silicon device layer (colors). As expected, the electric field antinodes are located in the silicon layer where the erbium dopants will be integrated. In addition, Fig. 4.2 c shows a section perpendicular to the waveguide at the center of the cavity for the same mode.

4.3. Nanofabrication

The nanofabrication process of the photonic crystal cavities is similar to the one used for the in-house fabricated nanophotonic waveguides (Subsec. 2.3.3, App. A). However, the performance, in particular the Q-factors, of the nanophotonic cavities can be more severely altered by fabrication imperfections inducing excess scattering loss. To minimize

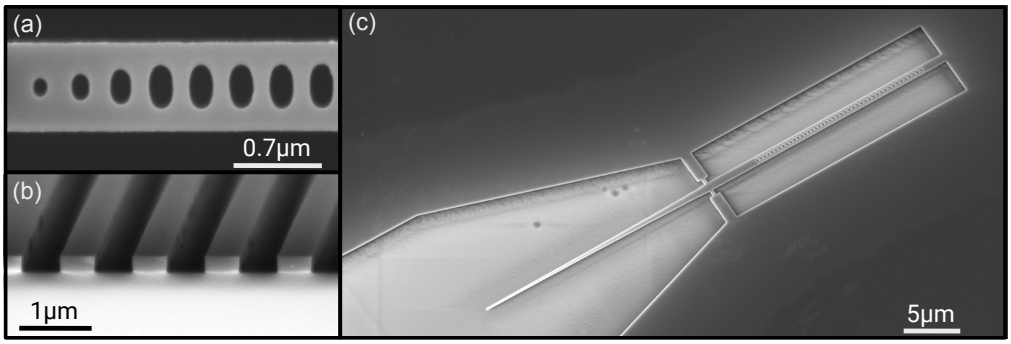

Figure 4.3.: **Nanofabrication of photonic crystal resonators.** To achieve the desired cavity properties, the electron beam lithography and reactive etching processes are optimized. (a) Scanning electron microscope (SEM) image. Top view of the first eight air holes of a photonic crystal cavity with $N_{\mathrm{mm}} = 3$ unit cells for mode matching. Smooth sidewalls and non-distorted, elliptical air holes indicate good electron beam lithography. (b) SEM image. After cleaving the sample perpendicular to photonic waveguides, their profile is inspected. Vertical sidewalls confirm the high anisotropy of the applied etching recipe. (c) SEM image. Suspended photonic crystal cavity after all steps of successful nanofabrication.

the latter, the nanofabrication process is optimized for smooth sidewalls for both the waveguide and the air holes (Fig. 4.3 a, b).

To achieve sidewalls with low line edge roughness, i.e., a smooth horizontal profile, the resist mask, fabricated by electron beam lithography, is optimized. To this end, proximity effect correction, including an over-dose under-size scheme, is applied (*BEAMER - GenISys GmbH* 2023). The latter improves the line edge roughness of the mask by exploiting the blurring effect of over-dose exposure while compensating the effect on the feature size. Furthermore, the resist is developed with n-amyl actetate and methyl isobutyl ketone kept at cold temperatures of 5 °C which also improves the line edge roughness (Ocola and Stein 2006).

To facilitate smooth, vertical etch profiles, the composition of the etch gases which provide chemical etching and sidewall passivation, i.e., SF_6 and O_2, is optimized together with the biasing of the etching plasma (de Boer et al. 2002; Nojiri 2015; Dussart et al. 2014; Yang et al. 2019). In contrast to the nanophotonic waveguides, the cavities are etched without Ar sputtering at another RIE machine.

Similar to the nanophotonic waveguides, the cavities comprise a tapered waveguide end which is used for adiabatic coupling to a tapered optical fiber. The theoretical limit for the coupling-efficiency using this approach increases from about 20 % to above 90 % when the BOX layer beneath the tapered waveguide is removed (Weiß 2022; Zeng et al. 2023; Nikbakht et al. 2015). The latter is facilitated by immersing the sample in hydrofluoric acid and subsequent drying using a critical point dryer. To guarantee

sufficient mechanical stability of the suspended device, additional support structures connect the nanostructures with the remaining silicon device layer (Fig. 4.3 c). For the photonic crystal cavities used in this work, this is feasible with only one pair of support structures. The width of the latter is about 200 nm for which the additional scattering loss is expected to be less than 5 % based on FDTD simulations. The experimentally achieved one-way coupling-efficiency of these suspended nanostructures is about 50 % (Pforr 2023) and is probably limited by angular misalignment between the fiber and the waveguide.

As an example for the final result of nanofabrication, an SEM micrograph of a fully processed, suspended one-dimensional photonic crystal cavity is shown in Fig. 4.3 c.

4.4. Characterization

After nanofabrication, the Q-factors, the cavity-to-waveguide coupling efficiency, and the resonance wavelength of the photonic crystal cavities are characterized at room temperature (App. B). Based on these characterization measurements, the cavity design and the nanofabrication processes can be optimized.

To detect the modes of the cavities, the wavelength-dependent reflection off the nanostructures is measured. A cavity mode is then indicated by a Lorentzian dip at its resonance wavelength (Eq. 3.10). From the linewidth of the Lorentzian, the Q-factor of the cavity mode (Eq. 3.4) is derived. In addition, the amplitude of the Lorentzian dip is given by the cavity-to-waveguide coupling efficiency, for which three different regimes are distinguished:

$$\frac{\kappa_{out}}{\kappa} = \frac{\kappa_{out}}{\kappa_{loss}+\kappa_{out}} \begin{cases} < 0.5, & \kappa_{out} < \kappa_{loss}, \quad \text{undercoupled}, \\ = 0.5, & \kappa_{out} = \kappa_{loss}, \quad \text{critically coupled}, \\ > 0.5, & \kappa_{out} > \kappa_{loss}, \quad \text{overcoupled}. \end{cases} \tag{4.7}$$

However, to distinguish between an undercoupled and an overcoupled cavity, it is necessary to not only measure the intensity of the reflected light but also its phase (Fig. 4.4 a) (Reiserer and Rempe 2015). In particular, the phase of the reflected light exhibits a jump ϕ_r when the laser wavelength is scanned over the resonance wavelength of the cavity mode. The magnitude of this phase jumps is proportional to the cavity-to-waveguide coupling efficiency:

$$\phi_r \begin{cases} < \pi, & \kappa_{out} < \kappa_{loss}, \quad \text{undercoupled}, \\ = \pi, & \kappa_{out} = \kappa_{loss}, \quad \text{critically coupled}, \\ > \pi, & \kappa_{out} > \kappa_{loss}, \quad \text{overcoupled}. \end{cases} \tag{4.8}$$

To facilitate a phase measurement (Jacobs 1988), a heterodyne setup is used (Früh 2020). The latter comprises a single laser which is frequency-shifted by 110 MHz using an AOM to form a local oscillator. The light is then reflected off the cavity. The local oscillator and the cavity reflection interfere at a beamsplitter and are detected with a

fast amplified photo diode (APD). The AC part of the electric output signal of the APD is then demodulated to its I and Q components using the 110 MHz source used for the local oscillator as reference. From I and Q, the amplitude A and the phase ϕ of the electric field reflected off the cavity can then be calculated as follows:

$$\phi = \arctan\left(\frac{I}{Q}\right), \quad A = \sqrt{I^2 + Q^2}. \tag{4.9}$$

The reflectivity of the cavity is proportional to the amplitude, i.e., $R \propto A^2$.

As an example, Figure 4.4 b and c show the reflectivity and the phase of two photonic crystal cavities with Q-factors of about 1×10^5. The first cavity mode (b) exhibits a dip to about 0.5 (Fig. 4.4 b). The phase measurement shows that the phase jump on resonance is smaller than π such that we can infer that the cavity mode is undercoupled (Fig. 4.4 c). In contrast, the second cavity mode (c) is found on a device with a more asymmetric cavity design. This results in a critically coupled cavity mode, i.e., it exhibits a reflectivity dip to almost 0 and a phase jump of about π.

Despite the careful optimization of the nanofabrication processes, residual feature-size fluctuations altering the waveguide width and the air hole sizes cannot be fully eliminated. In contrast to excess scattering loss, these imperfections do not dramatically reduce the expected Q-factors of the used cavity designs but shift their resonance wavelength away from the target wavelength given by the transition wavelengths of the erbium dopants on sites A and B. In particular, the fluctuations of the resonance wavelength exceed the limited tuning range of a few nanometers of optical wavelength (Sec. 4.5). Moreover, we find that on a single photonic chip, the wavelength fluctuations consist of a statistical and a systematic contribution. The latter causes wavelength fluctuations of tens of nanometers in between two subsequent nanofabrication runs and can significantly exceed the statistical fluctuations. To overcome this, a large number of photonic crystal cavities (≈ 100) with design wavelengths linearly varying over a range between 50 nm and 100 nm are fabricated on each sample. As an example, Fig. 4.4 d shows the detuning between the design wavelength and the measured wavelength for four different cavities with resonances spread over ≈ 50 nm. Importantly, sufficient Q-factors $Q > 0.7 \times 10^5$ are found for all of these cavities. This sample design ensures that on each photonic chip, at least a few cavities are within the accessible tuning range to the erbium dopants.

For spectroscopy on single emitters, a sample is then mounted in the cryogenic setup and cooled to temperatures of about 2 K (App. B). During the cooldown, the resonance wavelengths of the cavities exhibit a blue shift of about 15 nm due to the temperature dependent refractive index of silicon and thermal expansion. At cryogenic temperatures, the resonance wavelength of a large number of cavities is then measured to determine those which are within the tuning range. Figure 4.4 e shows the resonance wavelengths of approximately 50 cavities, spread over a wavelength range of about 20 nm. Here, statistical fluctuations of the feature-sizes cause wavelength shifts of a few nanometers.

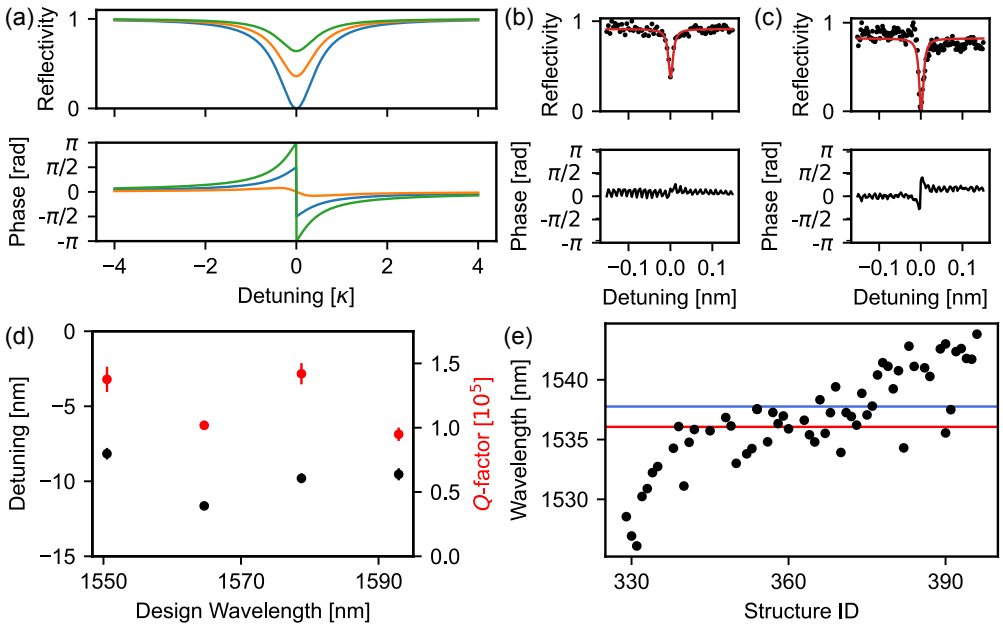

Figure 4.4.: **Characterization of photonic crystal cavities.** The Q-factor and the coupling regime of the fabricated photonic resonators are characterized in reflection. (a) Light reflected from an optical resonator exhibits different reflection dips and phase jumps on resonance depending on the coupling regime, i.e., overcoupled (green), undercoupled (orange) and critically coupled (blue). Only from the reflected intensity (top panel), an overcoupled resonator can not be distinguished from an undercoupled resonator. Instead, the phase needs to be measured (bottom panel). (b, c) Experimental data showing a critically (b) and an undercoupled (c) resonator. (d) To compensate for fluctuations of the resonance wavelength due to fabrication imperfections, up to a few hundred resonators are fabricated on each sample with design wavelengths swept over 50 nm to 100 nm. The detuning between the target wavelength and the design wavelength is about 10 nm exemplarily shown for four structures. In case of successful nanofabrication, most resonators show a high Q-factor $> 0.7 \times 10^5$. (e) At cryogenic temperatures, the resonance wavelengths of ≈ 50 resonators are measured. The large number of resonators within 20 nm guarantees that some resonators can be tuned on resonance with the erbium dopants on site A and B (blue and red horizontal lines).

4.5. Tuning

Despite the large number of cavities on a single photonic sample, it is very unlikely that the resonance wavelength of one of them perfectly matches the transition wavelength of the erbium dopants. Thus, tuning methods are required to trim the resonance wavelength inside the cryostat and at base temperature.

To tune the resonance wavelength of a photonic crystal cavity, the effective permittivity seen by the cavity mode needs to be modified. Inside the cryostat, this can be achieved by gas condensation. For this purpose, a suitable gas, e.g., argon, nitrogen, xenon, or carbon dioxide, is guided to the surface of the nanophotonic chip which is kept below the freezing point of the gas (Mosor et al. 2005). Thus, once the gas gets in contact with the sample surface, a thin layer of ice is created on the nanostructure, which has a different refractive index compared to vacuum. In this work, argon gas is used and further details on technical realization can be found in App. B. Since argon ice (as well as ice of the other gases) has a refractive index larger than one, the resonance wavelengths of the cavity experience a shift to longer wavelengths. The maximum tuning range which can be achieved with argon ice condensation is about 20 nm (Fig. 4.5 a), which is in good agreement with FDTD simulations. Remarkably, the Q-factor of the cavity is only slightly affected by the argon ice.

An intrinsic disadvantage of gas condensation is that the flow of gas cannot be interrupted fast enough to facilitate controlled tuning. In addition, the gas condensation is not selective to an individual cavity, but the thin layer of ice covers the entire sample. Therefore, to overcome these limitations, ice can be locally evaporated by exploiting resonant heating. To this end, a laser is coupled into the nanostructure, and its wavelength is ramped with a rate of a few Hertz over the resonance of the cavity mode. Then, the laser power is increased until the resonance wavelength starts to shift to longer wavelengths. This indicates that the ice in the vicinity of the cavity starts to evaporate. The onset of this effect is observed for approximately 10 µW at the feed waveguide. Importantly, this laser tuning technique is stopped intrinsically once the laser is no longer on resonance with the cavity such that, by choosing the range of the wavelength ramp, the desired tuning range can be precisely controlled (Fig. 4.5 b). We further note that the exchange gas in the sample space of the used cryostat is removed during the laser tuning procedure to reduce the thermalization of the ice with the VTI.

Combining the two aforementioned techniques, the resonance wavelengths of the cavity modes can be tuned over multiple nanometers with high precision. However, it is important to note that directly after the cooldown, the cavity wavelengths are not centered within this tuning range. Instead, tuning is only possible towards longer wavelengths.

Furthermore, an additional temperature-dependent shift of the resonance wavelength is observed between the base temperature of about 1.7 K and $\approx$ 4 K (Fig. 4.5 c). The resonance shifts to shorter wavelengths with lower temperatures indicating the formation of a layer with a refractive index larger than one on the cavities. In addition, with an increasing amount of argon ice on the resonators, a slight reduction of this temperature tuning range is observed. This effect is thus attributed to the He exchange gas inside the sample space which becomes liquid at this temperature and might form a thin film

covering the sample. Over the mentioned temperature range, the tuning range induced by this effect is only a few Gigahertz, which corresponds to a few linewidths for typical cavities studied in this work. Despite the small range, the advantages of this temperature tuning are that it is easily reversible and very precise.

The previously mentioned methods allow the precise tuning of photonic crystal cavities only at cryogenic temperatures. As an alternative, tuning by controlled oxidation of individual cavities can be applied. This could even be demonstrated on wafer-scale (Panuski et al. 2022) and allows tuning of a large number of resonators persistently on resonance with each other. However, due to the temperature required for the oxidation, this process might not be feasible after implantation of erbium dopants without hampering their properties (Sec. 2.2). Moreover, fast ($\approx 1\,\mu s$) and reversible tuning can be realized by controlling the distance between a pair of coupled, suspended one-dimensional photonic crystal resonators (Deotare et al. 2012). This would allow for tuning the cavity on and off resonance with individual dopants during experimental sequences.

Finally, in contrast to tuning the resonance wavelength of the cavity, the transition wavelength of the erbium dopants could also be tuned on resonance with cavity mode by applying electric or magnetic fields. This is particularly attractive for experiments in a high B-field regime where tuning the dopants over a range of multiple tens of Gigahertz may not fundamentally change the physical properties of the system.

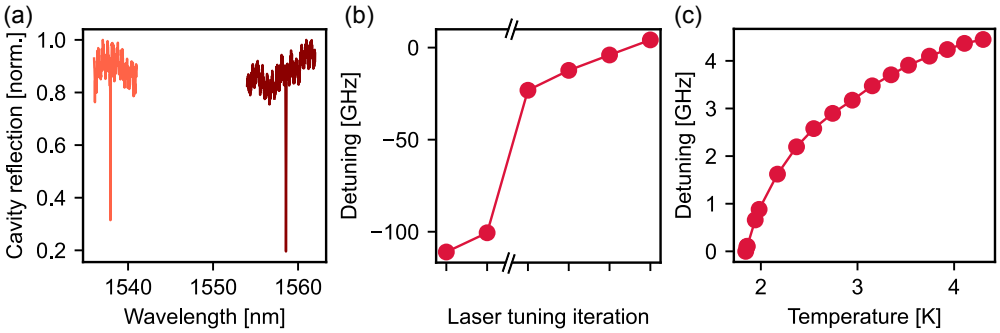

Figure 4.5.: **Tuning of photonic crystal cavities.** Argon gas is condensed onto the sample. (a) Because the refractive index of argon ice exceeds that of vacuum, the resonance of the cavity is shifted to longer wavelengths, with an observed maximum shift of $\approx$ 20 nm for suspended cavities. Remarkably, the Q-factor is only slightly altered by the argon ice. (b) Argon ice tuning is difficult to control. Overtuning, i.e., tuning of the resonance to a wavelength smaller than the target wavelength is hard to avoid. The excess ice can be melted again in a controlled way by applying a laser on resonance with the cavity mode. (c) In addition, a small temperature dependence of the cavity resonance is observed close to base temperature of the cryostat. In contrast to the other methods, this is easily reversible. This effect is attributed to the He exchange gas in the sample space as the effect starts at $\approx$ 4 K, i.e., at the temperature at which He becomes liquid.

5. Single erbium dopants in silicon

In this chapter, the properties of single erbium dopants embedded in silicon photonic crystal cavities are investigated. A part of these results has been published in (Gritsch, Ulanowski, and Reiserer 2023).

First, the sample that allowed the first observation of single dopants is introduced, and its limitations are described (Sec. 5.1). To overcome the latter, a new generation of optimized samples is designed and fabricated, and the experimental setup is improved (Sec. 5.2). In these nanophotonic devices, single erbium dopants are resolved spectrally, and their properties are studied. They show spectral diffusion linewidths as low as 13(5) MHz and Purcell enhancements up to 177. In addition, their emitted photons exhibit high single-photon purity $g^{(2)} < 0.02$. Furthermore, the electronic spin states of single emitters are resolved by applying an external magnetic field (Sec. 5.3). Then, the properties of a spin qubit encoded in a single erbium dopant are studied. First, the optical coherence of the bright state of such a qubit is investigated. In particular, optical Rabi oscillations are observed, and photon echo measurements reveal optical coherence times of $T_2 = 1.31(5)\,\mu s$ (Sec. 5.4). Furthermore, the eigenstates of such a qubit are initialized by optical pumping and read out by fluorescence state detection with a fidelity of 87.2(5) % (Sec. 5.5). In addition, direct driving of the spin transition using microwave pulses is demonstrated. On this transition, Rabi oscillations and a spin echo coherence time of $t_2 = 48(2)\,\mu s$ are observed (Sec. 5.6). Finally, these results are summarized, and an outlook on future measurements is given (Sec. 5.7).

5.1. First observation of single erbium dopants in a silicon photonic crystal cavity

For the first experiment targeting single emitters, a sample of type CVD as described in Chap. 2 is used. On this sample, photonic crystal cavities are fabricated with the following design parameters (Sec. 4.2): $N_{\mathrm{taper}} = 20$, $N_{\mathrm{coupling}} = 0$, $N_{\mathrm{back}} = 5$, $\tilde{\gamma}_{\mathrm{coupling}} = 1$, and $N_{\mathrm{mm}} = 0$. For these nanophotonic resonators, a mode volume of $V = 1.45\,(\lambda/n)^3$ is calculated by an FDTD simulation (Subsec. 4.2.4).

Using argon tuning (Sec. 4.5), a cavity with a Q-factor of $0.73(3) \times 10^5$ is tuned on resonance with the erbium dopants integrated at site B. This cavity mode is undercoupled and has a dip depth of about 0.3, corresponding to a cavity-to-waveguide coupling efficiency of about 10 % (Sec. 4.4). Since this resonator is not underetched, the fiber-to-chip coupling efficiency for this device is only about 10 %. In addition, in order to optimize the signal-to-noise ratio, the SNSPDs (App. B) are operated with a reduced quantum efficiency of only 40 %. This results in a relatively moderate detection efficiency for a

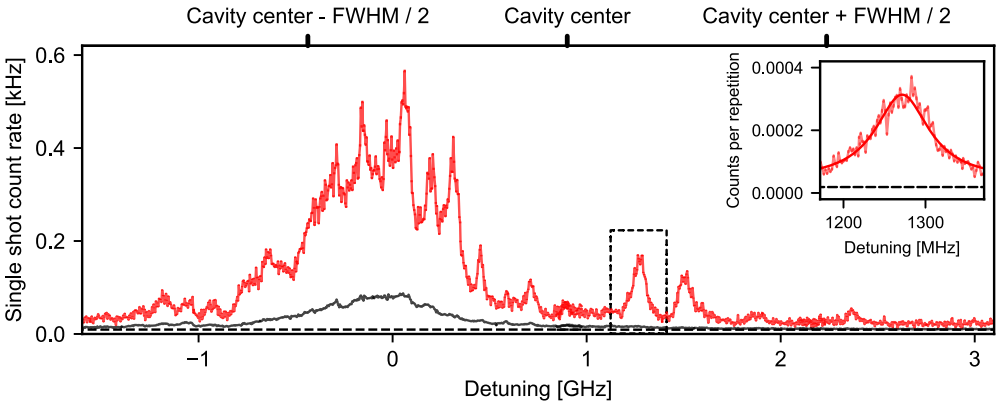

Figure 5.1.: **First observation of single erbium dopants embedded in a nanophotonic silicon cavity.** (Main panel) The fluorescence after resonant excitation is compared for two time intervals. On longer timescales, i.e., 10 µs to 48 µs after the excitation pulses, the signal (dark gray) shows a single Lorentzian peak corresponding to the inhomogeneous linewidth of the dopants in the feed waveguide which do not experience a Purcell enhancement. In contrast, within the first microsecond after the excitation pulses, the fluorescence exhibits several narrower peaks (red) which are attributed to single erbium dopants. (Inset) In the tail of this spectrum (dashed box in main panel), a single, well-resolved emitter is found.

single photon emitted into the cavity mode of about 0.1 %.

At the base temperature of the cryostat, i.e., 1.7 K, second-long spin lifetimes are expected (Sec. 2.9). In addition, the effective magnetic field at the position of the erbium dopants is likely to be non-zero since paramagnetic impurities, neighboring spins, and the Earth's magnetic field cause a non-zero Zeeman splitting of the optical transition. If this splitting is larger than the pulse bandwidth, spins can be pumped to the other Zeeman branch and thus end up in an effective dark state. To avoid this, the sample is heated to 14 K, which reduces the spin lifetime below the optical lifetime without broadening the erbium transition (Sec. 2.9). We then perform resonant fluorescence spectroscopy, similar to the experiments in nanophotonic waveguides, using laser pulses with a length of 0.4 µs and a square pulse shape, corresponding to a spectral resolution of about 1 MHz. These excitation pulses are repeated every 50 µs in order to adapt to the expected Purcell enhancement.

In the resulting fluorescence spectrum, two different timescales can be identified which are compared in the following (Fig. 5.1, main panel). First, a single peak (dark gray) is identified when the fluorescence is integrated over the time interval from 10 µs to 48 µs after the excitation pulses. Since the whole chip and not only the mode maximum of the photonic crystal cavity is implanted with erbium, this peak is attributed to the inhomogeneous distribution of the erbium dopants at site B integrated either within the

50 µm long feed waveguide or within the resonator volume, but not or not significantly enhanced by the Purcell effect. In contrast, about 20 peaks are observed in addition to this inhomogeneous distribution when the fluorescence signal is integrated only within the first 1 µs after the excitation pulses (red). We attribute these peaks on short timescales to individual erbium dopants coupled to the cavity mode such that their optical decay rate is significantly enhanced by the Purcell effect (Dibos et al. 2018; Ulanowski, Merkel, and Reiserer 2022). The inhomogeneous broadening of these single emitters is comparable to or exceeds the inhomogeneous broadening of the dopants which are not Purcell enhanced and is explained by the same effects, i.e., random strain fields and the mixed isotopic composition of the crystal (Sec. 2.7). The spectral diffusion linewidths of these peaks, which are extracted by individual Lorentzian fits, vary from 10 MHz to 100 MHz (Fig. 5.1 inset). Thus, the dopants are spectrally not well separated, making it difficult to address them individually. Combined with the background contribution from the non-coupled dopants and the low single-photon detection efficiency (Fig. 5.1 inset), this limits the ability to investigate the properties of individual dopants coupled to the cavity mode.

Because of these limitations, we now turn to a second, improved nanophotonic sample. However, we note that the results obtained on this device mark the first observation of single erbium dopants embedded in a nanophotonic silicon resonator including the resolution of the electronic spin states of a single emitter and the observation of coherent Rabi oscillations (Gritsch, Ulanowski, and Reiserer 2023).

5.2. Improved cavity

To overcome the limitations of the cavity mentioned in the previous section, a second generation of samples with optimized properties has been designed and fabricated. This second generation differs from the first generation in the SOI wafer used as the starting material, in the concentration and the implantation profile of the erbium dopants, and in the cavity design of the photonic crystal cavities (Subsec. 5.2.1). In the following sections, the focus of this work is on the results obtained with one of these optimized nanophotonic resonators. First, the maximum Purcell enhancement and the spatial distribution of the Purcell enhancement within this resonator is modeled and compared to the first cavity belonging to the first sample generation (Subsec. 5.2.2). Spectroscopic measurements on the optimized resonator then confirm that the improvements lead to significantly fewer and thus better addressable erbium dopants coupled to the cavity mode (Subsec. 5.2.3).

5.2.1. Sample properties and cavity design

The properties of the first (1. Gen) and the second (2. Gen) generation of samples are summarized and compared in Tab. 5.1. For the second generation of cavity samples, a CZ-grown SOI wafer with a device layer thickness of 220 nm and a BOX layer thickness of 3 µm is used. This wafer is then implanted at Innovion with a dose of $0.1 \times 10^{12}\,\mathrm{cm}^{-2}$, which corresponds to a 29-fold reduction compared to the first generation of samples.

Sample name	1. Gen	2. Gen
	Silicon-on-insulator wafer	
Growth method	CVD (*)	CZ
Manufacturer / vendor	UW, LSRL	SOITEC
Device layer thickness [µm]	0.19	0.22
BOX thickness [µm]	2	3
Device layer bonding	smart-cut	smart-cut
Resistivity [$\Omega\,\mathrm{cm}$]	unknown	$8.5 - 11.5$
Doping concentration [cm^{-3}]	undoped, (seed: unknown)	boron, 1×10^{15}
	Erbium implantation	
Site	IBS	Innovion
Dose [$10^{12}\,\mathrm{cm}^{-2}$]	2.9	0.1
Energies [MeV]	0.1, 0.35	0.25
Simulated peak concentration [cm^{-3}]	2×10^{17}	10^{16}
Isotopic content	^{170}Er, ^{167}Er (50 %:50 %)	^{166}Er, ^{167}Er, ^{168}Er
Angle	7°	7°
	Annealing	
Temperature [K]	800	800
During / post implantation	during	post
	Cavity design	
N_{taper}	20	7
N_{coupling}	0	8
N_{back}	5	20
$\tilde{\gamma}_{\mathrm{coupling}}$	1	0.7
N_{mm}	0	2
BOX removed	no	yes

Table 5.1.: **Sample overview.** Properties of the SOI wafers, implantation and annealing conditions, and cavity design of the two sample generations used for studying single erbium dopants. Abbreviations: Silicon Valley Microelectronics (SVM), Ion Beam Services (IBS), University Wafer (UW), and Lawrence Semiconductor Research Lab (LSRL). (*) Same as the CVD samples in Chap. 2.

The isotopes used for implantation are ^{166}Er, ^{167}Er, and ^{168}Er due to the precision of the available mass filtering. In addition, the dopants are implanted with a single energy of 250 keV, targeting the center of the silicon device layer to increase the fraction of dopants integrated near the field maximum of the cavity mode. During the implantation, the wafer is kept at room temperature. To cure the implantation induced defects, the samples are annealed at a temperature of 800 K for 1 min after implantation (App. A, Sec. 2.3.2).

On these samples, photonic crystal cavities with an optimized outcoupling efficiency are fabricated to increase the detection efficiency for a single photon emitted into the cavity mode. For this purpose, the asymmetry between the coupling mirror and the back mirror is significantly increased by choosing the following design parameters: $N_{\mathrm{taper}} = 7$, $N_{\mathrm{coupling}} = 8$, $N_{\mathrm{back}} = 20$, $\tilde{\gamma}_{\mathrm{coupling}} = 0.7$, and $N_{\mathrm{mm}} = 2$. A cavity with these design parameters is then tuned on resonance with the erbium dopants on site A and used for the subsequent spectroscopic measurements. After tuning with argon gas condensation and a resonant laser (Sec. 4.5), this cavity exhibits a mode with a Q-factor of $0.82(2) \times 10^5$. This cavity mode is further almost critically coupled such that the cavity-to-waveguide coupling efficiency is about 50 % (Sec. 4.4). This represents an approximately five-fold increase compared to the first sample generation. The increase in the Q-factor achieved in spite of the enhanced outcoupling is attributed to improvements of the nanofabrication recipes and to statistical fluctuations of the Q-factor (Sec. 4.3 and 4.4). Moreover, the mode volume $V = 0.83\,(\lambda/n)^3$, derived from FDTD simulations for the optimized cavity design, is only about 60 % of the mode volume of the first resonator.

5.2.2. Expected Purcell enhancement

Next, we calculate the expected maximum Purcell factor and estimate the number of dopants with a given Purcell enhancement for the improved cavity. These values are compared with those of the cavity used for the first study of erbium dopants embedded in a nanophotonic silicon resonator (Sec. 5.1). For both resonators, the maximum Purcell enhancement (Sec. 3.1) is derived from the measured Q-factors, the simulated mode volumes, and the branching ratio of 0.23(5) for the transition $Y_1 \rightarrow Z_1$ which is identical for both sites A and B (Sec. 2.6). From these values, maximum Purcell enhancements of $P = 1.7(1) \times 10^3$ and $P = 0.88(19) \times 10^3$ are found for the cavities of the second and the first sample generation, respectively. The improvement expected for the second sample generation is mostly resulting from the reduced mode volume of the optimized design.

In the fabricated devices, most dopants will exhibit a reduced Purcell enhancement because they are randomly distributed within the cavity due to the probabilistic ion implantation process and because their electric dipole vectors are not necessarily optimally aligned with the electric field in the cavity (Subsec. 3.1.2). To model these effects, random numbers representing the coordinates of individual emitters are drawn from the probability distributions representing the implantation profiles of the samples similar to Subsec. 2.4.2 and Subsec. 2.9.1. Since the orientation of the transition dipole moment is unknown for the erbium sites, the Purcell enhancement distribution is calculated for the three principal axes of the coordinate system. For each of these positions and dipole

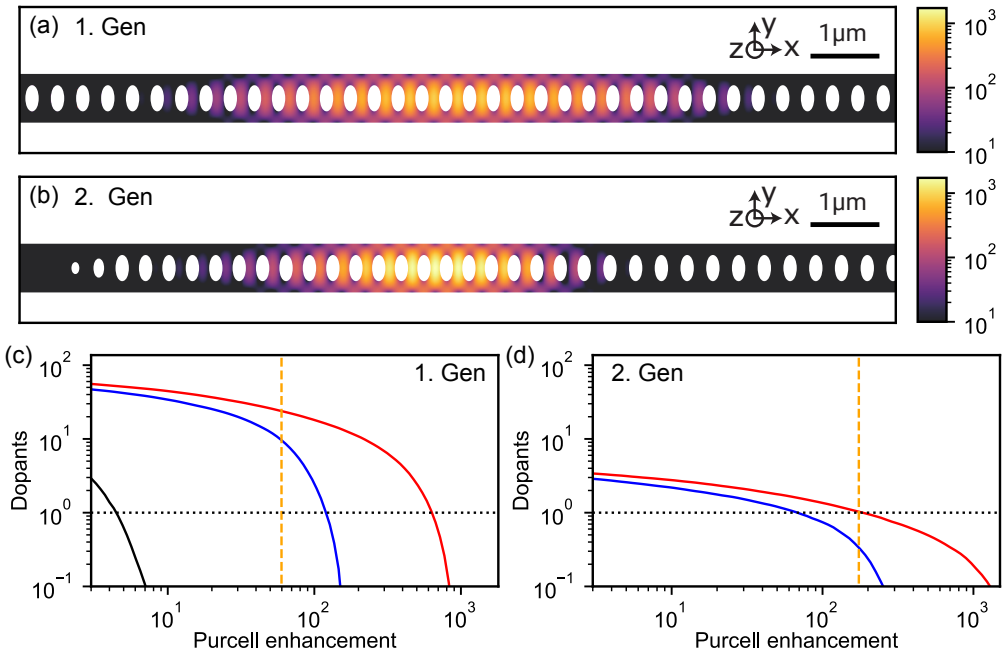

Figure 5.2.: **Purcell enhancement distribution in photonic crystal cavities.** Purcell enhancement (colors) at the center of the silicon device layer for the photonic crystal cavities studied on the first (a) and second (b) generation of samples. The slightly higher Q-factor and the reduced mode volume achieved for the improved cavity lead to a larger maximum Purcell enhancement. From these spatial mode distributions and the implantation profiles, the expected number of dopants with a Purcell factor exceeding the value on the x axis for dipoles orientated along the principal axes of the coordinates system (colors) are calculated for the first (c) and the improved (d) resonator. For each dipole orientation, an integration yield of 0.1 % is assumed. For both devices, the strongest enhancement is observed for dipoles along y (red), a weaker enhancement along x (blue), and no significant enhancement along z (black). The black dotted lines represent an expectation value of one. In particular, for the improved cavity, this one-dopant expectation value is significantly smaller than the maximum Purcell enhancement. In addition, the largest experimentally observed Purcell enhancement is indicated for each cavity (orange dashed, Sec. 5.3).

orientations, the Purcell enhancement is then calculated using the spatial mode profiles of the electric field components (Fig. 5.2 a, b).

A distribution of the Purcell enhancements for each dipole orientation is deduced by binning the resulting values. These distributions are rescaled using the implantation dose of the respective sample and assuming an integration yield of 0.1 % for each dipole orientation based on the measurements with erbium ensembles (Subsec. 2.9.5). After rescaling, the distributions are cumulated so that they describe the expectation value for the number of dopants exceeding a given threshold value for the Purcell enhancement (Fig. 5.2 c, d).

For both cavities, the dipoles oriented along y (red) experience the strongest Purcell enhancement, as expected, since the principal electric field component of the cavity mode is oriented along this direction. Dipoles oriented along x (blue) experience a weaker but still significant Purcell enhancement in contrast to dopants oriented along z (black) for which almost no Purcell enhancement is expected.

For the cavity belonging to the first generation of samples (Fig. 5.2 c), we find that the Purcell enhancement for which the expectation value for the number of dopants exceeds one is close to the maximum Purcell enhancement. In contrast, due to the much smaller implantation dose used for the second cavity generation, the Purcell enhancement at this one-dopant threshold is reduced by almost an order of magnitude compared to the maximum Purcell enhancement for the cavity with the improved design.

To overcome the latter without increasing the total number of dopants, which would again lead to spectral overlapping of single dopants hindering selective addressing, masked implantation can be applied for future samples. To this end, not the entire silicon device layer but only a small region around the center of the cavity mode is doped with erbium. Using the electron lithography technology available in our cleanroom and taking into account the expected horizontal straggle from numerical simulations (Ziegler, James 2023), it should be feasible to integrate emitters only within a volume with a radius of about 50 nm around the maximum of the cavity mode. In this case, almost all emitters will experience the maximum Purcell factor.

5.2.3. Spectroscopy

For the spectroscopic measurements on the improved cavity, an optical single-sideband modulator is added to the setup. The latter increases the frequency bandwidth of subsequent excitation pulses to 1.4 GHz compared to about 0.1 GHz achieved with the AOMs. In addition, the improved setup allows addressing of transitions within 14 GHz with a single laser field. This overcomes the requirement to keep the sample at temperatures for which the spin lifetime is expected to be short compared to the optical lifetime because in each experimental sequence both Zeeman branches can be addressed. Instead, the sample is now kept within the tuning range of the temperature tuning (Sec. 4.5).

In addition to the improved cavity-to-waveguide outcoupling, the improved cavity is also underetched (Sec. 4.3), i.e., the BOX layer beneath the waveguide taper is removed so that the fiber-to-chip coupling efficiency is increased to about 50 %. The combination of these improvements leads to an overall detection efficiency for a single photon emitted

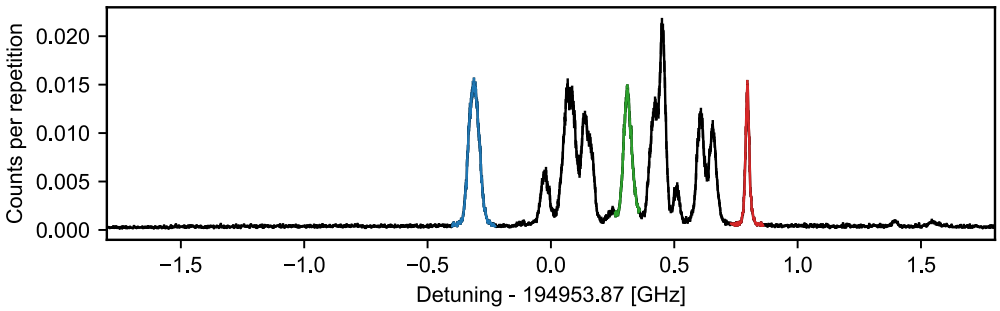

Figure 5.3.: **Fluorescence spectroscopy on improved device.** Resonant fluorescence spectroscopy similar to Fig. 5.1, but on the cavity belonging to the second generation of samples. The reduced dopant concentration in the resonator entails that more individual dopants can be selectively addressed and that the broadband background is strongly suppressed compared to the first device. Three of the single emitters (colors) are studied in further detail. In addition, the absolute fluorescence signal recorded after each repetition is significantly improved due to the optimized cavity design and nanofabrication processes.

in the cavity of about 5 %. This corresponds to a 50-fold increase compared to the first device.

Figure 5.3 shows the fluorescence spectrum of the improved cavity integrated within the first 20 µs after excitation pulses with a length of 150 ns. In comparison to the first sample generation, almost no signal originating from dopants coupled to the feed-waveguide is observed. Instead, the data shows only a small number of peaks which are again attributed to single emitters. At least three of these emitters are sufficiently well-isolated such that they can be selectively addressed (blue, green, and red). Similar to the first cavity, the inhomogeneous distribution of the single dopants is about 1 GHz and hence comparable to the value obtained with the ensembles. Thus, removing the BOX layer beneath the cavity, which is expected to change the local strain environment, does not strongly influence the inhomogeneous distribution.

5.3. Single dopants

We now turn to the properties of the three single erbium dopants, which are colored in Fig. 5.3. In particular, the Purcell enhancement (Subsec. 5.3.1), the spectral diffusion linewidth (Subsec. 5.3.2), and the purity of the emitted photons (Subsec. 5.3.3) are investigated. Furthermore, the electronic spin states of the dopants are resolved by applying an external magnetic field (Subsec. 5.3.4).

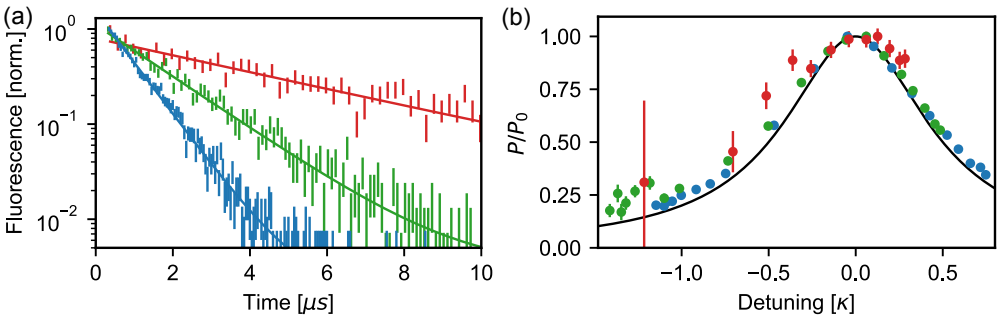

Figure 5.4.: **Purcell enhancement.** The cavity resonance is tuned across the inhomogeneous linewidth by temperature tuning. (a) For each dopant, the largest Purcell enhancement is observed when the cavity is exactly on resonance with their transition frequency. Extracting the lifetime from exponential fits to the fastest observed decays shows that the blue dopant exhibits the largest Purcell enhancement ($T_1 = 0.803(11)\,\mu s$, $P = 177(2)$), followed by the green ($T_1 = 1.59(3)\,\mu s$, $P = 89(2)$) and the red dopant ($T_1 = 4.83(20)\,\mu s$, $P = 29.4(10)$). (b) The Purcell enhancement is normalized to the maximum for each dopant and plotted as function of the cavity detuning in units of the cavity linewidth. The datasets follow the theory curve according to Eq. 3.4 (black) without free parameters.

5.3.1. Purcell enhancement

First, the Purcell enhancement of the three colored dopants is measured. For this purpose, the cavity is tuned across the inhomogeneous linewidth using the temperature tuning approach (Sec. 4.5). For each frequency setpoint of the cavity, a fluorescence scan is recorded. The time-resolved fluorescence is then integrated in frequency within a FWHM around the center of the spectral diffusion linewidth and fit with an exponential fit model. From these fits, the lifetimes are extracted which in turn are used to derive the Purcell enhancement by comparing these values to the bulk lifetime of site A (Sec. 2.8).

As expected, the shortest optical lifetimes, and hence the largest Purcell enhancements, are found when the cavity is exactly on resonance with the single dopants (Fig. 5.4 a). Comparing the three dopants, we find the largest Purcell enhancement for the blue emitter $P = 177(2)$, followed by the green $P = 89(2)$ and the red $P = 29.4(10)$ one.

Furthermore, the Purcell enhancement is measured as a function of the detuning of the resonator. The datasets show that the Purcell enhancement follows the expected (Eq. 3.4) Lorentzian behavior (Fig. 5.4 b). This confirms that the reduction of the optical lifetime can be attributed to the cavity enhancement.

The largest observed Purcell enhancement is about ten-fold lower than the theoretical maximum for the cavity. The main contributions to the discrepancy are attributed to both the imperfect dipole alignment and the spatial position of the dopant relative to the

maximum of the cavity mode. Remarkably, this experimentally observed value for the maximum Purcell enhancement is close to the one-dopant threshold shown in Fig. 5.2 for dipoles orientated along y. However, we note that more data, i.e., more dopants embedded into different resonators, is needed for a quantitative analysis.

While the position of individual dopants cannot be changed after nanofabrication, the dipole orientation can be modified using a superconducting vector magnet which would allow rotating the spin with respect to the cavity mode (Raha et al. 2020). However, such a magnet was not available.

Still, already at the current stage, the measured Purcell enhancement is larger than that reported in many other experiments with quantum dots (Lodahl, Mahmoodian, and Stobbe 2015) and color centers in diamond coupled to nanophotonic resonators (Bhaskar et al. 2020; Ruf et al. 2021). Furthermore, the Purcell enhancement is comparable to that of erbium dopants in macroscopic Fabry-Perot resonators (Ulanowski, Merkel, and Reiserer 2022; Ulanowski et al. 2023) (Tab. 5.2). In comparison to the record values, demonstrated with erbium dopants in MgO and $CaWO_4$ evanescently coupled to nanophotonic silicon resonators, the measured Purcell enhancement in this work is only six, respectively five times smaller (Ourari et al. 2023; Horvath et al. 2023).

Albeit the value of P is well-suited to characterize the performance of the resonator, the absolute value of the shortened lifetime is more important for practical purposes as it sets the repetition rate for many quantum information processing operations. This work on erbium dopants in silicon thus stands out, vastly because of the exceptionally fast optical lifetime for sites A and B compared with erbium in other host materials (Sec. 2.8, Sec. 2.11). The lifetimes of all three dopants reported here are shorter than the shortest lifetime of 7.4 µs observed for a single erbium dopant in any other host crystal (Ourari et al. 2023). In particular, the optical lifetime of the blue dopant is about nine times shorter than this value.

5.3.2. Spectral diffusion linewidth

The narrowest spectral diffusion linewidth of 13.5(5) MHz is observed for the red dopant (Fig. 5.5). Furthermore, the blue and the green emitters show spectral diffusion linewidths of 47(3) MHz and 32.7(16) MHz, respectively. All of these spectral diffusion linewidths are more than two orders of magnitude larger than the lifetime-limited linewidths calculated for each dopant from their Purcell enhanced lifetimes (blue: 0.198(3) MHz, green: 0.100(3) MHz, red: 0.033(1) MHz). The spectral diffusion linewidths do not show a dependence on the Purcell enhancement of the dopant, which is tested by tuning the resonance frequency of the cavity with respect to the dopants. In addition, the optical power of the excitation pulses are chosen such that the spectral diffusion linewidths are not power-broadened, and the measured linewidths are much larger than the bandwidth (≈ 3 MHz) of the 150 ns-long excitation pulses.

Thus, the spectral diffusion has to be attributed to microscopic noise sources that may be detrimental to applications in quantum technologies. The variation of these spectral diffusion linewidths hints towards local broadening mechanisms such as fluctuating charge traps at the nearby surfaces which are a known problem for semiconductor

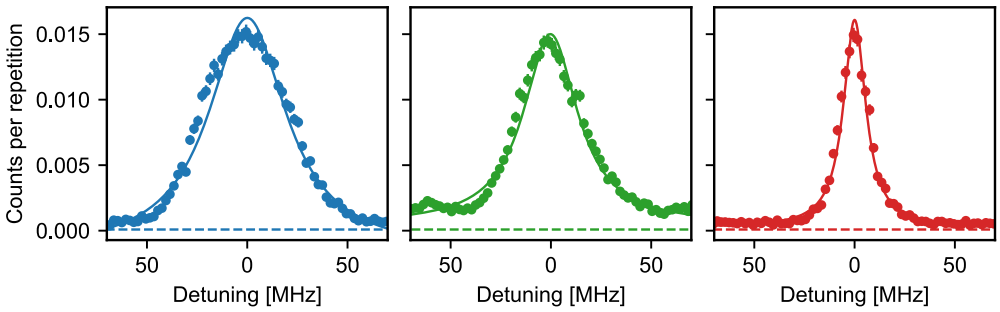

Figure 5.5.: **Spectral diffusion linewidth.** The spectral diffusion linewidths for the three dopants are obtained from Lorentzian fits to the data. The narrowest spectral diffusion linewidth, about 13.5(5) MHz, is observed for the red dopant, followed by the green and the blue emitter with linewidths of 32.7(16) MHz and 47(3) MHz, respectively.

quantum devices (Kuhlmann et al. 2013). This challenge is also known for erbium dopants in other host materials where the ratios between the spectral diffusion and the lifetime-limited linewidths are on the same order of magnitude or even larger than in this work (Tab. 5.2).

An important exception are sites for which the static electric dipole moment is strictly zero because of symmetry constraints such that dopants integrated at these sites cannot exhibit first order Stark shifts (Phenicie 2021). Accordingly, erbium dopants integrated on such a site in $CaWO_4$ show spectral diffusion linewidths which are only less than one order of magnitude larger than their lifetime-limited linewidth (Ourari et al. 2023).

Compared with the T center in silicon, the emitters studied here exhibit ratios of the spectral diffusion linewidth and the lifetime-limited linewidth which are up to 30-fold smaller than the average value observed in micropucks (Higginbottom et al. 2022) and about 60-fold smaller than the value reported for a T center coupled to a nanophotonic cavity (Johnston et al. 2023).

5.3.3. Single-photon purity

The spectral lineshape and the measured reduction of the optical lifetime give already a strong indication that the colored peaks in Fig. 5.3 are indeed single emitters. To confirm this and to extract the purity of the emitted single photons, the autocorrelation function $g^{(2)}$ is measured.

To obtain the latter, a Hanbury Brown and Twiss interferometer is not necessary because the dead time of our superconducting single-photon detector is < 10 ns and hence about two orders of magnitude shorter than the lifetime of the emitters. Accordingly, $g^{(2)}$ can be extracted by correlating all photon detection events recorded on the detector during a repeated pulsed fluorescence experiment. To this end, all photon detection events within one optical lifetime after the excitation pulse are taken into account.

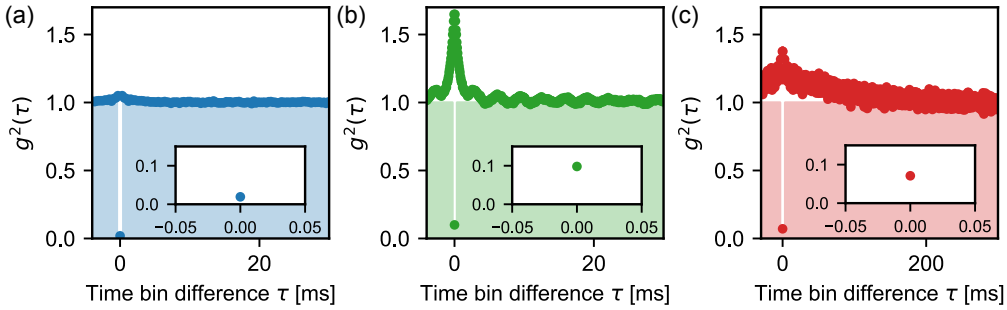

Figure 5.6.: **Autocorrelation measurements.** The autocorrelation function $g^{(2)}$ is measured for all three dopants, and clear anti-bunching at zero delays is observed for all dopants (insets): (a) blue: $g^{(2)}(\tau = 0) = 0.019(1)$; (b) green: $g^{(2)}(\tau = 0) = 0.071(8)$; (c) red: $g^{(2)}(\tau = 0) = 0.098(2)$. For non-zero delays, the green and the red dopant show a clear bunching indicating spectral diffusion on longer timescales. Moreover, the bunching of the green dopants clearly shows a modulation, which implies a periodically evolving contribution to its spectral diffusion.

Moreover, for this measurement, the length of the excitation pulses and the pulse amplitudes are optimized individually for each dopant so that the anti-bunching $g^{(2)}(\tau = 0)$ is minimized. To this end, pulses with lengths of 20 ns, 25 ns, and 50 ns are used for the blue, green, and red dopant, respectively. The bandwidths ($\approx$ 10 MHz to 30 MHz) are thus still comparable or even narrower than the spectral diffusion linewidth of the respective dopant. Compared to our previous work, these measurements benefit vastly from the more than 50-fold increased single-photon detection efficiency (Gritsch, Ulanowski, and Reiserer 2023).

The autocorrelation functions show clear anti-bunching at zero delay and thus confirm that all three peaks are single emitters (Fig. 5.6). The highest photon purity of $g^{(2)}(\tau = 0) = 0.019(1)$ is observed for the blue dopant (Fig. 5.6 a, inset). The small residual value is attributed to detector dark counts. Similar photon purities are found for erbium dopants in other host crystals (Ourari et al. 2023) and for color centers in silicon coupled to nanophotonic resonators (Islam et al. 2023; Johnston et al. 2023; Saggio et al. 2023).

The blue dopant shows almost no bunching for non-zero time delays. In contrast, the green dopant exhibits a strong bunching in this regime which clearly shows an additional modulation (Fig. 5.6 b). The latter indicates that the transition frequency of this dopant is influenced by a periodically evolving system. The latter might be a two-level system such as another close-by erbium or ^{29}Si nuclear spin rotating in a magnetic field. The red dopant also exhibits bunching at non-zero delays, however, no signs of a dominating modulation are observed (Fig. 5.6 c). In addition, the bunching decays on a more than ten-fold longer timescale.

For the green and the red dopant (Fig. 5.6 b, c, insets), slightly larger values of

$g^{(2)}(\tau = 0) = 0.071(8)$ and $g^{(2)}(\tau = 0) = 0.098(2)$, respectively, are found for the antibunching at zero delay. This residual fluorescence is attributed to the unwanted excitation of other cavity-coupled dopants and of dopants coupled to the feed waveguide which are either integrated on site A or belong to the broadband background (Sec. 2.5). We note that, in comparison to our initial work, this background contribution is drastically reduced due to the lower dopant concentration in the new device (Gritsch, Ulanowski, and Reiserer 2023).

5.3.4. Resolving the spin states

After focusing on the optical properties of the single dopants, we now turn to their electronic spin. For this purpose, an external magnetic field is applied along the (100) axis of the silicon host crystal. Thus, the degeneracy of the spin-1/2 Zeeman levels is lifted similarly to Sec. 2.10. In contrast to our earlier work, the sample is kept at temperatures below 5 K, i.e., in a regime for which the electron spin lifetimes are expected to significantly exceed the repetition interval of the fluorescence measurements of about 30 µs. These long spin lifetimes are overcome by sufficiently strong excitation pulses which are able to reset the spin state. Possible mechanisms for the reset of the spin state include the off-resonant excitation of the spin and the subsequent decay along its spin-flip transition, and the excitation of other spins in the vicinity of the emitter which then in turn flip the spin. Such neighboring spins may be erbium dopants integrated at other sites, in particular also those sites which contribute to the broadband background. An additional explanation would be a change of the electric environment in the nanostructure, e.g., due to the creation of free charge carriers which may also induce spin flips (Wolfowicz et al. 2021). Although the reset of the spin state is beneficial for the spectroscopic measurements presented in the following, it may be detrimental for the performance of a spin qubit encoded in these states (Sec. 5.5).

The resonant fluorescence signal is recorded while increasing the setpoint of the applied magnetic field from 0 mT to 100 mT in steps of 20 mT (Fig. 5.7). For clarity, an offset on the y-axis proportional to the applied field is added to every dataset. As a guide to the eye, the spectra for each magnetic field setpoint are colored where the spin-preserving transitions of the three dopants from the previous measurements (blue, green, red) and of an additional dopant (orange) are observed. Because of their different splittings in the magnetic field, the four dopants can be grouped into two magnetic classes. For the first magnetic class, to which the red and the green dopants are attributed, an effective g-factor $\Delta g = |g_g - g_e|$ for the spin-preserving transitions of $\Delta g = 2.05(6)$ is extracted. This value is in good agreement with one of the effective g-factors observed in the ensemble measurement (Sec. 2.10, Tab. 2.5). For the second magnetic class (blue and orange dopants), an effective g-factor of $\Delta g = 0.30(2)$ is found. The latter slightly deviates from the second value observed in the ensemble measurements. The deviation might be caused by sample misalignment with respect to the magnetic field axis. Within each magnetic class, the single dopants exhibit slightly different effective g-factors, which may be explained by the inhomogeneous distribution of the spin transitions. To further study this effect, more single dopants need to be measured in future devices.

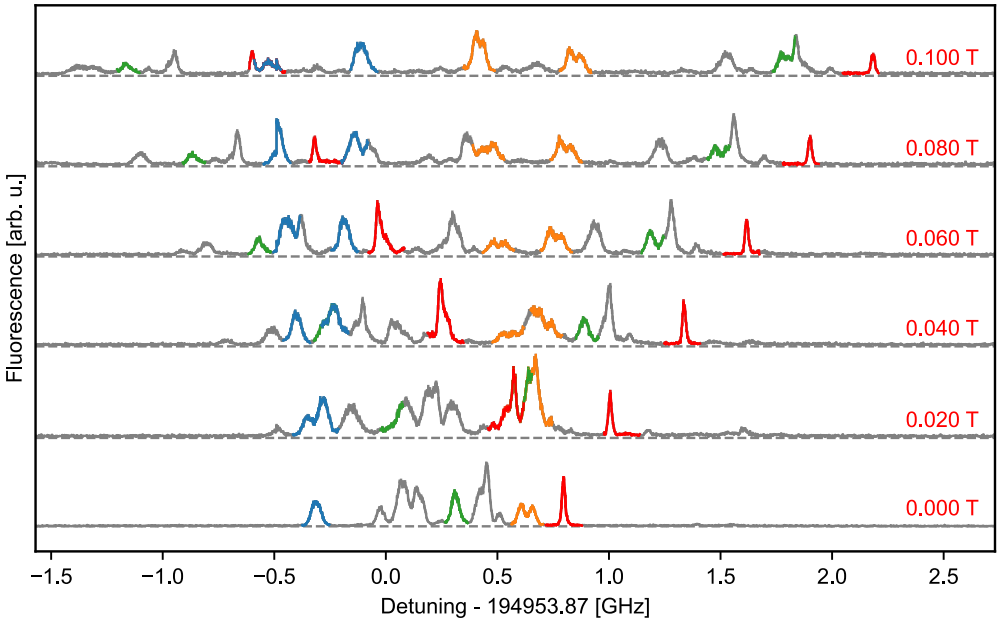

Figure 5.7.: **Resolving the electronic spin.** An external magnetic field is applied along the (100) direction of the host crystal and increased in steps of 20 mT so that the Zeeman levels of the dopants are resolved spectrally in the fluorescence signal. To the latter, a y-offset proportional to the magnetic field setpoint is added for clarity. As a guide to the eye, the frequency range around the Zeeman states of four dopants are colored. We observe that the dopants belong to two magnetic classes (blue and orange, red and green) with different effective g-factors as expected from the ensemble measurements (Sec. 2.10). For small magnetic field setpoints, a deviation from a linear splitting is observed which is attributed to magnet hysteresis effects.

For small magnetic fields, the splittings seem to deviate from a linear behavior, which is attributed to some hysteresis of the magnetic field at the position of the sample. Thus, in this section, the effective g-factors have been calculated only from the resonance frequencies extracted at 100 mT.

To provide further evidence that the peaks which are associated to a single emitter in the previous measurement indeed belong to each other, a pump-probe scheme can be applied. For this purpose, 500 pump pulses with a pulse length of 100 ns and a detuning f_{pump} relative to the transition frequency at zero field are applied. After each of these pump sequences, a resonant fluorescence spectrum is recorded by varying the probe detuning f_{probe} and using pulses with a length of 200 ns to increase the spectral resolution. The intensities of all pulses are chosen so that, in comparison to the first measurement, the probability of excitation-pulse induced spin resets is significantly reduced. Thus, in

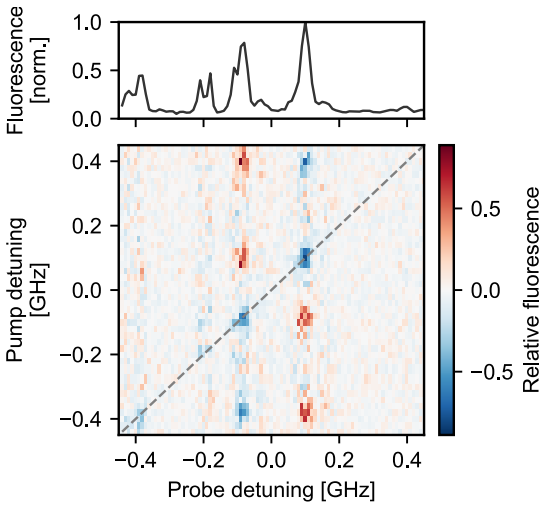

Figure 5.8.: **Pump-probe map.** To determine which peaks belong to the same dopant, a pump-probe measurement scheme is used. To this end, 500 pump pulses with a detuning of f_{pump} are applied prior to each measurement of the probe spectrum. (Top panel) The fluorescence after the probe pulses, averaged for all pump detunings, is used as the baseline. (Main panel) The increase or decrease of the recorded fluorescence relative to this baseline depending on the pump detuning reveals that the two large peaks in the top panel belong to the same dopant. Furthermore, the spin-flip transitions can be identified. The magnet is set to 45 mT. Black dashed line (guide to the eye): $f_{\mathrm{pump}} = f_{\mathrm{probe}}$.

combination with the sufficiently long spin lifetimes, the spin states can be polarized by the pump pulses.

Using this pump-probe scheme, a dopant which belongs to the magnetic class with the smaller splitting ($\Delta g = 0.30(2)$) between the spin-preserving transitions is investigated at a magnetic field of 45 mT (Fig. 5.8). The resonant fluorescence, averaged over all pump detunings, shows 4 peaks. Here, we focus on the two largest peaks belonging to the single emitter of interest which are centered within the probe detuning range (Fig. 5.8, top panel). The main panel shows the deviation of the fluorescence from its averaged level depending on the pump detuning. In particular, blue areas correspond to a reduction of the fluorescence indicating that the pump sequence reduces the population of the spin state at the respective probe detuning. As an example, this is observed for identical pump and probe detunings $f_{\mathrm{probe}} = f_{\mathrm{pump}} \approx \pm 0.1\,\mathrm{GHz}$. Accordingly, red areas indicate that the fluorescence increases because of the pump sequence. In particular, the combination of the reduced fluorescence of the peak which is addressed by the pump fields with the increased fluorescence on the other peak demonstrates that the peaks belong to the same dopant and that its spin states can be polarized. Furthermore, the data shows that the

spin states are also polarized for two pump detunings at $f_{\mathrm{pump}} = \pm 0.4\,\mathrm{GHz}$ in addition to the two spin-preserving transitions. These pump detunings are also symmetrically split around the transition of the dopant at zero field and are thus identified as the spin-flip transitions (Fig. 5.8). An effective g-factor of 1.2(1) is extracted for the spin-flip transitions which is proportional to the sum of the g-factors in the ground and the excited state $|g_g + g_e|$. In addition, the spin-flip transition and the spin-preserving transition which similarly polarize the spin states can be assigned to the same ground state. Thus, the ground-state g-factor $g_g = 0.76(5)$ and the excited-state g-factor $g_e = 0.45(5)$ can be unambiguously inferred.

The spin-flip transitions are barely visible in the averaged probe spectrum (Fig. 5.8, top panel), which is attributed to a dominant branching of the decays of the excited states via the spin-preserving transitions, i.e., a large cyclicity of the latter. Therefore, pumping on the spin-flips rapidly polarizes the spin to its other ground state, and the spin-flip transitions becomes dark. Importantly, we note that the detuning of the spin-flips is still significantly smaller than the cavity linewidth. Thus, the large cyclicity of the spin-preserving transition either indicates that the dipoles are favorably aligned by the external magnetic field (Raha et al. 2020) or that the cyclicity of this magnetic class is also large in absence of a cavity mode. The latter hypothesis is supported by the ensemble measurements in which a spin-flip transition with this effective g-factor could not be identified (Sec. 2.10, Tab. 2.5).

The dataset shown in Fig. 5.8 was taken on the same cavity but during a previous cooldown for which the center frequencies of the dopants were slightly different. These shifts are attributed to random strain fields generated by, e.g., the condensed argon gas. The center frequency of the dopant was close to the center frequency of the blue dopant.

Finally, we note that performing the same measurement on another dopant belonging to the second magnetic class reveals a ground-state g-factor of $g_g = 11.5(5)$ and an excited-state g-factor of $g_e = 9.4(5)$.

5.4. Optical coherence

In the previous section, we demonstrated that the electronic spin states of a single erbium dopant can be spectrally resolved and polarized by optical pumping. In this setting, a single spin qubit can be encoded in the electronic spin states of the optical ground state of the emitter. In the following section, the properties of such a spin qubit are investigated. To this end, we focus on the blue dopant of the previous measurements. Furthermore, a magnetic field of 0.3 T is applied such that the splitting between the spin-preserving transitions is about 1.25(5) GHz, and the splitting between the spin-flips is 5.2(2) GHz. The cavity is then tuned on resonance with one of the spin-preserving transitions. Due to this choice of the applied magnetic field setting, an additional enhancement of the cyclicity is expected because the spin-flip transitions are now detuned by more than one cavity linewidth.

We start the investigation of the properties of the spin qubit by measuring the optical coherence of the qubit. The optical coherence is paramount for interference-based

entanglement protocols (Sec. 3.2) (Reiserer 2022). First, optical Rabi oscillations are measured (Subsec. 5.4.1). Then, to determine the optical coherence time, photon echo sequences are used (Subsec. 5.4.2).

5.4.1. Optical Rabi oscillations

To measure optical Rabi oscillations, the fluorescence is recorded as a function of the electric field amplitude of the excitation pulses (Fig. 5.9 a). This measurement is repeated for multiple excitation pulse lengths varying from 15 ns to 100 ns. Thus, the frequency bandwidth of the excitation pulses is changed from about 30 MHz to 4.5 MHz. For all pulse lengths, an oscillatory behavior on an increasing background can be observed with larger electric field amplitudes. This oscillatory behavior is a clear signature of coherent Rabi oscillations. With increasing pulse lengths, the amplitudes of the coherent oscillations decrease. This is attributed to two effects: First, the excitation-pulse bandwidth is significantly smaller than the spectral diffusion linewidth of the emitters which entails a reduced excitation probability. Furthermore, the amplitude of the modulation decreases if the pulse length is comparable with the optical coherence time T_2. To separate these effects, the latter can be directly measured using a photon echo technique (Subsec. 5.4.2).

Remarkably, the residual fluorescence recorded after an optical 2π-pulse seems to be unaffected by the excitation pulse length, while the signal recorded after a π-pulse decreases with increasing pulse length (Fig. 5.9 b). To investigate this effect further, the fluorescence signal showing the Rabi oscillations, which is recorded within the first 3 µs (Fig. 5.9 c, blue), is compared with the signal measured between 7 µs and 10 µs after the excitation pulses (black: as measured). The latter is also rescaled for clarity (gray) such that its dependence on the electric field amplitude can be compared with the fluorescence on short timescales.

In the later time interval, i.e., about seven optical lifetimes after the excitation pulses, the fluorescence of the dopant is expected to be about three orders of magnitude smaller than in the earlier time interval. The signal exceeds this value, indicating a small contribution to the fluorescence originating from other dopants with longer optical lifetimes. However, the dependence of this signal on the electric field amplitude of the excitation pulses deviates clearly from the background signal on shorter timescales around which the Rabi oscillations are observed (Fig. 5.9 c, blue). Hence, this background fluorescence cannot be attributed directly to the other, weakly coupled dopants in the nanostructure.

Instead, also the fluorescence recorded after 2π-pulses seems to stem predominately from the dopant which undergoes the Rabi oscillations. This is confirmed by lifetime measurements. To this end, the time-resolved signals recorded after π- (Fig. 5.9 d, red) and 2π-pulses (black) for two different pulse lengths (25 ns: diamonds and 75 ns: crosses) are compared. In all four cases, the same optical lifetime is extracted from fits to the data. To understand this effect in detail, further investigations are necessary. As a first step, similar measurements may be recorded on several dopants with different spectral diffusion linewidths. Moreover, Rabi oscillations with even shorter excitation pulse lengths can be measured. In the current setup, this is hindered by the rise times of the AOMs of about 6 ns. To overcome this, electro-optical amplitude modulators might

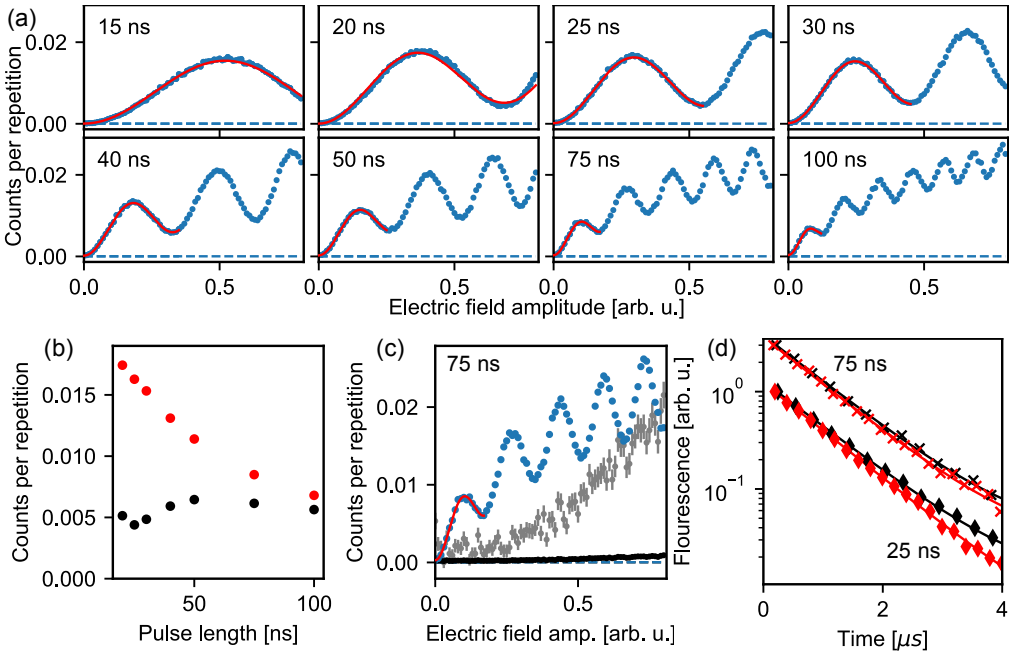

Figure 5.9.: **Optical Rabi oscillations.** (a) For pulse lengths ranging from 15 ns to 100 ns, the resonant fluorescence (blue) is recorded depending on the electric field amplitude of the excitation pulses. For all pulse durations, clear signatures of coherent Rabi oscillations on an increasing background are observed. From fits (red) to the data between zero and the first minimum, π- and 2π-pulse amplitudes are extracted (b) The fluorescence signal observed after a π-pulse (red dots, first maximum in a) decreases with increasing π-pulse duration which is attributed to the decreasing bandwidth. However, the fluorescence signal observed after a 2π-pulse (black dots, first minimum in a) does not show a clear dependence on the excitation pulse length. The background fluorescence also originates from the dopant under investigation. (c) To demonstrate this, the fluorescence signal recorded after pulses with a length of 75 ns is integrated in two different time intervals. In particular, the signal measured within the first 3 µs (blue) is compared with the signal recorded between 7 µs and 10 µs after the excitation pulses (black). To enhance the visibility, the latter is also rescaled to the maximum of the fluorescence on short timescales (gray). Albeit the fluorescence in the later time interval increases slightly with larger electric field amplitudes indicating the excitation of other emitters, its general dependence clearly deviates from the signal around which the oscillations occur. (d) The fluorescence after both, the π- (red) and 2π-pulses (black), decays with the same lifetime, i.e., the lifetime of the emitter, which is exemplarily shown for pulse lengths of 25 ns (diamonds) and 75 ns (crosses). The data is normalized and offset along y-axis for clarity.

be used, with which pulse lengths of about 1 ns can be realized. In this regime, the pulse bandwidth would then exceed the spectral diffusion linewidth by about one order magnitude.

5.4.2. Photon echo

The dephasing of the optical transition of the qubit is studied with a photon echo measurement scheme (Fig. 5.10 a inset) (Ulanowski, Merkel, and Reiserer 2022). The photon echo sequence consists of three pulses with the same length. The amplitude of the first pulse is chosen such that it corresponds to an optical $\pi/2$-pulse which creates a coherence between the optical ground and excited state for one spin orientation. After half of the sequence length $T_{\mathrm{seq}}/2$, an optical π-pulse, i.e., a pulse with twice the amplitude of the first pulse, is applied to cancel the static detuning between the laser and the emitter. After an additional waiting time of $T_{\mathrm{seq}}/2$, a second $\pi/2$-pulse is applied to rotate the state of the emitter to the ground or to the excited state depending on the relative phase to the first pulse. In particular, for a relative phase of 0 (π), the emitter should be in the excited (ground) state at the end of the pulse sequence. To probe this, the fluorescence is recorded within the first 3 µs after the last pulse for both relative phases depending on the sequence length T_{seq} (Fig. 5.10 a, b). The obtained datasets clearly show a difference in the fluorescence signals for the two different input phases. This difference corresponds to the photon echo amplitude (Fig. 5.10 c, d). The decay of the echo for increasing sequence lengths is well-fit with a single exponential model.

This measurement is then repeated for more pulse lengths. The echo amplitude obtained from the exponential fits to the decay decreases as a function of the pulse length (Fig. 5.10 e), which is expected due to the decreasing pulse bandwidth compared to the spectral diffusion linewidth. The fit to the data shows that the decrease is inversely proportional to the pulse length and thus in turn linear in the bandwidth. Remarkably, the optical coherence time, which is also extracted from the fit to the echo decay, increases with the pulse length. In particular, for the longest pulses with a length of 300 ns, an optical coherence time of $T_2 = 1.31(5)$ µs is observed. The latter corresponds to 66(3) % of the lifetime-limit of $T_2 \leq 2T_1$.

The increase of the coherence time with longer pulses may indicate that shorter, and thus stronger, excitation pulses cause decoherence of the emitter. Possible reasons for this effect are that the pulses alter the electric environment of the dopant by creating free charge carriers, either due to two-photon absorption or due to optically active erbium complexes or by changing the state of neighboring charge traps. Thus, to minimize this effect, samples with the lowest possible impurity concentration should be studied. Furthermore, dedicated termination of the surfaces of the nanophotonic structure might reduce the number of charge traps, and integration of the p-i-n diode into the device layer may help to stabilize the electric environment also during the excitation pulses. In addition, strong excitation pulses may induce decoherence by resonant or off-resonant excitation of the other emitters which in turn lead to instantaneous spectral diffusion of the emitter. This effect may be reduced in samples with lower dopant concentration. However, for the given integration yield on the preferred sites, the expected number of

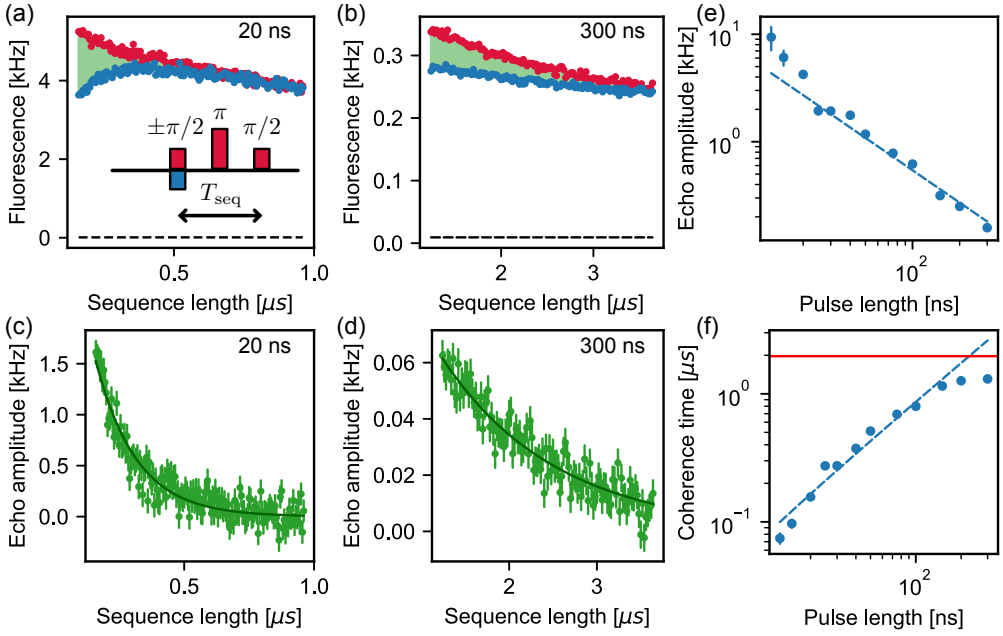

Figure 5.10.: **Single-dopant photon echo.** (a, inset) To study the optical coherence time T_2, a photon-echo measurement scheme is applied. For this purpose, an optical $\pi/2$-pulse creates a coherent superposition between the optical ground and excited states of one spin orientation. After half of the sequence length $T_{seq}/2$, a π-pulse is applied to compensate for a static detuning between the qubit and the laser. After waiting again for $T_{seq}/2$, another $\pi/2$-pulse is applied, which transfers the state to either the excited or back to the ground state, depending on the phase of the first $\pi/2$-pulse. (a, b) The fluorescence signal recorded after the second $\pi/2$-pulse for both input phases (red and blue) depending on the sequence length for two different input pulse lengths: 20 ns and 300 ns. (c, d) For each pulse length, the echo amplitude is then calculated by subtracting the fluorescence signals of the different input phases from each other. The decays of the echos are well-fit with a single exponential function (dark green). (e) The echo amplitude decreases ($\propto 1/x$, dashed) and (f) the optical coherence time increases with increasing duration of the input pulses. Before the saturation sets in, the increase of the coherence time in the pulse length is well-fit with a linear fit model (dashed).

dopants with a large Purcell factor per nanophotonic cavity will be significantly smaller than one which reduces the scaling potential of the material platform (Fig. 5.2, Subsec. 5.2.2). To overcome this, it is crucial to enhance the integration yield.

5.5. Fluorescence state detection

For all entanglement protocols, it is paramount that the state of the qubit can be retrieved after each repetition of the experiment. This is also called single-shot readout (SSRO) and can be achieved by fluorescence state detection.

Here, the state of the spin qubit is identified by probing the optical spin-preserving transition which is on resonance with the cavity, i.e., the optical transition associated with the bright state. In an ideal system, the state of the spin could be inferred if a photon is detected or not after such an excitation pulse. However, the detection efficiency for a single photon is only about 5 % (Sec. 5.2). Therefore, in absence of a detected photon, it is impossible to discriminate between photon loss and the spin being in its dark state. To overcome this, the optical transition is probed repeatedly, and the detected fluorescence photons are cumulated (Reiserer 2022; Raha et al. 2020). Then, a threshold number of photons is defined which is used to distinguish between the dark state and the bright state.

This readout scheme demands that the state of the spin is not changed during the experimental sequence, which entails two requirements: First, the spin lifetime needs to be longer than the sequence length. Second, the decay of the optically excited state needs to preserve the spin orientation. To this end, the relevant figure-of-merit is the cyclicity $\tilde{C}$ which is related to the number of excitation pulses n_0 that can be applied until the autocorrelation function $g^{(2)}$ decays to $1/e$ (Raha et al. 2020):

$$\tilde{C} = n_0 p_{\mathrm{ex}} \tag{5.1}$$

with the probability p_{ex} to create an excitation by the applied probe pulses. Importantly, the cyclicity can be significantly enhanced by embedding the spin qubit into an optical resonator (Sec. 3.2) (Raha et al. 2020).

In the following, we optimize the fidelity of such a fluorescence state detection scheme for the qubit encoded in the electronic spin states of the erbium dopant by tuning the number of readout pulses and the threshold number of photons. For this purpose, the qubit is first initialized in either the dark or the bright state by optical pumping on the respective spin-flip transition (Subsec. 5.3.4). The advantage of pumping on the spin-flip transition is that due to the dominant decay via the spin-preserving transition, the spin states can be quickly polarized. We note that in the current setting, the spin-flips are spectrally close enough to the cavity transition such that they can still be driven efficiently. If the spin-flip transitions would be further detuned, e.g., for a dopant which belongs to the second magnetic class of site A, driving of the spin-flip transition could still be facilitated with an orthogonal polarization of the excitation light field for which the photonic crystal cavity is transparent.

After initialization of the spin state, up to $N_{\mathrm{probe}} = 1000$ pulses are applied on the

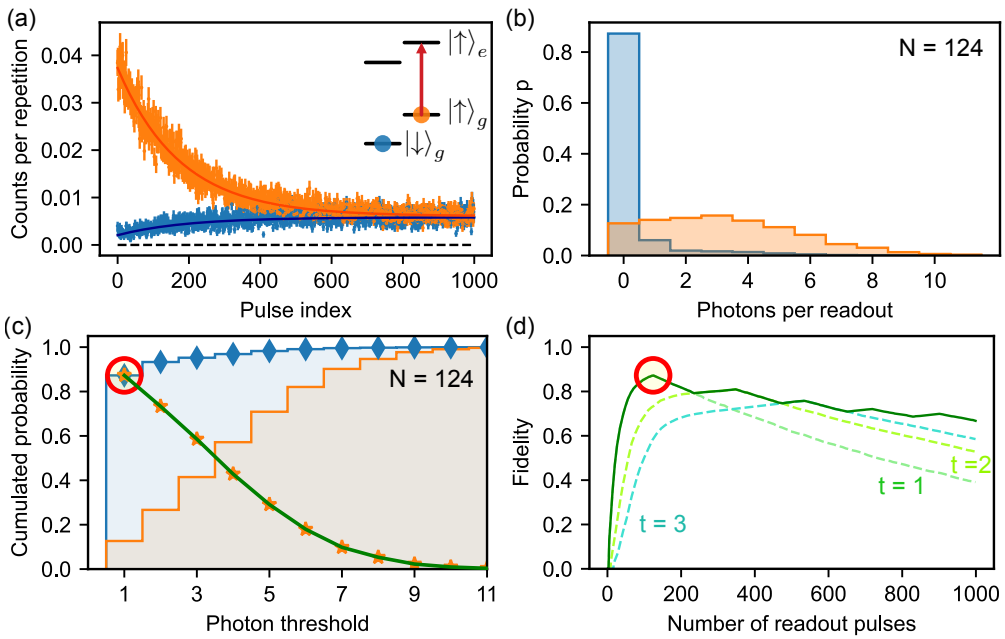

Figure 5.11.: **Fluorescence state detection.** (a, inset) The spin state of the qubit is initialized by optical pumping on the spin-flip transitions in either the bright (orange) or the dark (blue) state. The system is then probed by N readout pulses resonant with the spin-preserving transition of the bright state (red arrow). (a) Recorded fluorescence depending on the index of the readout pulses. When the qubit is prepared in the bright state, a large fluorescence signal is detected at the beginning of the readout sequence, which decreases to $1/e$ within about 175 readout pulses. When the qubit is prepared in the dark state, almost no fluorescence is observed initially. (b) By analyzing the click traces of each repetition of the readout sequence, the probability distributions to detect a certain number of photons during the first $N = 124$ pulses depending on the initialized state are reconstructed. (c) Using the corresponding cumulated distributions (colored area), the fidelity for the fluorescence state detection can be determined. To this end, for each value of the photon threshold t, which corresponds to the largest number of photon detection events still associated with a dark state, the probability to predict the dark (blue diamonds) and the bright (orange stars) states correctly is calculated. The overall fidelity for a certain value of the photon threshold t is given by the minimum of the individual fidelities. The optimal fidelity, 87.2(5) %, is found for $t = 1$. (d) Fidelity depending on the number of readout pulses for thresholds of $t = 1, 2, 3$ (lightgreen, green, lightblue, dashed) and with simulateneous threshold optimization (dark green).

spin-preserving transition of the bright state (Fig. 5.11 a). For this purpose, pulses with a length of 25 ns are used. The amplitude is further chosen such that these pulses are approximately $\pi/2$-pulses, i.e., the probability of creating an excitation for each pulse is about $p_{\mathrm{ex}} = 0.5$. Depending on the spin state, a significant difference of the fluorescence is observed indicating successful initialization. After the spin is initialized in the bright state, the fluorescence decays with an increasing number of readout pulses. From an exponential fit to the data, a cyclicity of $\tilde{C} = 88(10)$ is extracted.

In contrast, after the spin is initialized in the dark state, the fluorescence increases with more readout pulses. The number of pulses which can be applied until the equilibrium fluorescence is reached is comparable for both the dark and the bright state. A possible explanation would be that the cyclicity is limited by the spin lifetime. However, varying the delay time between subsequent readout pulses shows almost no impact on the obtained cyclicity. Instead, this again indicates that the used excitation pulses, even when applied off-resonantly, can induce spin-flips and thus reset the spin (Subsec. 5.3.4). This spin-reset effect is still attributed to resonant or off-resonant excitation of other emitters in the vicinity of the qubit. The pulse parameters used in this section are a trade-off between minimizing this effect and facilitating significant excitation probability per shot for a fast readout.

Next, the probability distributions for the number of photons detected during a single readout sequence of $N = 124$ is reconstructed for both the bright and the dark state (Fig. 5.11 b). For this purpose, the photon detection events after each repetition of the readout sequence are cumulated. The reconstructed probability distributions are significantly different from each other, which is expected because of the good contrast between the two qubit states (Fig. 5.11 a). For the dark state, the largest probability is found for the detection of zero photons. In contrast, the probability distribution of the bright state is more flat with a maximum at three detected photons.

Based on these probability distributions, the readout fidelity of the applied pulse sequence can be calculated. To this end, the photon threshold t, which represents the minimum number of detected photons during a readout sequence for which the spin state is estimated as bright, is varied from one to eleven (Fig. 5.11 c). For each photon threshold, the fidelities for the dark (blue diamonds) f_{dark} and the bright (orange stars) f_{bright} state are calculated individually from the probability distributions. The overall fidelity of the readout is then given by the minimum of these two fidelities $f = \min\left(f_{\mathrm{bright}}, f_{\mathrm{dark}}\right)$.

For the given number of readout pulses, $N = 124$, the optimal value for the threshold is found as $t = 1$. For the threshold, we determine an overall fidelity of 87.2(5) %. We note that this fidelity also includes the initialization fidelity such that the fidelity of the fluorescence state detection is expected to be slightly larger. In particular, an estimate for the initialization fidelity of 95(1) % is obtained by calculating the ratio of the fluorescence signals of the bright and the dark state averaged over the first ten readout pulses. Thus, a fidelity of 92(1) % is inferred for the spin readout.

In addition, Fig. 5.11 d shows the fidelity depending on the number of readout pulses with simultaneous optimization of the photon threshold t (solid line, dark green). The fidelity exhibits several local optima, each of them corresponding to a certain value of the photon threshold t (dashed lines, different colors).

These results represent the first optical single-shot readout of a spin qubit in silicon. The readout time, which is given by the sequence length of about 10 µs times the number of the readout pulses, is approximately 1.24 ms. A comparably fast readout with a larger fidelity of 97 % could be demonstrated for erbium dopants in $CaWO_4$ (Ourari et al. 2023). Still, the readout of single erbium dopants is much slower than the state detection schemes which have been realized for color centers in diamond, that benefit from significantly shorter optical lifetimes. In particular, single-shot readout of the spin of a NV center is possible with a fidelity about 97 % in only 4 µs (Hensen et al. 2015). Furthermore, for the SiV center, a significantly larger readout fidelity of 99.98 % in 30 µs could be achieved by exploiting the modification of the cavity reflection by a single strongly coupled emitter (Bhaskar et al. 2020).

In future experiments, the fluorescence state detection of a single erbium dopant can be sped up by further increasing the Purcell enhancement. In addition, the fidelity can be improved by enhancing the cyclicity of the erbium transition. For this purpose, samples with a lower dopant concentration will be investigated in which spin-flips induced by neighboring emitters are expected to be suppressed. Furthermore, the cyclicity may be optimized either by aligning the spins with a vector magnet along an axis for which the spin-flip probability of the optical decay is minimized or by operating the spin qubit in a regime for which the spin-flips are more strongly suppressed by the cavity (Raha et al. 2020). This can be achieved either by increasing the magnetic field which shifts the spin-flips further away from the cavity resonance or by increasing the Q-factor of the cavity. As an alternative approach, spins of the second magnetic class can be studied which show a significantly larger splitting of the spin-flip transitions compared to the spin-preserving transitions (Subsec. 5.3.4).

5.6. Spin control

In addition to initialization and readout of the spin state, coherent rotations or one-qubit gates are a fundamental requirement for quantum information protocols (Sec. 3.2). For optically addressable spin qubits, two different approaches have been studied to facilitate such gates (Reiserer 2022). The first approach is all-optical control with detuned Raman pulses (Reiserer and Rempe 2015). Such a Raman state transfer requires that the detuning between the pulses from the optical transition frequency is much larger than the spectral diffusion linewidth to avoid population in the excited state. For emitters with large spectral diffusion linewidths, this in turn demands strong optical pulses in order to facilitate π-pulses on both the spin-flip and spin-preserving transitions. So far, our studies of both the optical coherence properties and the fluorescence state detection have shown that strong pulses may induce detrimental effects to the qubit performance. In particular, strong pulses lead to optical decoherence and may cause unwanted spin flips. As an alternative, coherent rotations of the spin qubit can also be realized by directly driving the spin transition with electromagnetic fields in the microwave domain, which is investigated in this section (Wolfowicz et al. 2021).

In the following, we demonstrate the controlled transfer of the spin state by directly

applying such fields (Subsec. 5.6.1). Furthermore, the coherence properties of the spin are studied by measuring spin Rabi oscillations (Subsec. 5.6.2) and spin echos (Subsec. 5.6.3).

5.6.1. Optically detected spin transfer

To apply radiation fields in the microwave domain, the setup is extended with a copper wire mounted in the vicinity of the nanostructure above the sample within a distance of about 2 mm (App. B). This copper wire is connected with low-loss coax cables to the outside of the cryostat. Microwave pulses which create a magnetic field with a component that is perpendicular to the external guiding field are generated with an arbitrary waveform generator and amplified using a 100 W amplifier.

Since the optical frequencies of all four spin-flip and spin-preserving transitions are known, the frequency of the spin transition in the optical ground state can be directly calculated. The measurement sequence starts with the initialization of the spin by optical pumping on the spin-flip transition. Here, we initialize the spin in its dark state (Fig. 5.12 a). Then, a microwave pulse with a length of 1.1 µs is applied. When the frequency of that pulse is resonant with the spin transition, the spin population is transferred to the bright state. The latter is then probed with $N = 250$ readout pulses. Since this measurement does not intrinsically require to determine the spin state after each repetition of the experiment, the fluorescence is again averaged over many iterations.

Figure 5.12 b shows the fluorescence recorded after the optical readout pulses as a function of the frequency of the microwave pulses. The signal shows a triple peak structure at the expected resonance frequency of the spin transition and is well-fit with a model containing three Lorentzian terms which all have the same FWHM. The extracted linewidth is 2.6(1) MHz.

The spectrum consisting of three peaks is not expected for the electronic spin of a single erbium dopant. A possible explanation is that the triple peak structure may result from the coupling of the electronic spin of the erbium dopant to two nuclear spins, possibly of ^{29}Si. The hypothesis would entail that one of the two nuclear spins is about two-fold stronger coupled than the other. In this case, the amplitude of the central peak would be expected to be about two-fold larger than that of the outer peaks which agrees with the observation.

While the evidence of spin transfer is already promising, the observation of the triple peak structure and the suspected coupling of the spin to other nuclear spins may be detrimental to its performance as a spin qubit at the current setting of the external magnetic field. However, these nuclear spins may become attractive candidates for encoding a spin qubit at much larger magnetic fields where the electron spin is frozen out.

5.6.2. Spin Rabi oscillations

Next, we study the coherence of the spin transition. Similar to the investigation of the optical coherence of a single dopant, we first measure Rabi oscillations. For this

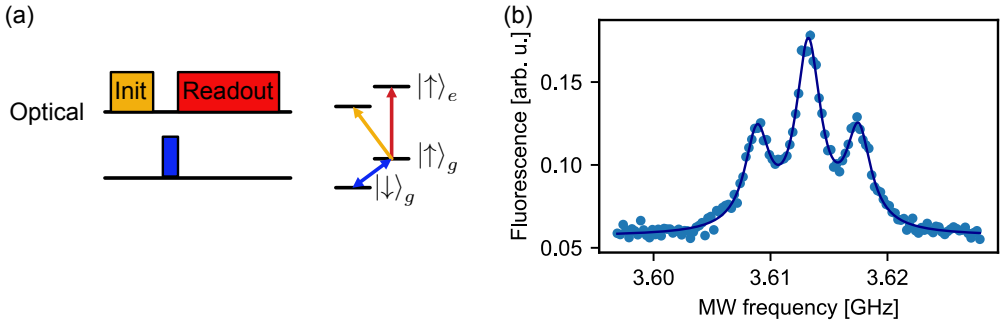

Figure 5.12.: **Direct spin transfer.** (a) Measurement scheme. The spin qubit is initialized in the dark state by pumping on the spin-flip transition (orange). Subsequently, a microwave pulse is applied which changes the population of the spin state if its frequency is on resonance with the spin transition in the optical ground state (blue). Then, the population of the bright state is probed by recording the fluorescence signal after excitation pulses resonant with the spin-preserving transition of the bright state (red). (b) Sweeping the frequency of the microwave pulse allow us to determine the transition frequency of the spin qubit. Instead of one peak, the transition is split into three which are well-fit with a model containing three Lorentzian terms which all have the same linewidth FHWM = 2.6(1) MHz (dark blue). The triple peak structure may indicate that the spin is coupled to nuclear spins in its local environment.

purpose, we change the excitation pulse area by varying the pulse length from 0.5 µs to 15 µs. Furthermore, the microwave source is tuned to the transition frequency of the central and largest of the three peaks observed in Fig. 5.12 a. In addition, the optical initialization and the readout of the spin qubit is identical to the previous subsection.

As a function of the pulse length, an oscillation of the recorded fluorescence is observed which is a clear indication of coherent spin Rabi oscillations (Fig. 5.13). The decay of this oscillations for longer pulses is attributed to decoherence of the spin state and fit with a Gaussian envelope (Suter and Álvarez 2016). Because of the triple peak structure found in the spin spectrum (Fig. 5.12 a), an additional beating on the envelope of the Rabi oscillations, resulting from the frequency detuning of the peaks, may be observed. To this end, further measurements are necessary.

In the current configuration, we find that the π-pulse length is limited to about 1.5 µs. To overcome this on future samples, gold striplines can be fabricated directly onto the chip. These striplines are then about two orders of magnitude closer to the dopants compared to the copper wire in the current configuration. Thus, we expect a significant increase of the achievable Rabi frequencies which improves the clock speed of qubit rotations..

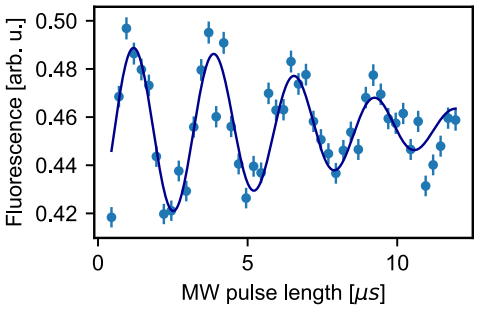

Figure 5.13.: **Spin Rabi oscillations.** After initialization of the spin in its dark state similar to Fig. 5.12, microwave pulses with varying length and resonant to the central spin transition are applied. As a function of the pulse length, an oscillation can be clearly identified which implies that the spin transition is driven coherently. The decay of the oscillations for longer pulse lengths is fitted with a Gaussian envelope and attributed to the decoherence of the spin.

5.6.3. Spin echo

The spin coherence time of the qubit encoded in the electron spin states is studied using an echo technique similar to the scheme which is applied to measure optical coherence properties (Sec. 5.4). For this purpose, the spin is again initialized by optical pumping. Then, a microwave $\pi/2$-pulse creates a coherent superposition between the spin states. After half of the sequence time $T_{\mathrm{seq}}/2$, a π-pulse is used to eliminate the effect of a static detuning between the microwave source and the spin. Subsequently, another $\pi/2$-pulse is applied to rotate the spin either back to its dark state or to the bright state depending on the relative phase of the first pulse. After the last pulse, the fluorescence is again integrated over 250 readout pulses. The datasets for the two different input phases are shown in Fig. 5.14.

The echo amplitude is then calculated by subtracting the two signals from each other and its decay is well-fit with a Gaussian (Fig. 5.14 b). From the latter, a spin coherence time of $t_2 = 48(2)\,\mu\mathrm{s}$ is extracted. Similar values for the coherence time are found for a spin qubit encoded in the electronic ground state of a single erbium dopant in $CaWO_4$ (Ourari et al. 2023). However, the measured coherence time is still significantly lower than the achieved values for spin qubits in diamond (Bernien et al. 2013; Bhaskar et al. 2020) (Tab. 5.3). Importantly, this spin coherence time excludes spin noise as the source for the optical decoherence.

The Gaussian shape of this decay indicates that the coherence time can be extended with dynamical decoupling sequences (Suter and Álvarez 2016). The performance of such sequences can be significantly improved on future samples with integrated gold striplines since microwave much shorter π-pulses with higher bandwidth will then be available.

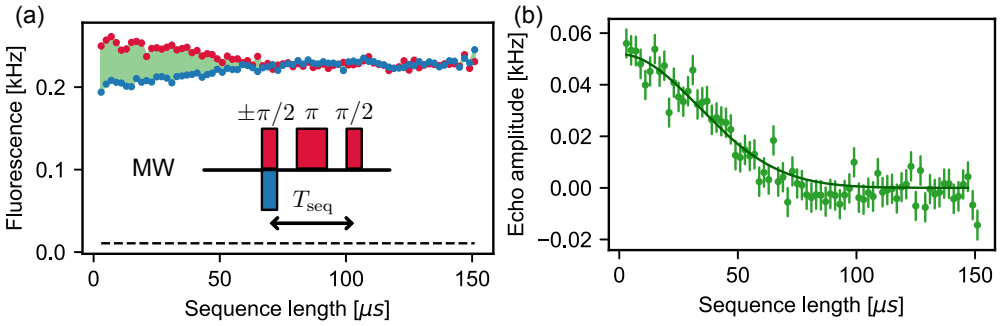

Figure 5.14.: **Spin echo sequence.** (inset) Similar to the photon measurement (Fig. 5.10), the coherence of the spin state is investigated with an echo sequence. To this end, the dark state is initialized by optical pumping. Then, microwave $\pi/2$-pulses with different phases are used to create a coherent superposition between the two spin states. Next, a π-pulse cancels the static detuning between the laser and the spin transition. Finally, another $\pi/2$-pulse is applied which, in the ideal case, rotates the spin back to either the up or the down state. (a) After the pulse sequence, the final state is read out by measuring the fluorescence on the bright state. (b) The decay of the echo amplitude, which corresponds to the difference of the fluorescence signals recorded after the two input phases, is well-fit with a Gaussian fit model. From the latter, a spin coherence time of $t_2 = 48(2)\,\mu\mathrm{s}$ is extracted.

Longer spin echo decay times may be found in isotopically purified samples in which the nuclear spins of the ^{29}Si isotope are removed if they are limiting the spin coherence. In experiments with ensembles of erbium dopants in silicon, this effect has been recently observed (Berkman et al. 2023b). In particular, electron spin coherence times of about one millisecond could be observed for two different sites in this experiment. Furthermore, in isotopically purified samples, the spin transition is not expected to split as observed in Subsec. 5.6.1 such that it might be driven more efficiently.

For quantum information processing, it is paramount that the coherence times exceeds the traveling time of the emitted photons and the subsequent classical signaling time. In particular, for a quantum network with a fiber link length of 100 km, the duration of these operations is about 0.5 ms. Thus, for the application in such networks, the coherence time of the qubit which is interfaced using the single erbium dopant must be significantly improved. This may be achieved by encoding qubits in nuclear spin states, e.g., of the ^{167}Er isotope (Rančić et al. 2018) or of neighboring ^{29}Si spins similar to what has been observed for color centers in diamond (Reiserer et al. 2016).

5.7. Summary and outlook

In summary, single erbium dopants embedded in nanophotonic silicon resonators have been investigated. In an optimized nanophotonic device, few dopants are selectively addressed using frequency-domain multiplexing. These dopants exhibit large Purcell enhancements which are only about six-fold lower than the largest reported values (Tab. 5.2). Moreover, the ratio between the spectral diffusion linewidths and the lifetime-limited linewidths obtained for these dopants is significantly smaller than the values found for erbium dopants in other host materials without inversion symmetric integration sites coupled to nanophotonic cavities (Dibos et al. 2018; Horvath et al. 2023). Furthermore, the observed ratio is comparable to the value found for erbium dopants in non-inversion symmetric sites coupled to Fabry-Perot resonators (Ulanowski, Merkel, and Reiserer 2022). In addition, this ratio is also much smaller than the values reported for color centers in silicon (Johnston et al. 2023; Higginbottom et al. 2022). The dopants studied in this chapter further emit photons with high single-photon purity.

In an external magnetic field, the electronic Zeeman levels of the emitters can be resolved and initialized such that they form an effective spin qubit. The properties of such a qubit have been further investigated. In particular, optical Rabi oscillations are observed, and photon echos recorded for the bright state of this qubit indicate that the optical coherence time approaches the lifetime-limit for sufficiently long excitation pulses. Furthermore, we demonstrated that the states of the qubit can be optically read out by fluorescence state detection, which represents to the first optical single-shot readout of spin qubit in silicon. Compared with the record values for spin qubits encoded in the electronic spin states of erbium dopants in other host materials (Ourari et al. 2023), a comparable readout speed and an approximately 10 % smaller readout fidelity are observed (Tab. 5.3). In addition, the spin transition of the qubit can be directly driven by microwave fields. On this transition, the spin exhibits coherent Rabi oscillations and spin echoes with a coherence time again comparable to erbium spins in other host materials (Ourari et al. 2023) (Tab. 5.3).

For future experiments, the nanophotonic samples may further be improved. To this end, about five-fold higher Q-factors will be targeted. Such Q-factors are still more than an order of magnitude smaller than the record Q-factor observed in silicon and is accessible with state-of-the-art nanofabrication techniques (Panuski et al. 2022). By further optimizing the design, about two-fold smaller mode volumes seem feasible. Together with implantation of erbium dopants only at the mode maximum of the resonator, a ten- to hundred-fold improvement of the Purcell factor may then be achieved. In this case, Purcell factors significantly exceeding the record values reported to date are expected. This would entail optical lifetimes ranging from 10 ns to 100 ns and hence fast optical operations, comparable to leading solid-state spin qubit platforms based on color centers in diamond (Tab. 5.3). Moreover, based on the coherence time observed in this work, such Purcell factors are likely sufficient to facilitate lifetime-limited optical coherence. In the best case, this would entail that the lifetime-limited linewidth is comparable to the currently observed spectral diffusion linewidth.

In addition, a reduction of the spectral diffusion may be targeted in future samples.

Host crystal	Cavity type	Purcell factor	Spectral diffusion linewidth [MHz]	Lifetime-limited linewidth [MHz]
Si (this work, blue dopant)	PhC	177	47	0.198
Si (this work, red dopant)	PhC	29	14	0.033
$CaWO_4$	PhC	850	0.16	0.02
MgO	PhC	1040	0.69	0.008
Y_2SiO_5	FP	120	0.2	0.002
Y_2SiO_5	PhC	650	5	0.01
Y_2O_3	FC	125	3.8	0.002

Table 5.2.: **Optical detection of single erbium dopants in different host materials.** Abbreviations: Photonic crystal cavity (PhC), Fabry-Perot cavity (FP), fiber cavity (FC). Data from: (Dibos et al. 2018; Ulanowski et al. 2023; Ourari et al. 2023; Horvath et al. 2023; Deshmukh et al. 2023).

To this end, one approach is to minimize electric stray fields. The latter are often created by charge traps and dangling bonds at the surfaces of nanostructures. Thus, dedicated surface termination might reduce this effect. Furthermore, p-i-n-diodes could be integrated into the cavities which might help to stabilize the charge environment at the position of the dopants. In addition, these p-i-n-diodes can also remove charges created during the excitation pulses, possibly on a sufficiently fast timescale to reduce the spectral diffusion. If the spectral diffusion cannot be overcome in samples with the mentioned improvements, another option is to turn to entanglement protocols which are insensitive to spectral diffusion, for example, by using high-resolution detection of the photon emission time and shelving states to compensate in real-time for the random phases resulting from the stochastic emission process (Ruskuc et al. 2023).

To study the effect of resonant or off-resonant excitation of other emitters, which may cause optical decoherence and undesired spin-flips, samples with different dopant concentration will be investigated. If a reduction of the dopant concentration leads to a significant improvement of the mentioned detrimental effects, improving the integration yield on the favorable sites, as suggested in Sec. 2.11 will be crucial for the scalability of spin qubits based on this platform.

Future samples may also significantly improve the spin properties and the spin control. To this end, isotopically purified samples will be investigated. In such samples, the coherence properties of the electron and nuclear spins and the addressing of individual spins may be significantly enhanced (Berkman et al. 2023b; Saeedi et al. 2013) compared to samples with natural abundance of all silicon isotopes. If the spin coherence time is still insufficient in such isotopically purified samples, one may turn to the nuclear spin of the ^{167}Er isotope. For the latter, excellent spin coherence properties are expected at

	Er:Si (this work)	Er:$CaWO_4$	SiV:C	NV:C
Optical emission wavelength	1537 nm	1533 nm	737 nm	637 nm
Nanophotonic cavity integration	yes	yes	yes	no
SSRO fidelity [%]	87	97	99.98	97
SSRO duration [ms]	1.24	>1.5 (*)	0.03	0.004
Spin coherence time (without dynamical decoupling) [µs]	48	44	>200	>500

Table 5.3.: **Comparison of several spin qubits encoded in the electronic spin degree of freedom.** (*) Value inferred from optical lifetime and number of readout repetitions. Data from: (Ourari et al. 2023; Bernien et al. 2013; Hensen et al. 2015; Bhaskar et al. 2020).

potential ZEFOZ points at small fields (Ortu et al. 2018) or at very large magnetic fields (Rančić et al. 2018).

Furthermore, gold striplines for directly driving the spin transition will be integrated onto the photonic chips. Thus, the distance between the dopants and the microwave antenna is reduced by about two orders of magnitude. This will lead to significantly higher spin Rabi oscillations increasing the rate at which of the qubit can be controlled. This does not only enhance the operation speed of the qubit, but also facilitates fast dynamical decoupling sequences which may in turn be used to increase the coherence time of the spin qubit (Suter and Álvarez 2016).

6. Conclusion

In this work, erbium dopants have been integrated into nanophotonic silicon structures to investigate the potential of this material platform for optical quantum technologies. Ensemble spectroscopy in nanophotonic waveguides at cryogenic temperatures reveals that erbium dopants integrate at two novel, previously unreported sites during an optimized implantation and annealing process. These sites exhibit favorable properties including narrow inhomogeneous linewidths of $< 0.5\,\mathrm{GHz}$, large crystal field splittings of $> 1.7\,\mathrm{THz}$, and exceptionally short optical lifetimes of $< 200\,\mu\mathrm{s}$ in comparison with erbium dopants in other host crystals. Furthermore, the dopants integrated at these sites show narrow homogeneous linewidths $< 0.01\,\mathrm{MHz}$ indicating promising optical coherence properties. These two sites are also found in samples that were fabricated as part of a commercial multi-wafer project run, demonstrating the compatibility of this material platform with industrial nanofabrication processes.

In addition, single emitters integrated at the novel sites are embedded in silicon photonic crystal cavities. In such devices, individual dopants are spectrally addressed using frequency-domain multiplexing and characterized. Single emitters exhibit an up to 177-fold lifetime reduction and narrow spectral diffusion linewidths of $< 15\,\mathrm{MHz}$. Furthermore, they emit single photons with high purities of $g^{(2)}(0) < 0.02$. By applying an external magnetic field, the optical spin-preserving and spin-flip transitions can be addressed individually and the properties of a spin qubit encoded in the electronic spin states of a single dopant are investigated. The optical coherence time $T_2 = 1.31(5)\,\mu\mathrm{s}$ of such a qubit approaches the lifetime-limit for sufficiently long and weak excitation pulses. Furthermore, the state of the spin qubit is read out using a fluorescence state detection scheme with a fidelity of $87.2(5)\,\%$. This represents the first reported optical single-shot readout of a spin qubit in silicon. In addition, state transfer and coherent rotations of the qubit is demonstrated by directly driving the spin transition with microwave fields. From a spin echo sequence, an electron spin coherence time of $t_2 = 48(2)\,\mu\mathrm{s}$ is obtained. Thus, the four key requirements for interference-based entanglement generation, i.e., initialization, readout and coherent rotations of the spin, and optical coherence have been demonstrated in a proof-of-principle manner. These results thus establish spin qubits based on erbium dopants as a prime candidate for optical quantum technologies in silicon.

The suggested improvements in Sec. 2.11 and Sec. 5.7 may enhance the properties of these spin qubits based on single erbium dopants such that they ultimately approach or even exceed the performance of spin qubits in diamond (Hensen et al. 2015; Bhaskar et al. 2020). In this case, the compatibility with both the most developed nanofabrication platform and existing optical glass fiber technology will provide a fundamental advantage of single erbium dopants in silicon over these previously studied spin qubits.

Single erbium dopants in silicon then offer unprecedented scaling potential for quantum communication (Reiserer 2022) and quantum computation (Simmons 2023) hardware based on solid-state spin qubits.

A. Sample preparation

The nanophotonic waveguides (Sec. 2.4, Sec. 2.3) and cavities (Sec. 4.3, Subsec. 5.2.1) used for this work are fabricated in the cleanrooms at the Zentrum für Nanotechnologie und Nanomaterialien (ZNN) at Technical University of Munich (TUM) and at the Walther-Meißner-Institut (WMI).

The nanofabrication process comprises several steps depicted in Figure A.1. Over the course of this PhD project, these steps have been regularly revised, adapted, and optimized for both performance and efficiency. In the following, the process parameters for each step are outlined 'as is' at the end of this PhD project (December 2023).

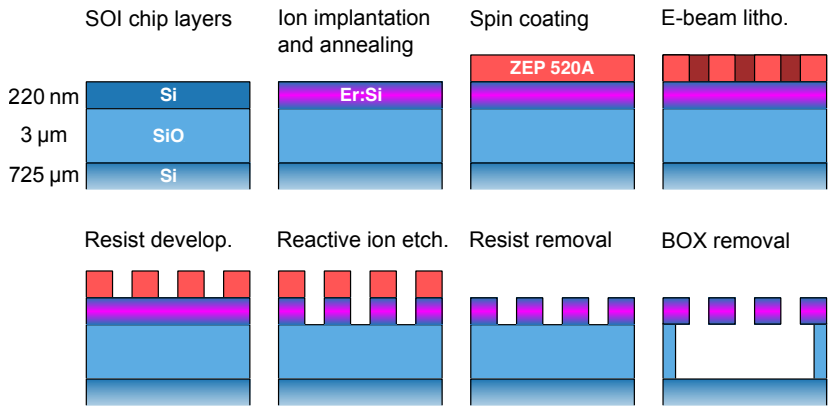

Figure A.1.: **Nanofabrication process**. Details for each step are described in the main text. Figure adapted from (Burger 2020).

Rapid thermal annealing

- Applies only to samples which were not annealed during implantation.
- Rapid thermal annealer (RTA), ADVANCE RIKO MILA-5000 series.
- Annealing conditions: chip in vacuum ($\approx 2 \times 10^{-2}$ mbar).
- Annealing recipe: Temperature rate heating: $\approx 8\,\mathrm{K\,s^{-1}}$; (typical) annealing temperature: 500 °C; hold time: 30 s; passive cooling: chip temperature below 300 °C in < 100 s.

Sample preparation

- Rinse chip: Sonicate chip for 3 min in acetone; sonicate chip for 3 min in IPA; blow dry with N_2.
- Clean surface with oxygen plasma: RF power: 400 W; oxygen flow: 75 sccm; pressure: 75 Pa for 195 s.
- Spin coat electron beam resist (ZEP-520A, ZEON Corp.) onto the sample: Speed: 4000 rpm; acceleration: 2000 rpm/s; duration: 120 s.
- Softbake resist for 180 s at 180 °C.

Electron beam lithography

- nb5 (Nanobeam Ltd.) machine at the clean room at WMI.
- Proximity correct design file (typical format: GDSII) with BEAMER (Genisys GmbH) to compensate for secondary electron scattering effects.
- Write pattern with smallest available current $\approx$ 2 nA which corresponds to the smallest possible beam size $\approx$ 2 nm. Typical base dose: 1.5 C m^{-2} to 3 C m^{-2}. Fixed accleration voltage: 80 kV.

Resist development

- Immerse and gently stir sample in cold ($\approx$ 5 °C, placed in a cold plate) n-amyl acetate for 70 s.
- Immerse and gently stir sample in cold ($\approx$ 5 °C, placed in a cold plate) methyl isobutyl ketone (MIBK) for 10 s.
- Blow dry with N_2.
- Hardbake for 180 s at 140 °C.

Reactive ion etching

- Oxford Instruments, PlasmaPro 100 Cobra ICP RIE Etch, clean room at ZNN.
- Clean the chamber with the standard oxygen plasma for 10 min.
- Cool the table on which the back wafer is mounted to −120 °C.
- Condition the chamber with the cryogenic etch recipe for 5 min.
- Mount the sample attached with thermal grease (Apiezon N) to a dummy back wafer.
- Run the cryogenic etch recipe.

- Parameters of cryogenic etch recipe: table temperature: −120 °C; chamber pressure: 7.5 mTorr; gas flows: sulfur hexafluoride (SF_6) 60 sccm, O_2 18 sccm; forward power: 15 W; ICP power: 600 W, etching time: 28 s; etch rate: $\approx 0.47\,\mu m\,min^{-1}$.

Resist stripping

- Immerse sample in warmed up (≈ 100 °C, placed in a hot plate) N,N-dimethylacetamide (ZDMAC, Zeon Corp.) for 10 min.
- Rinse chip: sonicate sample in warmed up (≈ 50 °C) N,N-dimethylacetamide for 10 min; sonicate sample in acetone for 5 min; sonicate sample in IPA for 2 min; blow dry with N_2.
- Clean surface with oxygen plasma: RF power: 400 W; oxygen flow: 75 sccm; pressure: 75 Pa for 195 s.

BOX removal

- Immerse sample in buffered oxide etch for 30 min.
- Immerse and stir sample in water (alternatively IPA) for 1 min.
- Keep sample submerged in water and transfer it to WMI.
- Submerge sample in ethanol.
- Dry sample with critical point dryer (Leica Microsystems GmbH, EM CPD300).

B. Experimental setups

For this work, a room temperature setup for characterization of the optical properties of the nanophotonic samples and a cryogenic setup for spectroscopy of erbium dopants have been built. Over the course of this PhD project, parts of these setups have been revised, adapted, and optimized. In the following, the components of both setups are presented 'as is' at the end of December 2023.

B.1. Room temperature setup

The room temperature (RT) setup (Fig. B.1) is used for characterizing the photonic properties of waveguides and cavities. It is based on a motorized three-axis XYZ stage with additional piezo actuators (Thorlabs NanoMax MAX381). On this stage, a sample with nanophotonic structures is mounted at ambient conditions. The sample can be moved relative to a fixed tip of a tapered optical fiber. To monitor this relative movement, a microscope objective (Thorlabs LMM40X-P01) and a CCD camera (Thorlabs CS165MU) are mounted above the fiber tip. A blue LED (Thorlabs M490L4) and a pellicle (Thorlabs BP145B1) are used to illuminate the fiber tip and the sample.

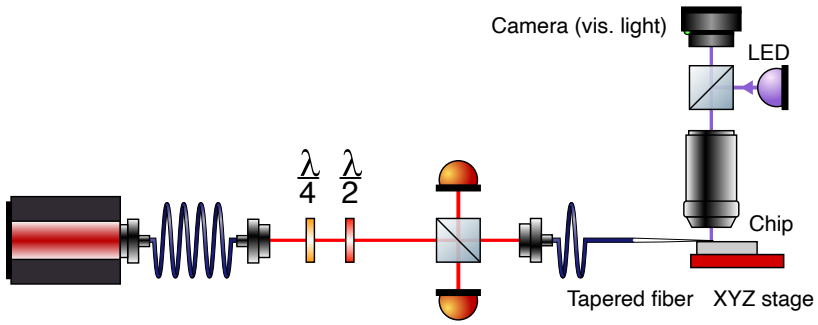

Figure B.1.: **Room temperature setup.** The photonic properties of the nanostructures are characterized with this setup prior to spectroscopic measurements at cryogenic temperatures. Light emitted by a wavelength-tunable laser is coupled to the nanostructure via a tapered fiber tip. The reflected light is then recorded by a photodiode. Further details in the text. Figure adapted from (Burger 2020).

Further, a fiber-coupled laser (Toptica CTL1500 or Toptica CTL1550) with a tuning range $> 100\,\mathrm{nm}$ is guided through a free-space setup comprising a half-wave plate and

a quarter-wave plate for polarization control and non-polarizing beamsplitter (Thorlabs BS012) with 50:50 splitting ratio. The tap output of the beamsplitter is recorded by a photodiode (PD, Thorlabs PDA10CS2) and used for normalization while the signal output is coupled into an optical fiber guiding the laser to the nanophotonic structure.

The light reflected from the nanostructure is then measured at the fourth port of the beamsplitter with a similar PD (Thorlabs PDA10CS2). The signals from both PDs are recorded with an oscilloscope (Picoscope 5000 series). To measure the wavelength-dependent reflection of the nanophotonic structures, a digital trigger sent from the laser to the oscilloscope marks the start of an internal wavelength ramp of the laser.

B.2. Cryogenic setup

For most spectroscopic measurements, the nanophotonic samples are mounted in a closed-cycle cryostat (Attocube Attodry 2100) with a base temperature of about 1.7 K in its standard configuration. The sample is thermalized by helium exchange gas. The sample temperature can be controlled with high precision between base temperature and room temperature by a variable temperature insert (VTI). In addition, the cryostat is equipped with a superconducting magnet which can apply magnetic fields of up to 9 T at the position of the sample. Alternatively, a second closed-cycle cryostat with base temperature of about 1.0 K (ICE Oxford DRY ICE 1K) is used. It is a vacuum cryostat without an exchange gas in the sample space and further equipped with a superconducting magnet which can apply magnetic fields of up to 3 T.

Cryogenic sample mount and argon gas tuning

The cryostat (Attocube Attodry 2100) is a top-loading system in which the sample is located at the end of a ≈ 1 m long stick. At the lower end of this sample stick, the sample is mounted on a stack of piezo steppers (Attocube ANPx312, ANPz 102) such that it can be aligned relative to a fixed tapered optical fiber in three dimensions. Similar to the RT-setup, the sample position is monitored with a blue LED, a pellicle, and a CCD camera outside of the sample space. Instead of an objective lens, a cryo-compatible triplet collimator (Thorlabs TC18FC-405) is mounted above the sample on the sample stick inside the sample space. As an exception, the waveguides on the FZ samples do not require nanopositioning inside the cryostat because optical fibers are glued to the waveguide facets (Sec. 2.4). Further details, including a technical drawing regarding the sample holder and the built-in microscope, can be found in (Weiß 2022).

In addition, the sample stick comprises gas lines which allow condensing argon gas onto the nanophotonic cavities to tune their resonance frequencies (Sec. 4.5). To this end, the requirement is that the sample itself is kept below the freezing point of the used gas while the tube in which the gas is guided is heated to a temperature larger than this point. This is achieved by using a copper tube thermally coupled to a resistive heater with a sufficiently small heating effect on the sample itself. Using a temperature sensor (Cernox 1030), the temperature of the copper tube is then controlled by a cryogenic

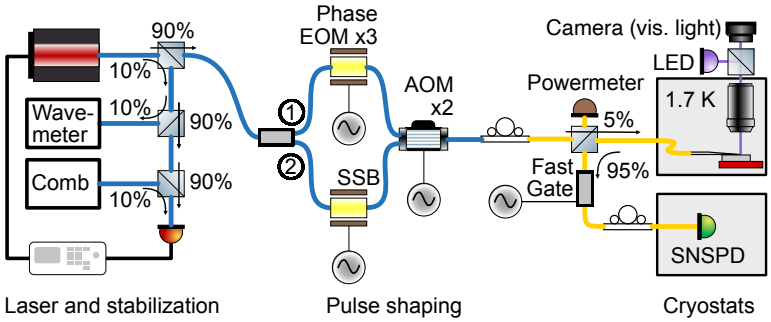

Figure B.2.: **Cryogenic measurement setup.** The light of a frequency stabilized cw laser is pulsed and modulated by acousto-optic modulators and either three electro-optic phase modulators or an optical single side-band modulator. The resulting pulses are guided via a 95:5 beam splitter to the sample which is mounted in a cryostat. The photons reflected from or emitted by the sample are then measured with superconducting nanowire single-photon detectors. PM (SM) optical fibers are colored blue (yellow). Further details are provided in the text.

temperature controller (SRS CTC100). The gas flow is controlled manually with a needle valve mounted outside of the cryostat.

Laser systems and stabilization

For optical excitation of the erbium dopants, one of the following continuous wave (cw) lasers is used: Toptica CTL1500, Toptica CTL1500, Toptica DL pro or NKT Photonics BASIK X15 'Koheras'. These laser systems are coupled to polarization maintaining fibers (Fig. B.2, blue). Further, all laser systems are phase-locked (Leibrandt and Heidecker 2015) to a frequency comb (Menlo Systems FC1500-250-ULN) with a repetition rate of 250 MHz. The comb is further stabilized to an external reference cavity (Menlo Systems ORS1500) with sub-hertz stability. In addition, the absolute wavelength of the lasers is measured with a wavemeter (Bristol 771A-NIR with 60 MHz resolution or High Finesse WS8-10 with 10 MHz resolution) sufficient to resolve individual comb teeth of the frequency comb.

Optical pulse shaping and experiment control

The light of the cw lasers is pulsed and frequency-shifted using concatenated acousto-optic modulators (AOM, Gooch&Housego Fiber-Q 300 MHz with rise time of 6 ns) (Fig. B.2). In addition to the AOMs, either a set of three concatenated electro-optic phase modulators (EOM; iXblue MPZ-LN-10/20) (Fig. B.2, 1) or a single-sideband modulation setup comprising an optical IQ modulator (iXblue MXIQER-LN-30) and a modulator bias controller (iXblue MBC-IQ-LAB-A1) (2) is used. The RF signals nec-

essary to drive these components are generated with two arbitrary waveform generators (AWGs, Zurich Instruments HDAWG and SHSFG)

After this stage, the generated pulses are further guided with single mode fibers (Fig. B.2, yellow). These fiber components are connected with low-loss connectors (Diamond E-2000 series). The polarization of the excitation pulses can be aligned to the guided modes of the nanophotonic structures with a motorized fiber polarization controller (FPC, Thorlabs MPC220). Subsequently, the pulses are sent through a fiber beam splitter fabricated of band-insensitive optical single mode fiber (Corning ClearCurve) with a splitting ratio of 95:5 (Evanescent Optics Inc.). At the 95 % port, the power of the excitation pulses is measured with a powermeter (Thorlabs PM101A). The output of the 5 % port is coupled to the sample mounted inside the cryostat.

After this beamsplitter, the light is guided to a superconducting nanowire single-photon detector (SNSPD; PhotonSpot or ID Quantique) in a second cryostat. To avoid latching of the detectors by the excitation pulses, a fast optical switch is used for gating (Agiltron Ultra-fast Dual Stage SM NS 1x1 Switch with a specified rise time of 10 ns) which is also controlled by the AWG. The voltage pulses generated by SNSPD by the impinging photons are recorded with a time-bin digitizer (Swabian Instruments TimeTagger Series 20).

Microwave control

In addition, microwave (MW) fields can be applied to the nanophotonic structures. For this purpose, MW pulses are generated (Zurich instruments SHSFG) and subsequently amplified (Mini Circuits ZHL-100W-352+, 100W). In order to apply these MW fields at the position of the sample, the pulses are guided through a ≈ 2 cm long copper wire mounted at a distance of ≈ 2 mm to the sample surface above the nanostructures. To minimize the losses inside the cryostat, a low-loss coax cable is used in between the MW input and the copper wire (Astrolab cobra-flex).

Bibliography

Acín, Antonio, Immanuel Bloch, Harry Buhrman, Tommaso Calarco, Christopher Eichler, Jens Eisert, Daniel Esteve, Nicolas Gisin, Steffen J. Glaser, Fedor Jelezko, Stefan Kuhr, Maciej Lewenstein, Max F. Riedel, Piet O. Schmidt, Rob Thew, Andreas Wallraff, Ian Walmsley, and Frank K. Wilhelm (Aug. 2018). "The Quantum Technologies Roadmap: A European Community View". In: *New Journal of Physics* 20.8, p. 080201. DOI: 10.1088/1367-2630/aad1ea.

Afzelius, Mikael, Christoph Simon, Hugues de Riedmatten, and Nicolas Gisin (May 21, 2009). "Multimode Quantum Memory Based on Atomic Frequency Combs". In: *Physical Review A* 79.5, p. 052329. DOI: 10.1103/PhysRevA.79.052329.

Akahane, Yoshihiro, Takashi Asano, Bong-Shik Song, and Susumu Noda (Oct. 2003). "High-Q Photonic Nanocavity in a Two-Dimensional Photonic Crystal". In: *Nature* 425.6961, pp. 944–947. DOI: 10.1038/nature02063.

Anderson, Christopher P., Alexandre Bourassa, Kevin C. Miao, Gary Wolfowicz, Peter J. Mintun, Alexander L. Crook, Hiroshi Abe, Jawad Ul Hassan, Nguyen T. Son, Takeshi Ohshima, and David D. Awschalom (Dec. 6, 2019). "Electrical and Optical Control of Single Spins Integrated in Scalable Semiconductor Devices". In: *Science* 366.6470, pp. 1225–1230. DOI: 10.1126/science.aax9406.

Appel, Martin Hayhurst, Alexey Tiranov, Alisa Javadi, Matthias C. Löbl, Ying Wang, Sven Scholz, Andreas D. Wieck, Arne Ludwig, Richard J. Warburton, and Peter Lodahl (Jan. 8, 2021). "Coherent Spin-Photon Interface with Waveguide Induced Cycling Transitions". In: *Physical Review Letters* 126.1, p. 013602. DOI: 10.1103/PhysRevLett.126.013602.

Arute, Frank et al. (Oct. 2019). "Quantum Supremacy Using a Programmable Superconducting Processor". In: *Nature* 574.7779, pp. 505–510. DOI: 10.1038/s41586-019-1666-5.

Asano, Takashi, Yoshiaki Ochi, Yasushi Takahashi, Katsuhiro Kishimoto, and Susumu Noda (Feb. 6, 2017). "Photonic Crystal Nanocavity with a Q Factor Exceeding Eleven Million". In: *Optics Express* 25.3, pp. 1769–1777. DOI: 10.1364/OE.25.001769.

Barrett, Sean D. and Pieter Kok (June 24, 2005). "Efficient High-Fidelity Quantum Computation Using Matter Qubits and Linear Optics". In: *Physical Review A* 71.6, p. 060310. DOI: 10.1103/PhysRevA.71.060310.

BEAMER - GenISys GmbH (2023). URL: https://www.genisys-gmbh.com/beamer.html (visited on 12/16/2023).

Becher, Christoph, Weibo Gao, Swastik Kar, Christian D. Marciniak, Thomas Monz, John G. Bartholomew, Philippe Goldner, Huanqian Loh, Elizabeth Marcellina, Kuan Eng Johnson Goh, Teck Seng Koh, Bent Weber, Zhao Mu, Jeng-Yuan Tsai, Qimin Yan, Tobias Huber-Loyola, Sven Höfling, Samuel Gyger, Stephan Steinhauer, and Val

Zwiller (Jan. 2023). "2023 Roadmap for Materials for Quantum Technologies". In: *Materials for Quantum Technology* 3.1, p. 012501. DOI: 10.1088/2633-4356/aca3f2.

Berciano, Mathias, Guillaume Marcaud, Pedro Damas, Xavier Le Roux, Paul Crozat, Carlos Alonso Ramos, Diego Pérez Galacho, Daniel Benedikovic, Delphine Marris-Morini, Eric Cassan, and Laurent Vivien (Oct. 12, 2018). "Fast Linear Electro-Optic Effect in a Centrosymmetric Semiconductor". In: *Communications Physics* 1.1 (1), pp. 1–9. DOI: 10.1038/s42005-018-0064-x.

Berkman, Ian R., Alexey Lyasota, Gabriele G. de Boo, John G. Bartholomew, Brett C. Johnson, Jeffrey C. McCallum, Bin-Bin Xu, Shouyi Xie, Rose L. Ahlefeldt, Matthew J. Sellars, Chunming Yin, and Sven Rogge (Jan. 12, 2023a). "Observing Er^{3+} Sites in Si With an In Situ Single-Photon Detector". In: *Physical Review Applied* 19.1, p. 014037. DOI: 10.1103/PhysRevApplied.19.014037.

Berkman, Ian R., Alexey Lyasota, Gabriele G. de Boo, John G. Bartholomew, Shao Q. Lim, Brett C. Johnson, Jeffrey C. McCallum, Bin-Bin Xu, Shouyi Xie, Nikolay V. Abrosimov, Hans-Joachim Pohl, Rose L. Ahlefeldt, Matthew J. Sellars, Chunming Yin, and Sven Rogge (July 19, 2023b). *Millisecond Electron Spin Coherence Time for Erbium Ions in Silicon*. DOI: 10.48550/arXiv.2307.10021. arXiv: 2307.10021 [quant-ph]. preprint.

Bernien, H., B. Hensen, W. Pfaff, G. Koolstra, M. S. Blok, L. Robledo, T. H. Taminiau, M. Markham, D. J. Twitchen, L. Childress, and R. Hanson (May 2013). "Heralded Entanglement between Solid-State Qubits Separated by Three Metres". In: *Nature* 497.7447 (7447), pp. 86–90. DOI: 10.1038/nature12016.

Bhaskar, M. K., R. Riedinger, B. Machielse, D. S. Levonian, C. T. Nguyen, E. N. Knall, H. Park, D. Englund, M. Lončar, D. D. Sukachev, and M. D. Lukin (Apr. 2020). "Experimental Demonstration of Memory-Enhanced Quantum Communication". In: *Nature* 580.7801 (7801), pp. 60–64. DOI: 10.1038/s41586-020-2103-5.

Black, Eric D. (Jan. 1, 2001). "An Introduction to Pound–Drever–Hall Laser Frequency Stabilization". In: *American Journal of Physics* 69.1, pp. 79–87. DOI: 10.1119/1.1286663.

Bloch, Immanuel, Jean Dalibard, and Sylvain Nascimbène (Apr. 2012). "Quantum Simulations with Ultracold Quantum Gases". In: *Nature Physics* 8.4, pp. 267–276. DOI: 10.1038/nphys2259.

Bogaerts, W., P. De Heyn, T. Van Vaerenbergh, K. De Vos, S. Kumar Selvaraja, T. Claes, P. Dumon, P. Bienstman, D. Van Thourhout, and R. Baets (2012). "Silicon Microring Resonators". In: *Laser & Photonics Reviews* 6.1, pp. 47–73. DOI: 10.1002/lpor.201100017.

Bopp, Julian M., Matthias Plock, Tim Turan, Gregor Pieplow, Sven Burger, and Tim Schröder (Oct. 10, 2022). *'Sawfish' Photonic Crystal Cavity for Near-Unity Emitter-to-Fiber Interfacing in Quantum Network Applications*. DOI: 10.48550/arXiv.2210.04702. arXiv: 2210.04702 [physics, physics:quant-ph]. preprint.

Borregaard, Johannes, Anders Søndberg Sørensen, and Peter Lodahl (2019). "Quantum Networks with Deterministic Spin–Photon Interfaces". In: *Advanced Quantum Technologies* 2.5-6, p. 1800091. DOI: 10.1002/qute.201800091.

Böttger, Thomas, C. W. Thiel, Y. Sun, and R. L. Cone (Feb. 1, 2006). "Optical Decoherence and Spectral Diffusion at 1.5 μm in $Er^{3+} : Y_2SiO_5$ versus Magnetic Field, Temperature, and Er^{3+} Concentration". In: *Physical Review B* 73.7, p. 075101. DOI: 10.1103/PhysRevB.73.075101.

Burek, Michael J., Charles Meuwly, Ruffin E. Evans, Mihir K. Bhaskar, Alp Sipahigil, Srujan Meesala, Bartholomeus Machielse, Denis D. Sukachev, Christian T. Nguyen, Jose L. Pacheco, Edward Bielejec, Mikhail D. Lukin, and Marko Lončar (Aug. 25, 2017). "Fiber-Coupled Diamond Quantum Nanophotonic Interface". In: *Physical Review Applied* 8.2. DOI: 10.1103/PhysRevApplied.8.024026.

Burger, Florian (May 14, 2020). "Silicon Photonic-Crystal Waveguides for Broadband Purcell Enhancement of Erbium Emission".

Burgers, A. P., L. S. Peng, J. A. Muniz, A. C. McClung, M. J. Martin, and H. J. Kimble (Jan. 8, 2019). "Clocked Atom Delivery to a Photonic Crystal Waveguide". In: *Proceedings of the National Academy of Sciences* 116.2, pp. 456–465. DOI: 10.1073/pnas.1817249115.

Car, B., J.-L. Le Gouët, and T. Chanelière (Sept. 10, 2020). "Superhyperfine Induced Photon-Echo Collapse of Erbium in Y_2SiO_5". In: *Physical Review B* 102.11, p. 115119. DOI: 10.1103/PhysRevB.102.115119.

Car, B., L. Veissier, A. Louchet-Chauvet, J.-L. Le Gouët, and T. Chanelière (Oct. 4, 2019). "Optical Study of the Anisotropic Erbium Spin Flip-Flop Dynamics". In: *Physical Review B* 100.16, p. 165107. DOI: 10.1103/PhysRevB.100.165107.

Casabone, Bernardo, Chetan Deshmukh, Shuping Liu, Diana Serrano, Alban Ferrier, Thomas Hümmer, Philippe Goldner, David Hunger, and Hugues de Riedmatten (June 11, 2021). "Dynamic Control of Purcell Enhanced Emission of Erbium Ions in Nanoparticles". In: *Nature Communications* 12.1 (1), p. 3570. DOI: 10.1038/s41467-021-23632-9.

Chan, Jasper, Amir H. Safavi-Naeini, Jeff T. Hill, Seán Meenehan, and Oskar Painter (Aug. 23, 2012). "Optimized Optomechanical Crystal Cavity with Acoustic Radiation Shield". In: *Applied Physics Letters* 101.8, p. 081115. DOI: 10.1063/1.4747726.

Cova Fariña, Pablo, Benjamin Merkel, Natalia Herrera Valencia, Penghong Yu, Alexander Ulanowski, and Andreas Reiserer (June 11, 2021). "Coherent Control in the Ground and Optically Excited States of an Ensemble of Erbium Dopants". In: *Physical Review Applied* 15.6, p. 064028. DOI: 10.1103/PhysRevApplied.15.064028.

Daley, Andrew J., Immanuel Bloch, Christian Kokail, Stuart Flannigan, Natalie Pearson, Matthias Troyer, and Peter Zoller (July 2022). "Practical Quantum Advantage in Quantum Simulation". In: *Nature* 607.7920 (7920), pp. 667–676. DOI: 10.1038/s41586-022-04940-6.

Dantec, Marianne Le, Miloš Rančić, Sen Lin, Eric Billaud, Vishal Ranjan, Daniel Flanigan, Sylvain Bertaina, Thierry Chanelière, Philippe Goldner, Andreas Erb, Ren Bao Liu, Daniel Estève, Denis Vion, Emmanuel Flurin, and Patrice Bertet (June 28, 2021). "Twenty-Three Millisecond Electron Spin Coherence of Erbium Ions in a Natural-Abundance Crystal". arXiv: 2106.14974 [cond-mat, physics:quant-ph].

De Boer, M.J., J.G.E. Gardeniers, H.V. Jansen, E. Smulders, M.-J. Gilde, G. Roelofs, J.N. Sasserath, and M. Elwenspoek (Aug. 2002). "Guidelines for Etching Silicon

MEMS Structures Using Fluorine High-Density Plasmas at Cryogenic Temperatures". In: *Journal of Microelectromechanical Systems* 11.4, pp. 385–401. DOI: 10.1109/JMEMS.2002.800928.

Degen, C. L., F. Reinhard, and P. Cappellaro (July 25, 2017). "Quantum Sensing". In: *Reviews of Modern Physics* 89.3, p. 035002. DOI: 10.1103/RevModPhys.89.035002.

De Leon, Nathalie P., Kohei M. Itoh, Dohun Kim, Karan K. Mehta, Tracy E. Northup, Hanhee Paik, B. S. Palmer, N. Samarth, Sorawis Sangtawesin, and D. W. Steuerman (Apr. 16, 2021). "Materials Challenges and Opportunities for Quantum Computing Hardware". In: *Science* 372.6539, eabb2823. DOI: 10.1126/science.abb2823.

Deotare, Parag B., Irfan Bulu, Ian W. Frank, Qimin Quan, Yinan Zhang, Rob Ilic, and Marko Loncar (May 22, 2012). "All Optical Reconfiguration of Optomechanical Filters". In: *Nature Communications* 3.1 (1), p. 846. DOI: 10.1038/ncomms1830.

Deshmukh, Chetan, Eduardo Beattie, Bernardo Casabone, Samuele Grandi, Diana Serrano, Alban Ferrier, Philippe Goldner, David Hunger, and Hugues de Riedmatten (Oct. 20, 2023). "Detection of Single Ions in a Nanoparticle Coupled to a Fiber Cavity". In: *Optica* 10.10, pp. 1339–1344. DOI: 10.1364/OPTICA.491692.

De Vries, Pedro and Ad Lagendijk (Aug. 17, 1998). "Resonant Scattering and Spontaneous Emission in Dielectrics: Microscopic Derivation of Local-Field Effects". In: *Physical Review Letters* 81.7, pp. 1381–1384. DOI: 10.1103/PhysRevLett.81.1381.

Dibos, A. M., M. Raha, C. M. Phenicie, and J. D. Thompson (June 11, 2018). "Atomic Source of Single Photons in the Telecom Band". In: *Physical Review Letters* 120.24. DOI: 10.1103/PhysRevLett.120.243601.

DiVincenzo, David P. (2000). "The Physical Implementation of Quantum Computation". In: *Fortschritte der Physik* 48.9-11, pp. 771–783. DOI: 10.1002/1521-3978(200009)48:9/11<771::AID-PROP771>3.0.CO;2-E.

Dodson, Christopher M. and Rashid Zia (Sept. 5, 2012). "Magnetic Dipole and Electric Quadrupole Transitions in the Trivalent Lanthanide Series: Calculated Emission Rates and Oscillator Strengths". In: *Physical Review B* 86.12, p. 125102. DOI: 10.1103/PhysRevB.86.125102.

Dussart, R., T. Tillocher, P. Lefaucheux, and M. Boufnichel (2014). "Plasma Cryogenic Etching of Silicon: From the Early Days to Today's Advanced Technologies". In: *Journal of Physics D: Applied Physics* 47.12, p. 123001. DOI: 10.1088/0022-3727/47/12/123001.

Englund, Dirk, Ilya Fushman, and Jelena Vuckovic (Aug. 8, 2005). "General Recipe for Designing Photonic Crystal Cavities". In: *Optics Express* 13.16, pp. 5961–5975. DOI: 10.1364/OPEX.13.005961.

Fox, Mark (2006). *Quantum Optics: An Introduction*. Oxford Master Series in Physics 15. Oxford ; New York: Oxford University Press. 378 pp.

Früh, Johannes (June 17, 2020). "Optimization of the Coupling to Photonic Crystal Resonators". MA thesis.

Fukumori, Rikuto, Yizhong Huang, Jun Yang, Haitao Zhang, and Tian Zhong (June 8, 2020). "Subkilohertz Optical Homogeneous Linewidth and Dephasing Mechanisms in Er^{3+}:Y_2O_3 Ceramics". In: *Physical Review B* 101.21, p. 214202. DOI: 10.1103/PhysRevB.101.214202.

Georgescu, I. M., S. Ashhab, and Franco Nori (Mar. 10, 2014). "Quantum Simulation". In: *Reviews of Modern Physics* 86.1, pp. 153–185. DOI: 10.1103/RevModPhys.86.153.

Gisin, Nicolas and Rob Thew (Mar. 2007). "Quantum Communication". In: *Nature Photonics* 1.3, pp. 165–171. DOI: 10.1038/nphoton.2007.22.

Gritsch, Andreas, Alexander Ulanowski, and Andreas Reiserer (June 20, 2023). "Purcell Enhancement of Single-Photon Emitters in Silicon". In: *Optica* 10.6, pp. 783–789. DOI: 10.1364/OPTICA.486167.

Gritsch, Andreas, Lorenz Weiss, Johannes Früh, Stephan Rinner, and Andreas Reiserer (Oct. 25, 2022). "Narrow Optical Transitions in Erbium-Implanted Silicon Waveguides". In: *Physical Review X* 12.4, p. 041009. DOI: 10.1103/PhysRevX.12.041009.

Gross, Rudolf and Achim Marx (Jan. 9, 2018). *Festkörperphysik*. De Gruyter. DOI: 10.1515/9783110559187.

Guimbao, J., L. Sanchis, L. Weituschat, J. Manuel Llorens, M. Song, J. Cardenas, and P. Aitor Postigo (June 15, 2022). "Numerical Optimization of a Nanophotonic Cavity by Machine Learning for Near-Unity Photon Indistinguishability at Room Temperature". In: *ACS Photonics* 9.6, pp. 1926–1935. DOI: 10.1021/acsphotonics.1c01651.

Ha, N. N., K. Dohnalová, T. Gregorkiewicz, and J. Valenta (May 13, 2010). "Optical Gain of the 1.54 μm<script> emission in MBE-grown Si:Er nanolayers". In: *Physical Review B* 81.19, p. 195206. DOI: 10.1103/PhysRevB.81.195206.

Hensen, B., H. Bernien, A. E. Dréau, A. Reiserer, N. Kalb, M. S. Blok, J. Ruitenberg, R. F. L. Vermeulen, R. N. Schouten, C. Abellán, W. Amaya, V. Pruneri, M. W. Mitchell, M. Markham, D. J. Twitchen, D. Elkouss, S. Wehner, T. H. Taminiau, and R. Hanson (Oct. 2015). "Loophole-Free Bell Inequality Violation Using Electron Spins Separated by 1.3 Kilometres". In: *Nature* 526.7575, pp. 682–686. DOI: 10.1038/nature15759.

Higginbottom, Daniel B., Alexander T. K. Kurkjian, Camille Chartrand, Moein Kazemi, Nicholas A. Brunelle, Evan R. MacQuarrie, James R. Klein, Nicholas R. Lee-Hone, Jakub Stacho, Myles Ruether, Camille Bowness, Laurent Bergeron, Adam DeAbreu, Stephen R. Harrigan, Joshua Kanaganayagam, Danica W. Marsden, Timothy S. Richards, Leea A. Stott, Sjoerd Roorda, Kevin J. Morse, Michael L. W. Thewalt, and Stephanie Simmons (July 2022). "Optical Observation of Single Spins in Silicon". In: *Nature* 607.7918 (7918), pp. 266–270. DOI: 10.1038/s41586-022-04821-y.

Hollenbach, Michael, Nico Klingner, Nagesh S. Jagtap, Lothar Bischoff, Ciarán Fowley, Ulrich Kentsch, Gregor Hlawacek, Artur Erbe, Nikolay V. Abrosimov, Manfred Helm, Yonder Berencén, and Georgy V. Astakhov (Dec. 12, 2022). "Wafer-Scale Nanofabrication of Telecom Single-Photon Emitters in Silicon". In: *Nature Communications* 13.1 (1), p. 7683. DOI: 10.1038/s41467-022-35051-5.

Horvath, Sebastian P., Christopher M. Phenicie, Salim Ourari, Mehmet T. Uysal, Songtao Chen, Łukasz Dusanowski, Mouktik Raha, Paul Stevenson, Adam T. Turflinger, Robert J. Cava, Nathalie P. de Leon, and Jeff D. Thompson (July 6, 2023). *Strong Purcell Enhancement of an Optical Magnetic Dipole Transition*. DOI: 10.48550/arXiv.2307.03022. arXiv: 2307.03022 [physics, physics:quant-ph]. preprint.

Hu, Shuren, Marwan Khater, Rafael Salas-Montiel, Ernst Kratschmer, Sebastian Engelmann, William M. J. Green, and Sharon M. Weiss (Aug. 2018). "Experimental

Realization of Deep-Subwavelength Confinement in Dielectric Optical Resonators". In: *Science Advances* 4.8, eaat2355. DOI: 10.1126/sciadv.aat2355.

Hunger, D., C. Deutsch, R. J. Barbour, R. J. Warburton, and J. Reichel (Jan. 13, 2012). "Laser Micro-Fabrication of Concave, Low-Roughness Features in Silica". In: *AIP Advances* 2.1, p. 012119. DOI: 10.1063/1.3679721.

Hunger, D., T. Steinmetz, Y. Colombe, C. Deutsch, T. W. Hänsch, and J. Reichel (June 2010). "A Fiber Fabry–Perot Cavity with High Finesse". In: *New Journal of Physics* 12.6, p. 065038. DOI: 10.1088/1367-2630/12/6/065038.

Islam, Fariba, Chang-Min Lee, Samuel Harper, Mohammad Habibur Rahaman, Yuqi Zhao, Neelesh Kumar Vij, and Edo Waks (Oct. 20, 2023). *Cavity Enhanced Emission from a Silicon T Center*. DOI: 10.48550/arXiv.2310.13808. arXiv: 2310.13808 [physics, physics:quant-ph]. preprint.

Jacobs, S. F. (Mar. 1, 1988). "Optical Heterodyne (Coherent) Detection". In: *American Journal of Physics* 56.3, pp. 235–245. DOI: 10.1119/1.15655.

Jakiela, R., A. Barcz, J. Sarnecki, and G.k. Celler (2018). "Ultrahigh Sensitivity SIMS Analysis of Oxygen in Silicon". In: *Surface and Interface Analysis* 50.7, pp. 729–733. DOI: 10.1002/sia.6467.

Janitz, Erika, Mihir K. Bhaskar, and Lilian Childress (Oct. 20, 2020). "Cavity Quantum Electrodynamics with Color Centers in Diamond". In: *Optica* 7.10, pp. 1232–1252. DOI: 10.1364/OPTICA.398628.

Joannopoulos, J. D., ed. (2008). *Photonic Crystals: Molding the Flow of Light*. 2nd ed. Princeton: Princeton University Press. 286 pp.

Johnston, Adam, Ulises Felix-Rendon, Yu-En Wong, and Songtao Chen (Oct. 30, 2023). *Cavity-Coupled Telecom Atomic Source in Silicon*. DOI: 10.48550/arXiv.2310.20014. arXiv: 2310.20014 [physics, physics:quant-ph]. preprint.

Kenyon, A. J. (Nov. 2005). "Erbium in Silicon". In: *Semiconductor Science and Technology* 20.12, R65. DOI: 10.1088/0268-1242/20/12/R02.

Kimble, H. J. (June 2008). "The Quantum Internet". In: *Nature* 453.7198, pp. 1023–1030. DOI: 10.1038/nature07127.

Kindem, Jonathan M., Andrei Ruskuc, John G. Bartholomew, Jake Rochman, Yan Qi Huan, and Andrei Faraon (Apr. 2020). "Control and Single-Shot Readout of an Ion Embedded in a Nanophotonic Cavity". In: *Nature* 580.7802 (7802), pp. 201–204. DOI: 10.1038/s41586-020-2160-9.

Knall, E. N., C. M. Knaut, R. Bekenstein, D. R. Assumpcao, P. L. Stroganov, W. Gong, Y. Q. Huan, P.-J. Stas, B. Machielse, M. Chalupnik, D. Levonian, A. Suleymanzade, R. Riedinger, H. Park, M. Lončar, M. K. Bhaskar, and M. D. Lukin (July 26, 2022). "Efficient Source of Shaped Single Photons Based on an Integrated Diamond Nanophotonic System". In: *Physical Review Letters* 129.5, p. 053603. DOI: 10.1103/PhysRevLett.129.053603.

Komza, Lukasz, Polnop Samutpraphoot, Mutasem Odeh, Yu-Lung Tang, Milena Mathew, Jiu Chang, Hanbin Song, Myung-Ki Kim, Yihuang Xiong, Geoffroy Hautier, and Alp Sipahigil (Nov. 16, 2022). *Indistinguishable Photons from an Artificial Atom in Silicon Photonics*. DOI: 10.48550/arXiv.2211.09305. arXiv: 2211.09305 [cond-mat, physics:physics, physics:quant-ph]. preprint.

Krutyanskiy, V., M. Canteri, M. Meraner, V. Krcmarsky, and B. P. Lanyon (Aug. 17, 2023). *Multimode Ion-Photon Entanglement over 101 Kilometers of Optical Fiber*. DOI: 10.48550/arXiv.2308.08891. arXiv: 2308.08891 [quant-ph]. preprint.

Kuhlmann, Andreas V., Julien Houel, Arne Ludwig, Lukas Greuter, Dirk Reuter, Andreas D. Wieck, Martino Poggio, and Richard J. Warburton (Sept. 2013). "Charge Noise and Spin Noise in a Semiconductor Quantum Device". In: *Nature Physics* 9.9 (9), pp. 570–575. DOI: 10.1038/nphys2688.

Leibrandt, D. R. and J. Heidecker (Dec. 30, 2015). "An Open Source Digital Servo for Atomic, Molecular, and Optical Physics Experiments". In: *Review of Scientific Instruments* 86.12, p. 123115. DOI: 10.1063/1.4938282.

Li, H. H. (July 1, 1980). "Refractive Index of Silicon and Germanium and Its Wavelength and Temperature Derivatives". In: *Journal of Physical and Chemical Reference Data* 9.3, pp. 561–658. DOI: 10.1063/1.555624.

Li, Pei-Yun, Jian-Yin Huang, Tian-Xiang Zhu, Chao Liu, Duan-Cheng Liu, Zong-Quan Zhou, Chuan-Feng Li, and Guang-Can Guo (Sept. 1, 2020). "Optical Spectroscopy and Coherent Dynamics of 167Er3 : YVO4 at 1.5 m below 1 K". In: *Journal of Luminescence* 225, p. 117344. DOI: 10.1016/j.jlumin.2020.117344.

Liu, Guokui and Bernard Jacquier, eds. (2005). *Spectroscopic Properties of Rare Earths in Optical Materials*. Springer Series in Materials Science 83. Berlin ; New York: Springer. 550 pp.

Liu, Yujia, Stephan Rinner, Thilo Remmele, Owen Ernst, Andreas Reiserer, and Torsten Boeck (Sept. 1, 2022). "28Silicon-on-insulator for Optically Interfaced Quantum Emitters". In: *Journal of Crystal Growth* 593, p. 126733. DOI: 10.1016/j.jcrysgro.2022.126733.

Lodahl, Peter, Sahand Mahmoodian, and Søren Stobbe (May 11, 2015). "Interfacing Single Photons and Single Quantum Dots with Photonic Nanostructures". In: *Reviews of Modern Physics* 87.2, pp. 347–400. DOI: 10.1103/RevModPhys.87.347.

Louchet-Chauvet, A., P. Verlot, J.-P. Poizat, and T. Chanelière (Nov. 1, 2023). "Piezo-Orbital Backaction Force in a Rare-Earth-Doped Crystal". In: *Physical Review Applied* 20.5, p. 054004. DOI: 10.1103/PhysRevApplied.20.054004.

Lu, Chao-Yang, Yuan Cao, Cheng-Zhi Peng, and Jian-Wei Pan (July 6, 2022). "Micius Quantum Experiments in Space". In: *Reviews of Modern Physics* 94.3, p. 035001. DOI: 10.1103/RevModPhys.94.035001.

Macfarlane, Roger M (Dec. 2002). "High-Resolution Laser Spectroscopy of Rare-Earth Doped Insulators: A Personal Perspective". In: *Journal of Luminescence* 100.1-4, pp. 1–20. DOI: 10.1016/S0022-2313(02)00450-7.

Mądzik, Mateusz T., Serwan Asaad, Akram Youssry, Benjamin Joecker, Kenneth M. Rudinger, Erik Nielsen, Kevin C. Young, Timothy J. Proctor, Andrew D. Baczewski, Arne Laucht, Vivien Schmitt, Fay E. Hudson, Kohei M. Itoh, Alexander M. Jakob, Brett C. Johnson, David N. Jamieson, Andrew S. Dzurak, Christopher Ferrie, Robin Blume-Kohout, and Andrea Morello (Jan. 2022). "Precision Tomography of a Three-Qubit Donor Quantum Processor in Silicon". In: *Nature* 601.7893 (7893), pp. 348–353. DOI: 10.1038/s41586-021-04292-7.

Maryasov, Alexander G. and Michael K. Bowman (Aug. 1, 2012). "Spin Dynamics of Paramagnetic Centers with Anisotropic g Tensor and Spin of 1/2". In: *Journal of Magnetic Resonance* 221, pp. 69–75. DOI: 10.1016/j.jmr.2012.05.011.

Merkel, Benjamin (2021). "Enhancing the Emission and Coherence of Erbium Dopants". Technische Universität München.

Merkel, Benjamin, Pablo Cova Fariña, and Andreas Reiserer (July 16, 2021). "Dynamical Decoupling of Spin Ensembles with Strong Anisotropic Interactions". In: *Physical Review Letters* 127.3, p. 030501. DOI: 10.1103/PhysRevLett.127.030501.

Merkel, Benjamin, Alexander Ulanowski, and Andreas Reiserer (Nov. 4, 2020). "Coherent and Purcell-Enhanced Emission from Erbium Dopants in a Cryogenic High-Q Resonator". In: *Physical Review X* 10.4, p. 041025. DOI: 10.1103/PhysRevX.10.041025.

Moehring, D. L., P. Maunz, S. Olmschenk, K. C. Younge, D. N. Matsukevich, L.-M. Duan, and C. Monroe (Sept. 2007). "Entanglement of Single-Atom Quantum Bits at a Distance". In: *Nature* 449.7158 (7158), pp. 68–71. DOI: 10.1038/nature06118.

Molesky, Sean, Zin Lin, Alexander Y. Piggott, Weiliang Jin, Jelena Vucković, and Alejandro W. Rodriguez (Nov. 2018). "Inverse Design in Nanophotonics". In: *Nature Photonics* 12.11 (11), pp. 659–670. DOI: 10.1038/s41566-018-0246-9.

Mosor, S., J. Hendrickson, B. C. Richards, J. Sweet, G. Khitrova, H. M. Gibbs, T. Yoshie, A. Scherer, O. B. Shchekin, and D. G. Deppe (Sept. 28, 2005). "Scanning a Photonic Crystal Slab Nanocavity by Condensation of Xenon". In: *Applied Physics Letters* 87.14, p. 141105. DOI: 10.1063/1.2076435.

Muiznieks, Andris, Janis Virbulis, Anke Lüdge, Helge Riemann, and Nico Werner (2015). "Floating Zone Growth of Silicon". In: *Handbook of Crystal Growth*. Elsevier, pp. 241–279. DOI: 10.1016/B978-0-444-63303-3.00007-9.

Nakamura, Tatsuya, Yasushi Takahashi, Yoshinori Tanaka, Takashi Asano, and Susumu Noda (May 2, 2016). "Improvement in the Quality Factors for Photonic Crystal Nanocavities via Visualization of the Leaky Components". In: *Optics Express* 24.9, pp. 9541–9549. DOI: 10.1364/OE.24.009541.

Nguyen, C. T., D. D. Sukachev, M. K. Bhaskar, B. Machielse, D. S. Levonian, E. N. Knall, P. Stroganov, C. Chia, M. J. Burek, R. Riedinger, H. Park, M. Lončar, and M. D. Lukin (Oct. 30, 2019). "An Integrated Nanophotonic Quantum Register Based on Silicon-Vacancy Spins in Diamond". In: *Physical Review B* 100.16, p. 165428. DOI: 10.1103/PhysRevB.100.165428.

Nikbakht, H., H. Latifi, M. Oraie, and T. Amini (Dec. 2015). "Fabrication of Tapered Tip Fibers With a Controllable Cone Angle Using Dynamical Etching". In: *Journal of Lightwave Technology* 33.23, pp. 4707–4711. DOI: 10.1109/JLT.2015.2453365.

Nobel Prize Outreach AB (Oct. 4, 2022). *The Nobel Prize in Physics 2022*. NobelPrize.org. URL: https://www.nobelprize.org/prizes/physics/2022/summary/ (visited on 07/01/2023).

Noiri, Akito, Kenta Takeda, Takashi Nakajima, Takashi Kobayashi, Amir Sammak, Giordano Scappucci, and Seigo Tarucha (Jan. 2022). "Fast Universal Quantum Gate above the Fault-Tolerance Threshold in Silicon". In: *Nature* 601.7893 (7893), pp. 338–342. DOI: 10.1038/s41586-021-04182-y.

Nojiri, Kazuo (2015). *Dry Etching Technology for Semiconductors*. Cham: Springer International Publishing. DOI: 10.1007/978-3-319-10295-5.

Ocola, L. E. and A. Stein (Nov. 30, 2006). "Effect of Cold Development on Improvement in Electron-Beam Nanopatterning Resolution and Line Roughness". In: *Journal of Vacuum Science & Technology B: Microelectronics and Nanometer Structures Processing, Measurement, and Phenomena* 24.6, pp. 3061–3065. DOI: 10.1116/1.2366698.

Orbach, R. : and Brebis Bleaney (Jan. 1997). "Spin-Lattice Relaxation in Rare-Earth Salts". In: *Proceedings of the Royal Society of London. Series A. Mathematical and Physical Sciences* 264.1319, pp. 458–484. DOI: 10.1098/rspa.1961.0211.

Ortu, Antonio, Alexey Tiranov, Sacha Welinski, Florian Fröwis, Nicolas Gisin, Alban Ferrier, Philippe Goldner, and Mikael Afzelius (Aug. 2018). "Simultaneous Coherence Enhancement of Optical and Microwave Transitions in Solid-State Electronic Spins". In: *Nature Materials* 17.8, p. 671. DOI: 10.1038/s41563-018-0138-x.

Oskooi, Ardavan F., David Roundy, Mihai Ibanescu, Peter Bermel, J.D. Joannopoulos, and Steven G. Johnson (Mar. 2010). "Meep: A Flexible Free-Software Package for Electromagnetic Simulations by the FDTD Method". In: *Computer Physics Communications* 181.3, pp. 687–702. DOI: 10.1016/j.cpc.2009.11.008.

Ouaddah, Hadjer, Isabelle Périchaud, Damien Barakel, Olivier Palais, Marisa Di Sabatino, Guillaume Reinhart, Gabrielle Regula, and Nathalie Mangelinck-Noël (Sept. 2019). "Role of Impurities in Silicon Solidification and Electrical Properties Studied by Complementary In Situ and Ex Situ Methods". In: *physica status solidi (a)* 216.17, p. 1900298. DOI: 10.1002/pssa.201900298.

Ourari, Salim, Łukasz Dusanowski, Sebastian P. Horvath, Mehmet T. Uysal, Christopher M. Phenicie, Paul Stevenson, Mouktik Raha, Songtao Chen, Robert J. Cava, Nathalie P. de Leon, and Jeff D. Thompson (Aug. 2023). "Indistinguishable Telecom Band Photons from a Single Er Ion in the Solid State". In: *Nature* 620.7976 (7976), pp. 977–981. DOI: 10.1038/s41586-023-06281-4.

Palmetshofer, L., M. Gritsch, and G. Hobler (Apr. 24, 2001). "Range of Ion-Implanted Rare Earth Elements in Si and SiO2". In: *Materials Science and Engineering: B* 81.1, pp. 83–85. DOI: 10.1016/S0921-5107(00)00742-X.

Panuski, Christopher L., Ian Christen, Momchil Minkov, Cole J. Brabec, Sivan Trajtenberg-Mills, Alexander D. Griffiths, Jonathan J. D. McKendry, Gerald L. Leake, Daniel J. Coleman, Cung Tran, Jeffrey St Louis, John Mucci, Cameron Horvath, Jocelyn N. Westwood-Bachman, Stefan F. Preble, Martin D. Dawson, Michael J. Strain, Michael L. Fanto, and Dirk R. Englund (Dec. 2022). "A Full Degree-of-Freedom Spatiotemporal Light Modulator". In: *Nature Photonics* 16.12 (12), pp. 834–842. DOI: 10.1038/s41566-022-01086-9.

Pforr, Jakob Michael (May 16, 2023). "Nanophotonic Resonators for Efficient Light Matter Coupling".

Phenicie, Christopher (2021). "Devices and Materials for Quantum Network Nodes Based on Rare Earth Ions". In.

Phenicie, Christopher M., Paul Stevenson, Sacha Welinski, Brendon C. Rose, Abraham T. Asfaw, Robert J. Cava, Stephen A. Lyon, Nathalie P. de Leon, and Jeff D. Thomp-

son (Dec. 11, 2019). “Narrow Optical Line Widths in Erbium Implanted in TiO2”. In: *Nano Letters* 19.12, pp. 8928–8933. DOI: 10.1021/acs.nanolett.9b03831.

Philips, Stephan G. J., Mateusz T. Mądzik, Sergey V. Amitonov, Sander L. de Snoo, Maximilian Russ, Nima Kalhor, Christian Volk, William I. L. Lawrie, Delphine Brousse, Larysa Tryputen, Brian Paquelet Wuetz, Amir Sammak, Menno Veldhorst, Giordano Scappucci, and Lieven M. K. Vandersypen (Sept. 2022). “Universal Control of a Six-Qubit Quantum Processor in Silicon”. In: *Nature* 609.7929 (7929), pp. 919–924. DOI: 10.1038/s41586-022-05117-x.

Polman, A. (July 1, 1997). “Erbium Implanted Thin Film Photonic Materials”. In: *Journal of Applied Physics* 82.1, pp. 1–39. DOI: 10.1063/1.366265.

Powell, O. (Oct. 2002). “Single-Mode Condition for Silicon Rib Waveguides”. In: *Journal of Lightwave Technology* 20.10, pp. 1851–1855. DOI: 10.1109/JLT.2002.804036.

Pregnolato, Tommaso, Marco E. Stucki, Julian M. Bopp, Maarten H. v d Hoeven, Alok Gokhale, Olaf Krüger, and Tim Schröder (Nov. 6, 2023). *Fabrication of Sawfish Photonic Crystal Cavities in Bulk Diamond*. DOI: 10.48550/arXiv.2311.03618. arXiv: 2311.03618 [physics, physics:quant-ph]. preprint.

Preskill, John (Aug. 6, 2018). “Quantum Computing in the NISQ Era and Beyond”. In: *Quantum* 2, p. 79. DOI: 10.22331/q-2018-08-06-79.

Priolo, Francesco, Giorgia Franzò, Salvatore Coffa, and Alberto Carnera (Feb. 15, 1998). “Excitation and Nonradiative Deexcitation Processes of Er^{3+} in Crystalline Si”. In: *Physical Review B* 57.8, pp. 4443–4455. DOI: 10.1103/PhysRevB.57.4443.

Przybylinska, H., W. Jantsch, Yu. Suprun-Belevitch, M. Stepikhova, L. Palmetshofer, G. Hendorfer, A. Kozanecki, R. J. Wilson, and B. J. Sealy (July 15, 1996). “Optically Active Erbium Centers in Silicon”. In: *Physical Review B* 54.4, pp. 2532–2547. DOI: 10.1103/PhysRevB.54.2532.

Quan, Qimin, Parag B. Deotare, and Marko Loncar (May 17, 2010). “Photonic Crystal Nanobeam Cavity Strongly Coupled to the Feeding Waveguide”. In: *Applied Physics Letters* 96.20, p. 203102. DOI: 10.1063/1.3429125.

Quan, Qimin and Marko Loncar (Sept. 12, 2011). “Deterministic Design of Wavelength Scale, Ultra-High Q Photonic Crystal Nanobeam Cavities”. In: *Optics Express* 19.19, pp. 18529–18542. DOI: 10.1364/OE.19.018529.

Raha, Mouktik, Songtao Chen, Christopher M. Phenicie, Salim Ourari, Alan M. Dibos, and Jeff D. Thompson (Mar. 30, 2020). “Optical Quantum Nondemolition Measurement of a Single Rare Earth Ion Qubit”. In: *Nature Communications* 11.1 (1), p. 1605. DOI: 10.1038/s41467-020-15138-7.

Rahm, Martin, Roald Hoffmann, and N. W. Ashcroft (2016). “Atomic and Ionic Radii of Elements 1–96”. In: *Chemistry – A European Journal* 22.41, pp. 14625–14632. DOI: 10.1002/chem.201602949.

Rančić, Miloš, Morgan P. Hedges, Rose L. Ahlefeldt, and Matthew J. Sellars (Jan. 2018). “Coherence Time of over a Second in a Telecom-Compatible Quantum Memory Storage Material”. In: *Nature Physics* 14.1 (1), pp. 50–54. DOI: 10.1038/nphys4254.

Redjem, W., A. Durand, T. Herzig, A. Benali, S. Pezzagna, J. Meijer, A. Yu Kuznetsov, H. S. Nguyen, S. Cueff, J.-M. Gérard, I. Robert-Philip, B. Gil, D. Caliste, P. Pochet, M. Abbarchi, V. Jacques, A. Dréau, and G. Cassabois (Dec. 2020). “Single Artificial

Atoms in Silicon Emitting at Telecom Wavelengths". In: *Nature Electronics* 3.12 (12), pp. 738–743. DOI: 10.1038/s41928-020-00499-0.

Reiserer, Andreas (Dec. 16, 2022). "Colloquium: Cavity-enhanced Quantum Network Nodes". In: *Reviews of Modern Physics* 94.4, p. 041003. DOI: 10.1103/RevModPhys.94.041003.

Reiserer, Andreas, Norbert Kalb, Machiel S. Blok, Koen J. M. van Bemmelen, Tim H. Taminiau, Ronald Hanson, Daniel J. Twitchen, and Matthew Markham (June 22, 2016). "Robust Quantum-Network Memory Using Decoherence-Protected Subspaces of Nuclear Spins". In: *Physical Review X* 6.2, p. 021040. DOI: 10.1103/PhysRevX.6.021040.

Reiserer, Andreas, Norbert Kalb, Gerhard Rempe, and Stephan Ritter (Apr. 2014). "A Quantum Gate between a Flying Optical Photon and a Single Trapped Atom". In: *Nature* 508.7495 (7495), pp. 237–240. DOI: 10.1038/nature13177.

Reiserer, Andreas and Gerhard Rempe (Dec. 1, 2015). "Cavity-Based Quantum Networks with Single Atoms and Optical Photons". In: *Reviews of Modern Physics* 87.4, pp. 1379–1418. DOI: 10.1103/RevModPhys.87.1379.

Rinner, Stephan, Florian Burger, Andreas Gritsch, Jonas Schmitt, and Andreas Reiserer (July 27, 2023). "Erbium Emitters in Commercially Fabricated Nanophotonic Silicon Waveguides". In: *Nanophotonics*. DOI: 10.1515/nanoph-2023-0287.

Ruf, M., M.J. Weaver, S.B. van Dam, and R. Hanson (Feb. 19, 2021). "Resonant Excitation and Purcell Enhancement of Coherent Nitrogen-Vacancy Centers Coupled to a Fabry-Perot Microcavity". In: *Physical Review Applied* 15.2, p. 024049. DOI: 10.1103/PhysRevApplied.15.024049.

Ruskuc, Andrei, Chun-Ju Wu, Joonhee Choi, Sophie L. N. Hermans, and Andrei Faraon (Mar. 7, 2023). "APS -APS March Meeting 2023 - Event - Heralded Entanglement of Single Rare-Earth Ion Qubits". In: *Bulletin of the American Physical Society*. APS March Meeting 2023. Vol. Volume 68, Number 3. American Physical Society.

Ruskuc, Andrei, Chun-Ju Wu, Jake Rochman, Joonhee Choi, and Andrei Faraon (Feb. 2022). "Nuclear Spin-Wave Quantum Register for a Solid-State Qubit". In: *Nature* 602.7897 (7897), pp. 408–413. DOI: 10.1038/s41586-021-04293-6.

Saeedi, Kamyar, Stephanie Simmons, Jeff Z. Salvail, Phillip Dluhy, Helge Riemann, Nikolai V. Abrosimov, Peter Becker, Hans-Joachim Pohl, John J. L. Morton, and Mike L. W. Thewalt (Nov. 15, 2013). "Room-Temperature Quantum Bit Storage Exceeding 39 Minutes Using Ionized Donors in Silicon-28". In: *Science* 342.6160, pp. 830–833. DOI: 10.1126/science.1239584.

Saggio, Valeria, Carlos Errando-Herranz, Samuel Gyger, Christopher Panuski, Mihika Prabhu, Lorenzo De Santis, Ian Christen, Dalia Ornelas-Huerta, Hamza Raniwala, Connor Gerlach, Marco Colangelo, and Dirk Englund (Feb. 20, 2023). *Cavity-Enhanced Single Artificial Atoms in Silicon*. DOI: 10.48550/arXiv.2302.10230. arXiv: 2302.10230 [physics, physics:quant-ph]. preprint.

Simmons, Stephanie (Nov. 8, 2023). *Scalable Fault-Tolerant Quantum Technologies with Silicon Colour Centres*. DOI: 10.48550/arXiv.2311.04858. arXiv: 2311.04858 [quant-ph]. preprint.

Sinclair, Gary F., Nicola A. Tyler, Döndü Sahin, Jorge Barreto, and Mark G. Thompson (Apr. 25, 2019). "Temperature Dependence of the Kerr Nonlinearity and Two-Photon Absorption in a Silicon Waveguide at 1.55 $\ensuremath{\mu}\mathrm{m}$". In: *Physical Review Applied* 11.4, p. 044084. DOI: 10.1103/PhysRevApplied.11.044084.

Srinivasan, Kartik and Oskar Painter (Mar. 24, 2003). "Fourier Space Design of High-Q Cavities in Standard and Compressed Hexagonal Lattice Photonic Crystals". In: *Optics Express* 11.6, pp. 579–593. DOI: 10.1364/OE.11.000579.

Stas, P.-J., Y. Q. Huan, B. Machielse, E. N. Knall, A. Suleymanzade, B. Pingault, M. Sutula, S. W. Ding, C. M. Knaut, D. R. Assumpcao, Y.-C. Wei, M. K. Bhaskar, R. Riedinger, D. D. Sukachev, H. Park, M. Lončar, D. S. Levonian, and M. D. Lukin (Nov. 4, 2022). "Robust Multi-Qubit Quantum Network Node with Integrated Error Detection". In: *Science* 378.6619, pp. 557–560. DOI: 10.1126/science.add9771.

Stevenson, Paul, Christopher M. Phenicie, Isaiah Gray, Sebastian P. Horvath, Sacha Welinski, Austin M. Ferrenti, Alban Ferrier, Philippe Goldner, Sujit Das, Ramamoorthy Ramesh, Robert J. Cava, Nathalie P. de Leon, and Jeff D. Thompson (June 10, 2022). "Erbium-Implanted Materials for Quantum Communication Applications". In: *Physical Review B* 105.22, p. 224106. DOI: 10.1103/PhysRevB.105.224106.

Suter, Dieter and Gonzalo A. Álvarez (Oct. 10, 2016). "Colloquium: Protecting Quantum Information against Environmental Noise". In: *Reviews of Modern Physics* 88.4, p. 041001. DOI: 10.1103/RevModPhys.88.041001.

Szabo, A. (June 1, 1975). "Observation of Hole Burning and Cross Relaxation Effects in Ruby". In: *Physical Review B* 11.11, pp. 4512–4517. DOI: 10.1103/PhysRevB.11.4512.

Thiel, C. W., Thomas Böttger, and R. L. Cone (Mar. 1, 2011). "Rare-Earth-Doped Materials for Applications in Quantum Information Storage and Signal Processing". In: *Journal of Luminescence*. Selected Papers from DPC'10 131.3, pp. 353–361. DOI: 10.1016/j.jlumin.2010.12.015.

Thomas, Gordon A., Boris I. Shraiman, Paul F. Glodis, and Michael J. Stephen (Mar. 2000). "Towards the Clarity Limit in Optical Fibre". In: *Nature* 404.6775 (6775), pp. 262–264. DOI: 10.1038/35005034.

Tiecke, T. G., J. D. Thompson, N. P. de Leon, L. R. Liu, V. Vuletić, and M. D. Lukin (Apr. 2014). "Nanophotonic Quantum Phase Switch with a Single Atom". In: *Nature* 508.7495 (7495), pp. 241–244. DOI: 10.1038/nature13188.

Ulanowski, Alexander, Johannes Früh, Fabian Salamon, Adrian Holzäpfel, and Andreas Reiserer (Nov. 28, 2023). *Spectral Multiplexing of Rare-earth Emitters in a Co-doped Crystalline Membrane*. DOI: 10.48550/arXiv.2311.16875. arXiv: 2311.16875 [quant-ph]. preprint.

Ulanowski, Alexander, Benjamin Merkel, and Andreas Reiserer (Oct. 26, 2022). "Spectral Multiplexing of Telecom Emitters with Stable Transition Frequency". In: *Science Advances* 8.43, eabo4538. DOI: 10.1126/sciadv.abo4538.

Uphoff, Manuel, Manuel Brekenfeld, Gerhard Rempe, and Stephan Ritter (Jan. 2015). "Frequency Splitting of Polarization Eigenmodes in Microscopic Fabry–Perot Cavities". In: *New Journal of Physics* 17.1, p. 013053. DOI: 10.1088/1367-2630/17/1/013053.

Van Leent, Tim, Matthias Bock, Florian Fertig, Robert Garthoff, Sebastian Eppelt, Yiru Zhou, Pooja Malik, Matthias Seubert, Tobias Bauer, Wenjamin Rosenfeld, Wei Zhang, Christoph Becher, and Harald Weinfurter (July 2022). "Entangling Single Atoms over 33 Km Telecom Fibre". In: *Nature* 607.7917 (7917), pp. 69–73. DOI: 10.1038/s41586-022-04764-4.

Vinh, N. Q., N. N. Ha, and T. Gregorkiewicz (July 2009). "Photonic Properties of Er-Doped Crystalline Silicon". In: *Proceedings of the IEEE* 97.7, pp. 1269–1283. DOI: 10.1109/JPROC.2009.2018220.

Watkins, George D. (Aug. 1, 2000). "Intrinsic Defects in Silicon". In: *Materials Science in Semiconductor Processing* 3.4, pp. 227–235. DOI: 10.1016/S1369-8001(00)00037-8.

Wehner, Stephanie, David Elkouss, and Ronald Hanson (Oct. 19, 2018). "Quantum Internet: A Vision for the Road Ahead". In: *Science* 362.6412, eaam9288. DOI: 10.1126/science.aam9288.

Weiß, Lorenz Karl Wilhelm (2022). "Erbium Dopants in Silicon Nanophotonic Waveguides". Technische Universität München.

Weiss, Lorenz, Andreas Gritsch, Benjamin Merkel, and Andreas Reiserer (Jan. 20, 2021). "Erbium Dopants in Nanophotonic Silicon Waveguides". In: *Optica* 8.1 (1), pp. 40–41. DOI: 10.1364/OPTICA.413330.

Wolfowicz, Gary, F. Joseph Heremans, Christopher P. Anderson, Shun Kanai, Hosung Seo, Adam Gali, Giulia Galli, and David D. Awschalom (Oct. 2021). "Quantum Guidelines for Solid-State Spin Defects". In: *Nature Reviews Materials* 6.10 (10), pp. 906–925. DOI: 10.1038/s41578-021-00306-y.

Wu, Yulin et al. (Oct. 25, 2021). "Strong Quantum Computational Advantage Using a Superconducting Quantum Processor". In: *Physical Review Letters* 127.18, p. 180501. DOI: 10.1103/PhysRevLett.127.180501.

Xie, Tian, Jake Rochman, John G. Bartholomew, Andrei Ruskuc, Jonathan M. Kindem, Ioana Craiciu, Charles W. Thiel, Rufus L. Cone, and Andrei Faraon (Aug. 16, 2021). "Characterization of $Er^{3+} : YVO_4$ for Microwave to Optical Transduction". In: *Physical Review B* 104.5, p. 054111. DOI: 10.1103/PhysRevB.104.054111.

Xue, Xiao, Maximilian Russ, Nodar Samkharadze, Brennan Undseth, Amir Sammak, Giordano Scappucci, and Lieven M. K. Vandersypen (Jan. 2022). "Quantum Logic with Spin Qubits Crossing the Surface Code Threshold". In: *Nature* 601.7893 (7893), pp. 343–347. DOI: 10.1038/s41586-021-04273-w.

Yamada, Koji (2011). "Silicon Photonic Wire Waveguides: Fundamentals and Applications". In: *Silicon Photonics II: Components and Integration*. Ed. by David J. Lockwood and Lorenzo Pavesi. Topics in Applied Physics. Berlin, Heidelberg: Springer Berlin Heidelberg, pp. 1–29. DOI: 10.1007/978-3-642-10506-7_1.

Yang, Dongxun, Jiashuai Wang, Rui Li, Yanqing Ma, and Lei Ma (Nov. 2019). "Extremely Vertical Sidewall Trench Etching on Silicon Substrate and Modelling Etching Using Artificial Neural Network". In: *Materials Research Express* 6.12, p. 125902. DOI: 10.1088/2053-1591/ab55b4.

Yin, Chunming, Milos Rancic, Gabriele G. de Boo, Nikolas Stavrias, Jeffrey C. McCallum, Matthew J. Sellars, and Sven Rogge (May 1, 2013). "Optical Addressing of an Individual Erbium Ion in Silicon". In: *Nature* 497, p. 91.

Zeng, Beibei, Chawina De-Eknamkul, Daniel Assumpcao, Dylan Renaud, Zhuoxian Wang, Daniel Riedel, Jeonghoon Ha, Carsten Robens, David Levonian, Mikhail Lukin, Mihir Bhaskar, Denis Sukachev, Marko Loncar, and Bart Machielse (June 16, 2023). *Cryogenic Optical Packaging of Nanophotonic Devices with Coupling Loss < 1 dB*. DOI: 10.48550/arXiv.2306.09894. arXiv: 2306.09894 [physics, physics:quant-ph]. preprint.

Zhong, Han-Sen, Hui Wang, Yu-Hao Deng, Ming-Cheng Chen, Li-Chao Peng, Yi-Han Luo, Jian Qin, Dian Wu, Xing Ding, Yi Hu, Peng Hu, Xiao-Yan Yang, Wei-Jun Zhang, Hao Li, Yuxuan Li, Xiao Jiang, Lin Gan, Guangwen Yang, Lixing You, Zhen Wang, Li Li, Nai-Le Liu, Chao-Yang Lu, and Jian-Wei Pan (Dec. 18, 2020). "Quantum Computational Advantage Using Photons". In: *Science* 370.6523, pp. 1460–1463. DOI: 10.1126/science.abe8770. pmid: 33273064.

Zhong, Manjin, Morgan P. Hedges, Rose L. Ahlefeldt, John G. Bartholomew, Sarah E. Beavan, Sven M. Wittig, Jevon J. Longdell, and Matthew J. Sellars (Jan. 2015). "Optically Addressable Nuclear Spins in a Solid with a Six-Hour Coherence Time". In: *Nature* 517.7533, pp. 177–180. DOI: 10.1038/nature14025.

Zhong, Tian and Philippe Goldner (Nov. 1, 2019). "Emerging Rare-Earth Doped Material Platforms for Quantum Nanophotonics". In: *Nanophotonics* 8.11, pp. 2003–2015. DOI: 10.1515/nanoph-2019-0185.

Zhou, Yiru, Pooja Malik, Florian Fertig, Matthias Bock, Tobias Bauer, Tim van Leent, Wei Zhang, Christoph Becher, and Harald Weinfurter (Aug. 17, 2023). *Long-Lived Quantum Memory Enabling Atom-Photon Entanglement over 101 Km Telecom Fiber*. DOI: 10.48550/arXiv.2308.08892. arXiv: 2308.08892 [quant-ph]. preprint.

Ziegler, James (2023). *SRIM & TRIM*. URL: http://www.srim.org/ (visited on 08/25/2023).

List of Figures

List of Tables